Regulation of Hysteretic Systems with Preisach Representation

by

Li Wang

A thesis
presented to the University of Waterloo
in fulfillment of the
thesis requirement for the degree of
Master of Applied Science
in
Electrical and Computer Engineering

Waterloo, Ontario, Canada, 2009

I hereby declare that I am the sole author of this thesis. This is a true copy of the thesis, including any required final revisions, as accepted by my examiners.

I understand that my thesis may be made electronically available to the public.

Abstract

Piezoelectric actuators are well suited for high precision mechanical and electrical engineering applications. However, its performance in regulator configurations has been limited due to hysteresis. The hysteresis in these actuators means that multiple input states can result in the same output, which introduces a further design variable (initial state) in the regulation problem. It is proposed that certain initial states result in better regulation performance based on the structure of the Preisach model. These initial states are called "neutral states".

In this thesis, hysteresis and piezoelectric actuators are introduced as background information. The Preisach model is used in this work to describe the hysteresis behaviour of a customized shape control unit SS15 due to its convenient general structure and ability to model hysteresis. The representation tests are performed and a Preisach model is subsequently constructed and verified by comparing simulation and experimental results to ensure that the hysteresis inherent in the piezoceramic actuators of the SS15 is suitably described by this model. In order to evaluate the regulation performance for a given desired output, uniformly-distributed noise is injected at the input side of the SS15 in open- and closed-loop tests. It is demonstrated, by both simulation and experimental results, that the system output drifts less when it starts from the neutral state in open-loop tests. A PI regulator is implemented in the closed-loop tests. When the system is driven from the neutral state, both simulation and experimental results demonstrate that the system requires less control effort for closed-loop regulation.

Acknowledgments

I would like to express my deepest and sincerest gratitude to my supervisor Professor Robert B. Gorbet for his patient support and guidance during my study at the University of Waterloo.

My extreme appreciation goes to the research associate Eric Kubica for his great help in my thesis. I would like to thank my readers Professor Paul Calamai and Professor Dave Wang for providing valuable feedback on this work. I would also like to thank Professor Kirsten Morris for her comments on my research.

I'm deeply grateful to Kevin Krauel for his generous help in the experimental setup. My special thanks are to Shailaja Sajja, Mohamed El Deeb, Hao Luan and Ming Gong for their friendly help in my research and life.

Last but not least, I appreciate my family's encouragement, kindest help, constructive advice and support.

Dedication

This is dedicated to my mom, dad and love.

Contents

List of Figures

List of Tables

Chapter 1

Introduction

Nowadays piezoelectric actuators are drawing significant attention in the field of precision engineering. For example, shape control can be achieved by spatially distributed piezoelectric actuators, which exert forces to modify and maintain the shape of the material bonded or incorporated with piezoelectric ceramics. In this chapter, the motivation behind the use of piezoelectric actuators to perform shape control is discussed from various aspects. In particular, discussion is provided as to the advantages of utilizing actuators made of so-called smart material, the main goals of shape control and the inherent hysteretic nonlinearity observed in these smart materials. Furthermore the goals of the thesis are specified based on previous research efforts in the area of influence of initial state on regulation of actuators with hysteresis. Finally the outline of the thesis is listed.

1.1 Motivation

Over the past few decades, there has been a significantly increasing interest in the realm of smart materials, such as piezoelectric ceramics and shape memory alloys, especially focused towards their applications as actuators in high performance control design. In comparison to the numerous research efforts on the use of smart structures[1] in active vibration suppression, much less attention has been focused on the use of smart structures in shape control because the displacement of the piezoceramics used is very small and the precise positioning control is seriously affected by hysteresis.

Shape control is highly related to control engineering since the main goal of shape control is to apply appropriate actuation in order to minimize the influence of specific external disturbances. For example, Haftka and Adelman introduce the notion of shape control in a contribution [2]. In this work, the temperatures in control elements are computed in order to minimize the overall distortion of a space structure from its original shape. Much research has been focussed on solving the problems of drive signal determination and optimal actuator placement in order to achieve a certain shape. A considerable amount of literature can be found on piezoceramic actuators bonded

[1] A smart structure is one that monitors itself and/or its environment in order to respond to changes in its condition [1].

to or embedded into beams, shells and plates. Piezoelectric actuators offer high resolution down to the subnanometer range, high stiffness, low wear and tear, and fast response times [3]. Therefore these actuators are well suited for high precision electromechanical engineering applications.

For instance, Koconis et. al [4] investigate the changes in the shapes of fiber-reinforced composite beams, plates and shells due to embedded piezoelectric actuators. In that work, the actuation voltages are determined in order to achieve a specific shape by following an established analytical method, which successfully converts the shape control problem into a series of distributed regulation control problems. Agrawal and Treanor [5] have analytically solved the problem of optimal placement of piezoceramic actuators for shape control of beam structures and optimum piezoceramic actuator voltages, such that the error between the desired shape and the achieved shape is minimized, as has been demonstrated experimentally. Also the significant effects of hysteresis were observed and considered since the practical shape control application demands feedback of the beam's shape in order to ensure the desired deformation is obtained.

For a linear system, the setpoint regulation problem has been fully investigated and well understood, e.g., [6]. Unfortunately the regulation task is considerably more complicated when the actuator includes smart materials due to their inherent hysteresis nonlinearity. Hysteretic behaviour means that for a given output, there exists a range of inputs [7], which act like multiple states because of memory. Hysteresis also limits the performance of systems since it can give rise to undesirable loss of accuracy or oscillations, and even lead to instability [8].

This thesis investigates if there is a specific state holding attractive properties among those multiple states, such as high noise or disturbance rejection, for a given setpoint. An important measure of regulating performance is the maximum output transient caused by disturbances, since this determines the deviation from the desired shape. As shown in [7], the existence of a state with the above stated advantages has been demonstrated for hysteretic systems, specifically in shape memory alloy and piezoceramic actuator. This "neutral state" has better rejection of uniformly-distributed noise at its input in open-loop tests and requires the least control effort in a closed-loop regulation control systems. The reachability of this so-called "neutral state" is investigated together with the input required to drive the system to the appropriate neutral state. As noted in [7], the neutral state locus appears to pass through points inside the major hysteresis loop on the input and output plane where the internal ascending and descending branches have similar slopes. In [7], neutral state existence has been intuitively explained based on the Preisach model. The better regulating performance of the neutral state in terms of superior input noise rejection has been demonstrated during open-loop tests in both simulations and experiments. However, its superior regulating performance in terms of the least control effort required in closed-loop regulation tests is only demonstrated by the simulation results in [7]. This thesis extends the work of Gorbet by validating his results experimentally on a new system driven by piezoceramic actuators but with a different configuration. Moreover, this thesis provides the first experimental closed-loop results in this area.

1.2 Thesis Goals

There are several goals of this research which are listed below.

- Preisach model representation test: According to [9], in order to use the classical Preisach model to describe a hysteretic behaviour, certain necessary and sufficient conditions have to

be satisfied such as wiping-out property and congruent minor loop property. Experimental tests are implemented on the shape control system in order to verify that the hysteresis behaviour inherent in piezoceramic actuator can be represented by the Preisach model under certain conditions such as a low frequency input signal.

- Preisach model construction: Following the procedure introduced by Mayergoyz in [9], the data required for parameter identification (first order descending curves) are collected from experiments in order to build the Preisach model. Curve fitting and surface fitting are applied to obtain the weighting functions of the Preisach model.

- Input noise rejection open-loop test: Following the procedure in [7], noise rejection tests are performed on the shape control system in order to demonstrate the existence and the better open-loop set-point control performance of a neutral state initial condition with hysteresis. Both simulation and experimental results are obtained which demonstrate improved noise rejection when starting from the neutral state.

- Closed-loop regulation tests with the injection of input noise: A PI controller is designed and implemented in order to accomplish fast, accurate and robust regulation tasks. The control effort is calculated and compared quantitatively when various initial states and different noise gains are applied. Both simulation and experimental results are obtained.

1.3 Thesis Outline

The thesis is organized as follows:

- Chapter 2 introduces the background information regarding hysteresis and piezoceramic actuators. The hysteresis modelling is also investigated and the Preisach model is explained in detail since it has been chosen to describe the shape control unit with hysteresis. Based on the state-space representation of the Preisach model, the definition of a neutral state is provided graphically and discussed.

- Chapter 3 shows the experimental setup and the Preisach model representation test and the Preisach model identification.

- Chapter 4 provides both simulation and experimental results in open-loop drift tests when there is input noise. The differential output is applied as the metric to measure the output drift quantitatively. The explanation of the better regulating performance of the neutral state is also provided.

- Chapter 5 presents both simulation and experimental results in closed-loop regulation tests using a PI controller. The 2-norm of the control effort is applied to compare the control effort quantitatively when different initial states and noise amplitudes are applied.

- Chapter 6 provides conclusions on the employment of the neutral state based on the simulation and experimental results collected in open-loop and closed-loop tests when input noise is present. Future work is also discussed as extensions of the work in the thesis.

- Appendix A introduces the definition of a reduced memory sequence and presents the derivative of the Preisach model. The author believes that this is the first attempt to provide a formal input-output derivative of Preisach model behaviour, and that the derivative may be useful in proving optimality of the neutral state in future work.

Chapter 2

Background

In this chapter, the background information regarding hysteresis and piezoelectric actuators is introduced. Hysteresis modelling techniques are divided into three categories. Among these modelling techniques, the Preisach model, its representation property, and its identification procedure are presented in detail since it is adopted to model the hysteresis of a piezoceramic actuator in Chapter 3. The state space representation of Preisach model is also reviewed as it would be necessary tool for discussing the influence of initial states in a hysteretic system.

2.1 Hysteresis Definition

Hysteresis is a property of system where the output is not only a strict function of the input, but also incorporates a lag or memory of the input history. The term hysteresis originates from ancient Greek and is first used to describe ferromagnetism [10] and many useful models have developed in this domain [11], [12]. Another area where early hysteresis models are used is plasticity. After the maximum shear stress yield criterion is introduced by Tresca in 1864, numerous investigations emphasize this criterion increasingly [10]. Moreover, hysteresis can also be found in various fields, such as ferroelectricity [13], [14], thermostatics [15], [16], shape memory effects [17], [18], and mechanics [19], [20].

In [9], the terminology from control theory is adapted in the definition of hysteresis. First consider a transducer with $u(t)$ and $y(t)$ as its time dependant input and output respectively, as shown in Figure 2.1 (a). If the relationship between $u(t)$ and $y(t)$ consists of a multi-branch nonlinearity and the transitions from branch to branch occur after input extrema, then such a transducer is named as "hysteresis transducer" [9]. Such a relationship is illustrated in Figure 2.1 (b).

Hysteresis can be divided into two categories, namely: static hysteresis and dynamic hysteresis corresponding to the terminology of rate-independent and rate-dependent hysteresis respectively. For a static or rate-independent hysteresis, only the past extrema values of the inputs determine the branches while the rate of input variations between extrema do not affect the branches. On the other hand, the branches of a dynamic or rate-dependent hysteresis are determined by both the past extrema values of the inputs and the rate of input variations between extrema.

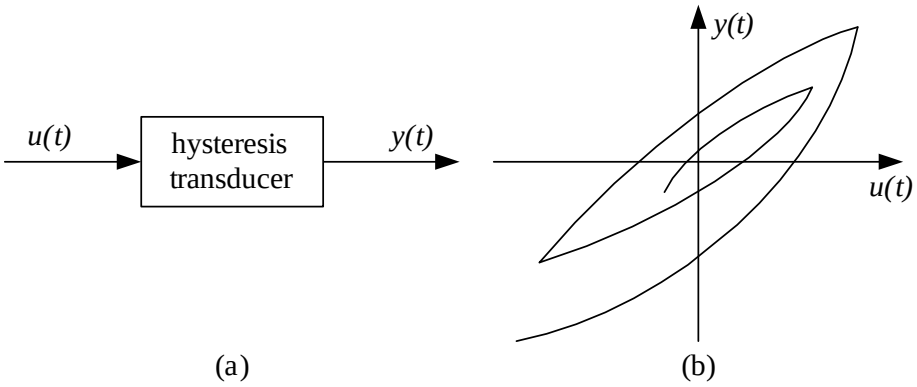

Figure 2.1: (a) Hysteresis transducer (b) Multi-branch nonlinearity [9].

As illustrated in Figure 2.2, the major hysteresis loop is *the limiting loop* enclosing all other hysteresis loops, typically referred to as minor loops within the major hysteresis loop.

2.2 Piezoelectric Actuator

There are currently two main types of piezoelectric materials: ceramics and polymers. Piezoelectric ceramics are probably the most important piezoelectric materials and the vast majority of piezoceramics belong to the lead-zirconate-titanate (PZT) family, which are extensively used as strain sensors and as mechanical sources of displacement [21].

Piezoelectric ceramics transduce energy between the electrical and mechanical domains. Application of an electric field across the ceramic produces a mechanical strain, and application of a mechanical stress on the ceramic induces an electrical charge in a similar manner. The use of the piezoelectric effect in actuators relies on the first property.

Piezoelectric materials change shape when their electrical dipoles spontaneously align in electric fields, causing deformation of the crystal structure. Piezoceramic actuators can be constructed in a number of different configurations such as stack, bender, and building-block types [22]. Fundamentally, a bimorph piezoelectric actuator is two piezoceramic strips glued to a passive metal substrate. Bimorph bender actuators are used in the shape control unit (SS15) [23] studied in this research, and thus, it will be discussed in detail.

Bender actuators use the internal piezoelectric strain to indirectly generate actuator motion. The bimorph bender actuator consists of two layers of piezoelectric material, which are poled and activated such that layers on opposite sides of the neutral axis have opposing strain as shown in Figure 2.3. An internal bending moment is generated by the opposing strain from the piezoelectric layers and results in the motion of the bender, which causes a quadratic amplification of actuator stroke as a function of length [22]. Additionally, inactive substrates may be included to achieve higher structural strength.

The biomorph bender actuator was first developed in the 1930s by Sawyer [24]. However the performance of these actuators has not been examined in depth until research into smart

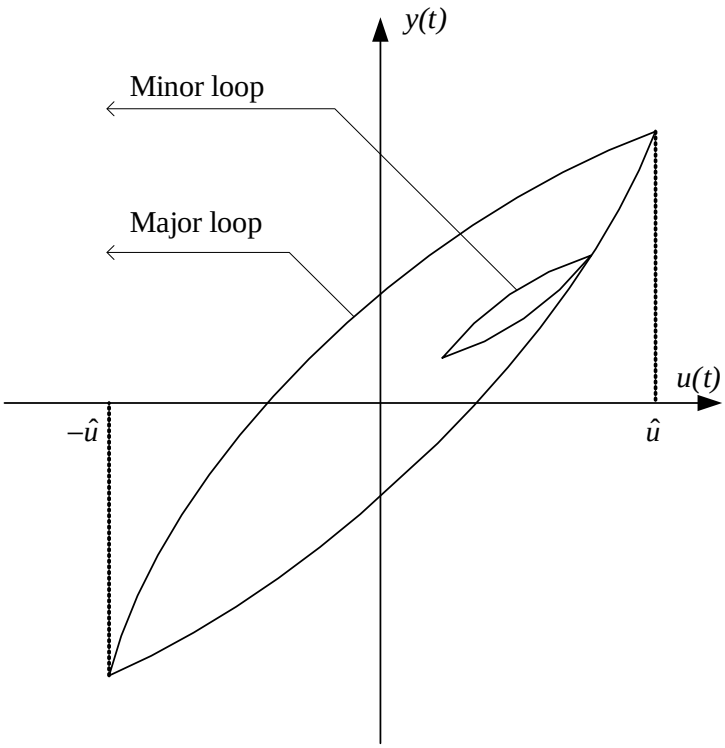

Figure 2.2: A major loop and minor loop of hysteresis.

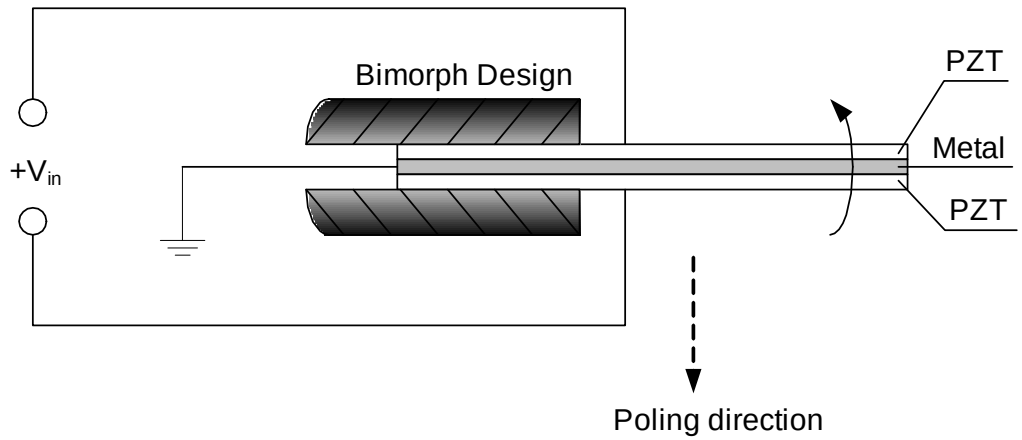

Figure 2.3: Illustration of bimorph bender actuator [3].

structures became popular in the past three decades [25], [26]. Subsequently, biomorph bender actuators have been utilized in various fields, such as robotic applications requiring relatively large displacements [27], spoilers on missile fins [28] and to actuate a quick-focusing lens [29].

A standards committee of the IEEE Ultrasonics, Ferroelectrics, and Frequency Control Society originally published a description of piezoelectric ceramic behaviour in 1966 and revised it in 1987 [30]: linearized constitutive relations are formulated to describe piezoelectric continua which form the basis for the model of piezoelectric behaviour that is in general use now. Typically the linearized constitutive relations are represented in a compressed matrix notation as follow:

$$S_p = s^E_{pq} T_q + d_{pk} E_k \tag{2.1}$$

$$D_i = d_{iq} T_q + \varepsilon^T_{ik} E_k \tag{2.2}$$

where S is the strain tensor, s^E represents the elastic compliance matrix when subjected to a constant electrical field, T represents the stress tensor, d is a matrix of piezoelectric material constants, E is the electric field vector, D is the electric displacement vector and ε^T is the permittivity measured at a constant stress. The subscripts indicate the dimensions of the matrices. Eq. (2.1) and (2.2) state that the material strain and electrical displacement exhibited by a piezoelectric ceramic are both linearly affected by the mechanical stress and electrical field to which the ceramic is subjected. However, these linearized constitutive relations are not able to explicitly describe the nonlinearities that are present in all piezoelectric ceramics. Moreover, these equations are derived by assuming a purely conservative energy field. As a result, it is impossible for them to describe the dissipative behavioural aspects of the ceramic as pointed out in [31]. In fact, all currently employed smart materials, including piezoelectric materials, exhibit some degree of hysteresis in the relation between input fields, temperatures, or stresses and output displacements [32]. Piezoceramics become useful as actuators after the poling process. A residual electric field still remains within the material and generates a "pre-strain" after the poling field is removed. Consequently, strain will increase if fields of the same polarity as the poling field are applied, while strain will decrease if fields of the opposite polarity are applied. When the applied

field is removed, the dipoles will tend to realign themselves along the residual field remaining within the material from the poling process. However, the dipoles cannot realign totally due to the material defects. Therefore, the hysteresis phenomena occurs [33].

2.3 Hysteresis Modelling History

Roughly speaking, hysteresis models for piezoelectric materials can be separated into three categories: "microscopic, macroscopic or semi-macroscopic" as pointed out by Smith [34]. In general, the models tend to employ energy principles, phenomenological principles, or a combination of the two.

2.3.1 Microscopic Models

In microscopic models of hysteresis [35], quantum principles, typical elasticity or electromagnetic relations, or thermodynamic laws are employed at a lattice or grain level. Viscosity coefficients are taken into account when the free energy of a one-dimensional lattice system is calculated for a ferroelectric material, such that the hysteresis behaviour between the applied electric field and polarization is built in [35]. Their simulation results show that the hysteresis curves generated based on such a model are acceptable. However, numerous states and parameters are required in the model even for the one-dimensional lattice, which makes the microscopic models not very suitable in control applications.

2.3.2 Semi-macroscopic Models

Semi-macroscopic models employ a combination of physical and phenomenological principles. Attributions from the polarization switching mechanism are characterized based on energy relations. The parameters of the resulting models are obtained through macroscopic averages for describing the hysteresis.

For instance, the homogenized energy model generated by Smith [32] is a combination of "aspects of the homogenized free energy theory of [36] and Preisach models posed in terms of general densities or measure". As a result, the model is linearly dependent on the parameters and can be considered for various areas of controller design [8]. Generally speaking, the main goal of semi-macroscopic models is to utilize known physics to promote model construction and real-time updating by employing energy-based relations.

2.3.3 Macroscopic Models

Macroscopic models are built for the inherent hysteresis of ferroelectric materials by employing phenomenological principles. The purely phenomenological models include the Preisach and generalized Preisach models, which were originally constructed to describe magnetic hysteresis [37], and have subsequently been extended to piezoceramic materials in various formats [10], [38], [39], [40], and [41].

In the classical form, Preisach operators are constructed from a linear combination of multi-valued kernels [42]. Each kernel is characterized by two saturation states and the coefficients of each kernel represent the input magnitude when switching occurs between those two saturation states. As introduced in detail in Section 2.4, Preisach models are purely mathematical models to describe hysteretic behavior because only phenomenological principles are employed. As noted in [9], hysteretic nonlinearities can be exactly represented by the classical Preisach model as long as the hysteresis holds the wiping-out and congruency properties. Consequently the Preisach model of hysteresis is identified simply by determining the weighting function of the elementary hysteresis operators.

However, some hysteresis cannot satisfy both the wiping-out and congruency properties. Hence, a generalized Preisach model was developed to describe hysteresis in such cases [43]. The generalized Preisach model loosens the congruency property of the classical model and fits both first and second order transition curves.

Moreover, a Preisach-based dynamic hysteresis model is presented as another extension of the classical Preisach model in [44]. The dynamic Preisach model can describe the rate dependent nature of the voltage to displacement dynamics in a piezoceramic actuator and a recursive form of the model was developed for real-time implementation. Details of Preisach modelling are provided in the following section.

2.4 The Preisach Model

The Preisach model is used in this thesis due to its convenient general structure and ability to model hysteresis. It was originally developed to describe the hysteresis in magnetic material. However, in accordance with experimental work in recent decades, it can also be used to describe the behaviour in many other hysteretic materials, such as SMAs [45], [46]. For the classical Preisach model, it is assumed that the hysteresis is rate-independent, which means that the relationship between input $u(t)$ and output $y(t)$ are invariant under changes in the input rate. However, such an assumption is not satisfied in the hysteresis behaviour of piezoceramics at high frequency inputs. An extended Preisach model, which is the Preisach based dynamic hysteresis model, is introduced by Hu and Ben Mrad [44] in order to describe the hysteresis of piezoceramic actuators for high frequency input signals.

The elementary block of the Preisach model is the hysteresis relay operator $\gamma_{r,s}$.

$$\gamma_{r,s}[u(t)] = \begin{cases} +1, & u(t) \geq s + r \\ \gamma_0, & s - r \leq u(t) \leq s + r \\ -1, & u(t) \leq s - r \end{cases} \tag{2.3}$$

where $r > 0$ and s as its half-width and input offset respectively. $\gamma_{r,s} = \pm 1$ depending on the input $u(t)$ as shown in Figure 2.4 and is defined by Eq. (2.3), where γ_0 is the initial state. The model structure is illustrated in Figure 2.5. The weighted sum of each individual relay output equals the output $y(t)$, and $\mu(r, s)$ stands for the weight of the relay $\gamma_{r,s}$. The Preisach model output is defined for continuous inputs $u(t)$. Since the input $u(t)$ varies with time, the output of each elementary relay $\gamma_{r,s}[u(t)]$ is tuned according to the current input value, and the weighted

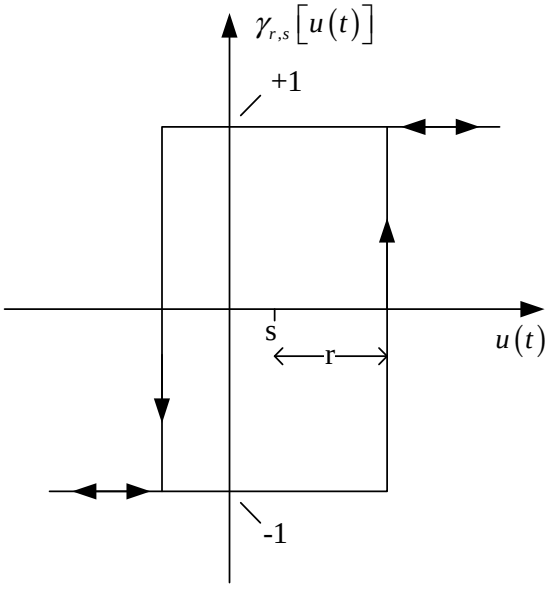

Figure 2.4: Hysteresis relay.

sum of all relay outputs is the overall system output $y(t)$ as shown in Eq. (2.4).

$$y(t) = \int_{0}^{\infty}\int_{-\infty}^{\infty} \mu(r,s)\gamma_{r,s}\left[u(t)\right] dsdr \tag{2.4}$$

The right half-plane $\Re_+ \times \Re$ is often referred to as the Preisach plane P, in which every point presents a unique relay. The collection of weights $\mu(r,s)$ forms the Preisach weighting function $\mu : P \rightarrow \Re$, which can be experimentally determined for a given system. The approach as defined in [9] is used to identify the Preisach model of the hysteresis behaviour in a piezoceramic bimorph bender actuator in this thesis. If there are physical limitations such as control input saturation $\hat{u}$, the domain of μ can be restricted to a triangle $P_r = \{(r,s) \in P : |s| \leq \hat{u} - r\}$, which is referred as the restricted Preisach plane.

The Preisach plane is important since it can be used to track individual relay states in the following way. First of all, the relays are divided into two time-varying sets $P_-(t)$ and $P_+(t)$ defined by Eq. (2.5) as:

$$P_\pm(t) = \left\{(r,s) \in P_r : \gamma_{r,s}\left[u(t)\right] = \pm 1\right\} \tag{2.5}$$

In the Preisach plane time dependence is often implicit, so P_- and P_+ are used instead of $P_-(t)$ and $P_+(t)$. Obviously $P_- \cup P_+ = P_r$ is satisfied, which means that P_- and P_+ are connected and separated by the line ψ known as the Preisach plane boundary, which can be considered as a map ψ: $R_+ \times R \rightarrow R$ defined by $s = \psi(t,r)$. The evolution of the Preisach plane boundary ψ is illustrated in Figure 2.6 corresponding to Case 1 (Figure 2.6 (a) and (b)): a monotonically increasing input $u(t)$ starting from negative saturation and Case 2 (Figure 2.6 (c) and (d)): a

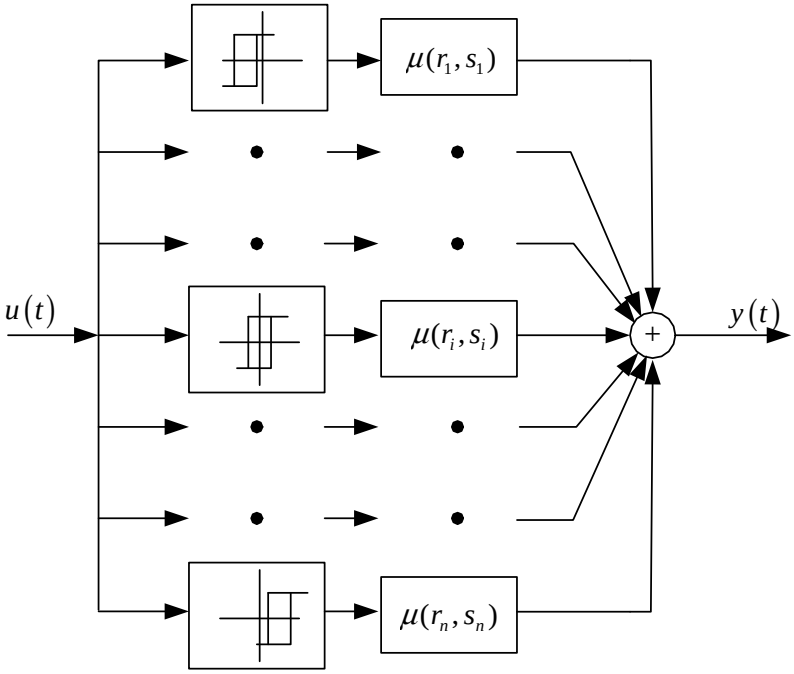

Figure 2.5: Preisach model structure.

monotonically decreasing input $u(t)$ starting from positive saturation separately. So at first in Case 1, all relays are turned off, i.e. all relays' output are -1 and $P_- = P_r$, $P_+ = 0$ (Figure 2.6 (a)). As the input increases, it switches on those relays $\gamma_{r,s} \in \{(r,s) \in P_+ : s \leq u(t) - r\}$ as it passes $u(t) = s + r$, and moves them from P_- to P_+. The boundary between P_- and P_+ can be represented as a segment of slope -1 in Figure 2.6(b). On the other hand for Case 2, all relays are turned on initially, i.e. all relays' output are +1 and $P_+ = P_r$, $P_- = 0$ (Figure 2.6(c)). As the input decreases, it switches off those relays $\gamma_{r,s} \in \{(r,s) \in P_- : s \geq u(t) + r\}$ as it passes $u(t) = s - r$, and moves them from P_+ to P_-. The Preisach plane boundary ψ is represented in Figure 2.6(d) as a segment of slope +1 for a monotonically decreasing input $u(t)$. P_+ is below P_- and the Preisach plane boundary ψ always intersects the axis $r = 0$ at the current input value $u(t)$.

The Preisach plane boundary also represents the memory of the Preisach model. When an arbitrary input is applied, input reversals cause corners in the boundary as shown in Figure 2.7. Moreover, the history of past input reversals and branching behaviour is stored via the corners of the boundary. However, some of the corners in the boundary may disappear when wiping-out happens, which is one of the two necessary and sufficient conditions for the existence of a Preisach representation of a hysteretic phenomenon [9]. These two conditions will be discussed in detail in the following section.

Now, according to [47], the output can be calculated based on the Preisach plane boundary $\psi(t,r)$ by separating the restricted Preisach plane P_r into $P_+(t)$ and $P_-(t)$:

$$y(t) = 2 \iint_{P_+(t)} \mu(r,s)\, dsdr - \iint_{P_r} \mu(r,s)\, dsdr \tag{2.6}$$

or

$$y(t) = -2 \iint_{P_-(t)} \mu(r,s)\, dsdr + \iint_{P_r} \mu(r,s)\, dsdr \tag{2.7}$$

The output variation generated by a monotonic change in input is stated in the following proposition [47].

Proposition 1 (Output Variation) *[47]*

A monotonic change in input which causes the boundary to sweep out an area Ω from time t_1 to t_2 leads to an output variation

$$y(t_2) - y(t_1) = 2sgn\left[u(t_2) - u(t_1)\right] \iint_{\Omega} \mu(r,s)\, dsdr \tag{2.8}$$

This relationship is needed subsequently to establish the connection between the output variation and the input disturbance.

2.5 Preisach Model Representation Property

In the previous section, the Preisach plane and Preisach boundary are introduced, which are two important concepts in the Preisach model. According to Mayergoyz, there are two necessary and

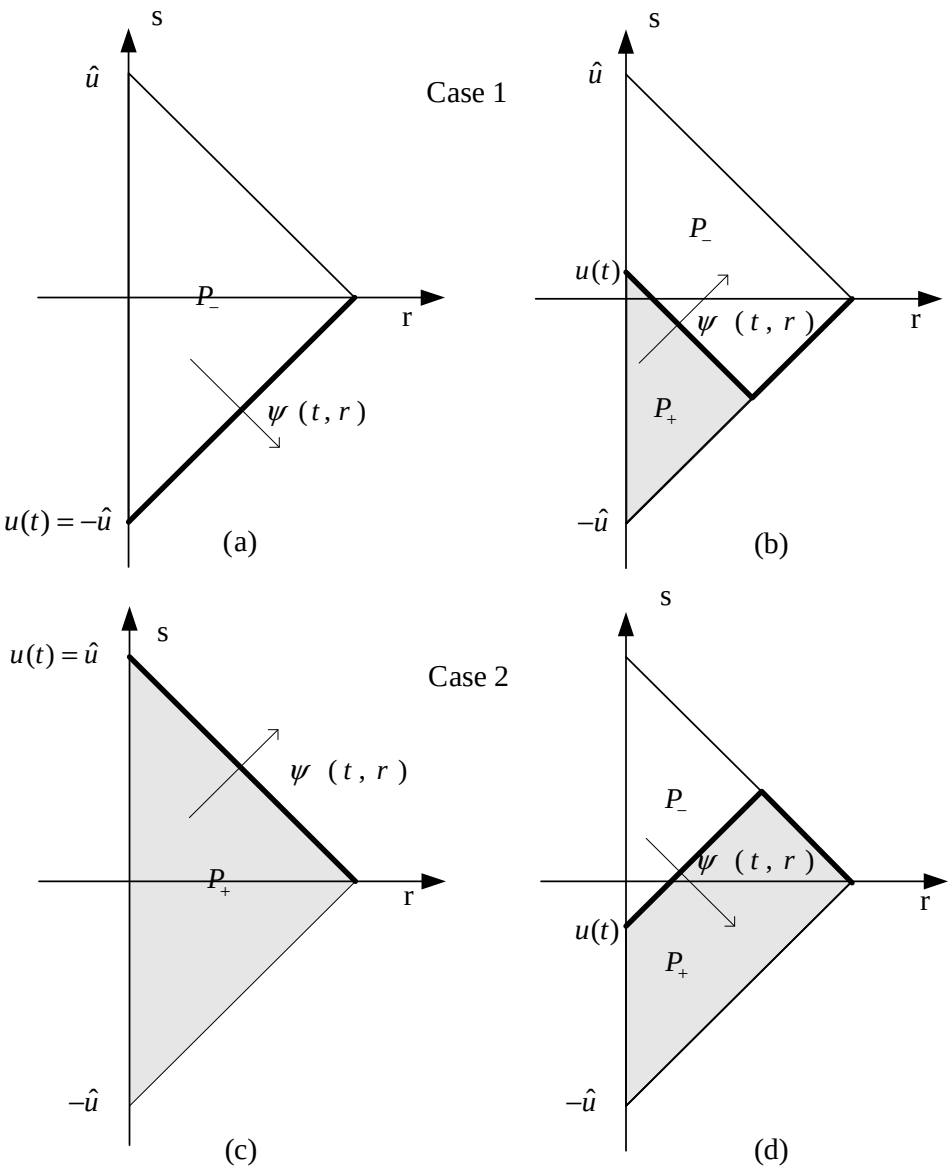

Figure 2.6: Preisach boundary behavior.

sufficient conditions for a certain system to be described by a Preisach model, the wiping-out property and the congruent minor loop property [9]. In the following two subsections, these two properties will be explained in detail.

2.5.1 Wiping-Out Property

As stated in the previous section, input extrema generate the corners of the Preisach boundary which represent the memory of the Preisach model. The wiping-out property indicates that certain input extrema can remove the effects of previous extrema so as to wipe out the memory of the model. Such a behaviour is illustrated in Figure 2.7.

Suppose $u(t)$ starts from 0 to minimum saturation first and the boundary at some time t_3 is as shown in Figure 2.7(a) with the input constant at u_3. There are three corners, namely O_0, O_1 and O_2 shown on the boundary $\psi(t_3, r)$ when $u(t)$ changes its direction at t_0, t_1 and t_2 with input value of $u_0 = -9$, $u_1 = 5$ and $u_2 = -2$. If the input changes its direction at t_3 with input $u_3 = 3$ and decreases from t_3 to t_4, a new segment with $+1$ slope is generated on the boundary, sweeping right downwards through P_r (Figure 2.7(b)). Moreover, a new corner O_3 appears on the boundary. As $u(t)$ keeps decreasing from t_4 to t_5, it reaches and passes the previous input minimum, i.e. $u_2 = -2$. The corners previously generated at time t_2 and t_3, i.e. O_2 and O_3, are "wiped out" (Figure 2.7(c)) and as the input continues to decrease, the memory of the pair of input minimum u_2 and maximum u_3 before t_5 has been removed (Figure 2.7(d)). At any particular time, the previous extrema which remain on the boundary, such as u_0 and u_1 are referred as the *dominant input extrema* by Mayergoyz [9].

2.5.2 Congruent Minor Loop Property

The congruent minor loop (CML) property states that any two minor loops have the same shape independent of past input history if those two minor loops are generated by input variation between the same two distinct values. These minor loops are also defined as comparable minor loops in [47].

Consider two different input signals which generate comparable minor loops through variation between u_2 and u_3 and $u_3 > u_2$. However, those two input signals have different input histories. As stated in Proposition 1, the variation of output $\triangle y$ due to an input variations between u_2 and u_3 is determined by the region Ω and is independent of past input history. As long as $u_2 < u(t) < u_3$, the same triangle (shaded area in Figure 2.8) is swept in both cases. Thus, the output variation from the previous extremum will be identical for both inputs at any point on the minor loop and the two comparable minor loops will have exactly the same shape.

2.6 Preisach Model Identification

Mayergoyz provides a Preisach model identification procedure in [9]. In Chapter 3 of this thesis, this procedure is followed to build the specific Preisach model of the shape control unit SS15. In Mayergoyz's work, a different notation of the hysteresis relay is adopted to describe a Preisach model. As shown by Eq. (2.3), the hysteresis relay is characterized by its half-width $r > 0$ and

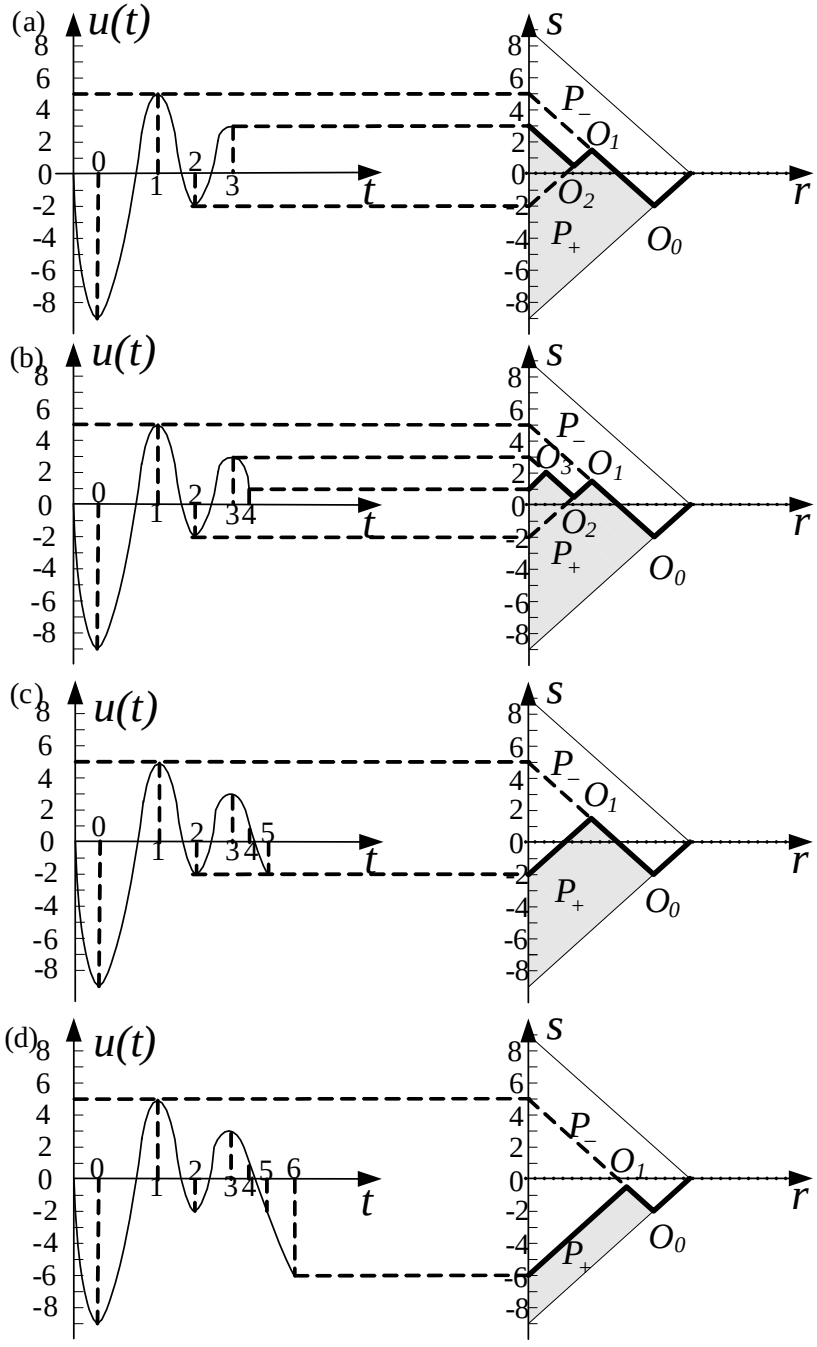

Figure 2.7: Wiping-out property.

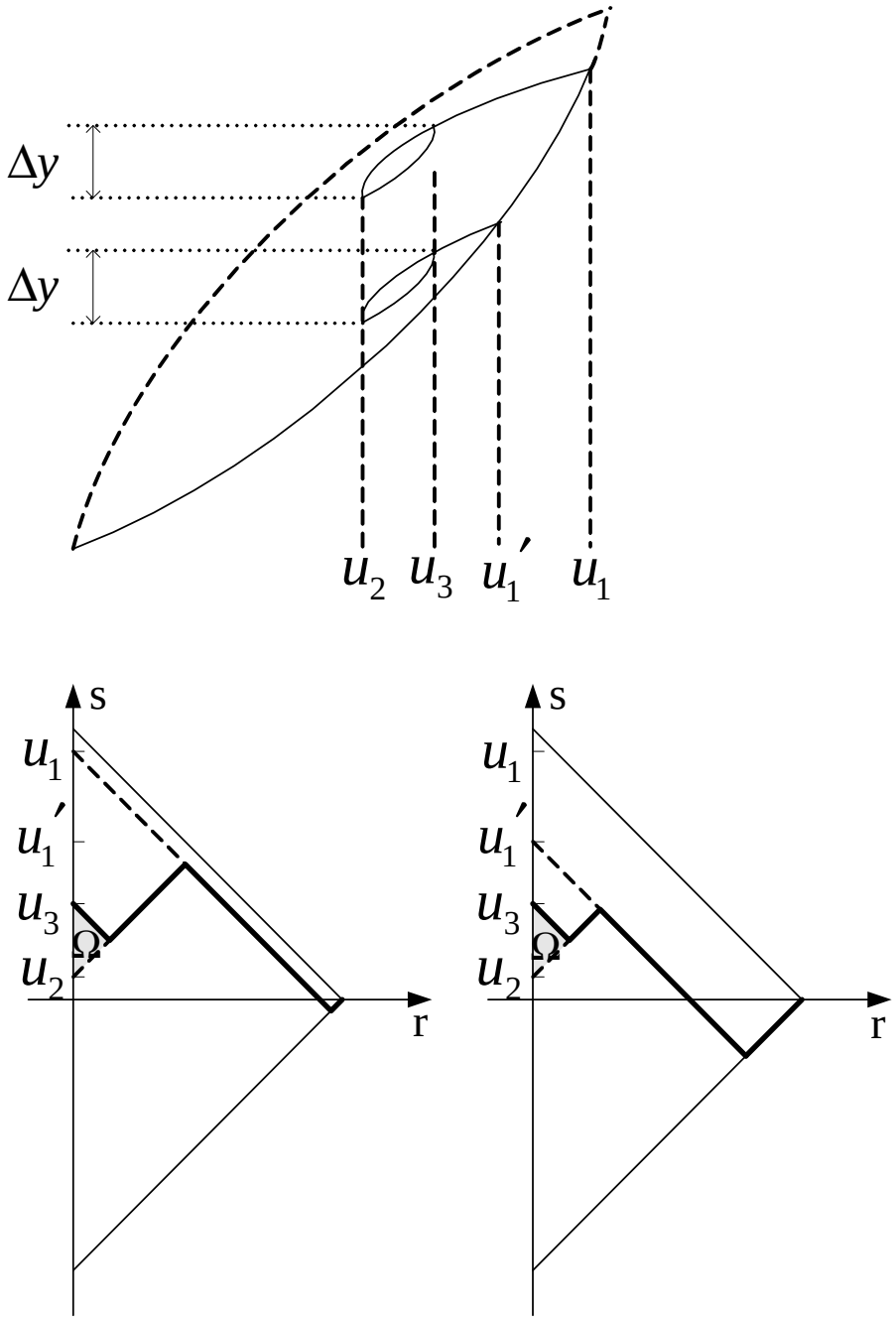

Figure 2.8: Congruent minor loop property.

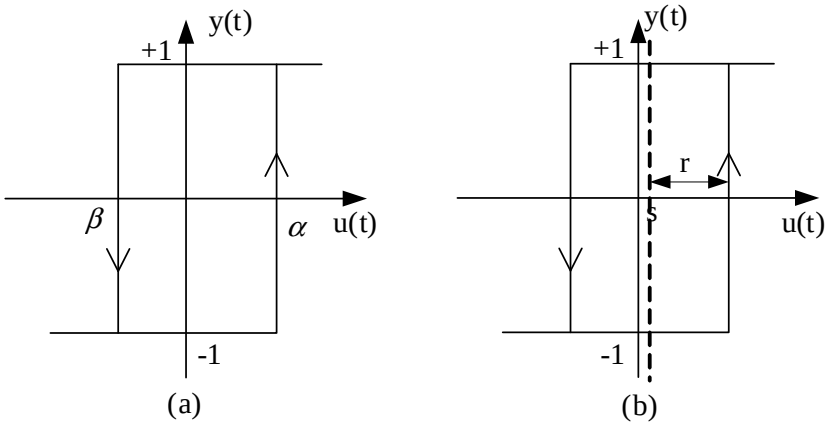

Figure 2.9: Different notation of a hysteresis relay: (a) is in the standard from as suggested by Mayergoyz [9] (b) is a linear transformation of those coordinates as suggested by Gorbet [7] to simplify a mathematical discussion of the model.

input offset s respectively. While in Mayergoyz's work, the hysteresis replay is characterized by its switch on and off values of input α and β respectively. Then the relationship between (α, β) and (r, s) are described as follows:

$$\alpha = s + r \tag{2.9}$$

$$\beta = s - r \tag{2.10}$$

Since $r \geq 0$, then $\alpha \geq \beta$, and (α, β) stands for the pair of switching values of each relay, which is shown in Figure 2.9 (a), while Figure 2.9 (b) shows the hysteresis relay noted by $\gamma_{r,s}$ for comparison. This is only a linear transformation of those coordinates, which can lead to a simplified mathematical discussion of the model due to the effect on the Preisach plane as illustrated in Figure 2.10.

The restricted Preisach plane is shown in Figure 2.10 (b) with $\gamma_{\alpha,\beta}$ as the basic hysteresis relay operator, $\hat{u}$ as the input control saturation and ψ as the Preisach plane boundary generated by input $u(t)$, which is shown in the left part of Figure 2.10. It is shown that a monotonically increasing input generates a horizontal segment of the Preisach plane boundary, while the monotonically decreasing input generates a vertical segment of the boundary in Figure 2.10 (a). The corresponding restricted Preisach plane with $\gamma_{r,s}$ as the basic hysteresis relay operator is shown in Figure 2.10 (b), in comparison to the standard Preisach form under the same conditions.

By using the notation of $\gamma_{\alpha,\beta}$ as the basic hysteresis relay, a first-order descending curve (FOD) can be directly generated by the input $u(t)$ shown in Figure 2.10 (a), i.e. the input $u(t)$ goes to negative input saturation $-\hat{u}$ first, then monotonically increases to a value $u = \alpha_1$, and finally decreases to $u = \beta_1$. Such an input is noted by $u_{\alpha_1\beta_1}$ as used in [47]. The corresponding measured output is denoted by y_{α_1} at $u = \alpha_1$, and $y_{\alpha_1\beta_1}$ at $u = \beta_1$ as shown in Figure 2.11, from which it is illustrated that the final branch of the graph is in the descending direction and only one reversal has appeared before the final branch. Such a branch is named as the first-order descending curve and will be collected in experiments to determine the Preisach weighting surface $\mu(\alpha, \beta)$ first.

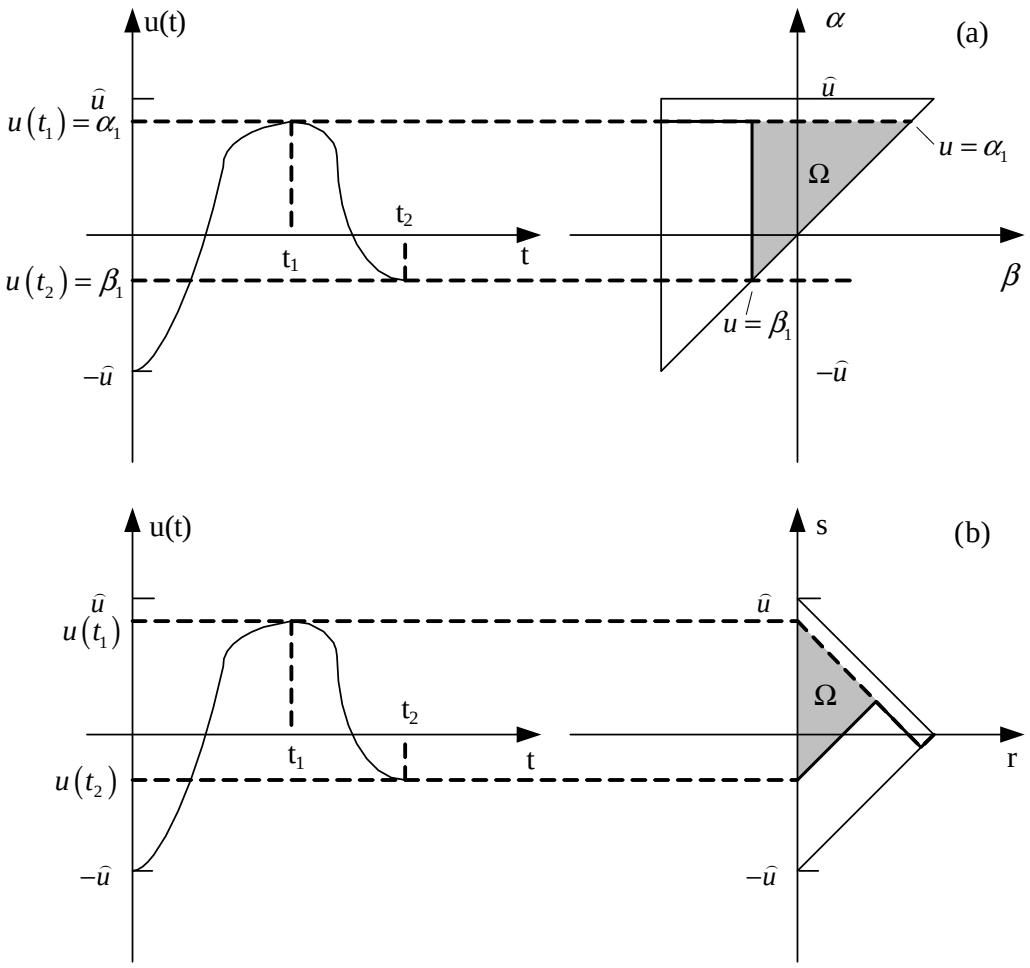

Figure 2.10: Preisach plane comparison based on different notation of a hysteresis relay operator: (a) $\gamma_{\alpha,\beta}$; (b) $\gamma_{r,s}$.

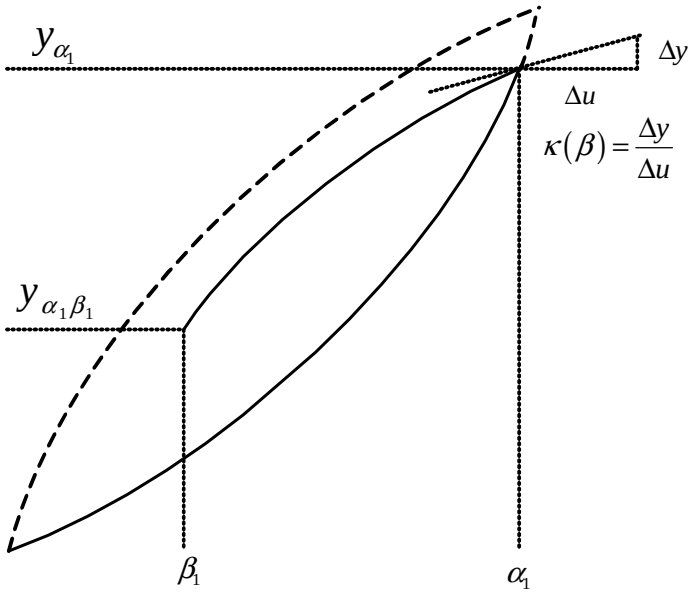

Figure 2.11: FOD curve in I/O plane.

Then from the linear mapping between (α, β) and (r, s), the weighting surface can be converted to the restricted Preisach plane based on the basic hysteresis block denoted by $\gamma_{r,s}$.

As shown in [9], defining the function $F(\alpha_1, \beta_1) = y_{\alpha_1} - y_{\alpha_1\beta_1}$, then

$$\begin{aligned} \mu(\alpha_1, \beta_1) &= -\frac{1}{2}\frac{\partial^2}{\partial\alpha_1\partial\beta_1}F(\alpha_1, \beta_1) \\ &= \frac{1}{2}\frac{\partial^2 y_{\alpha_1\beta_1}}{\partial\alpha_1\partial\beta_1} \end{aligned}$$

All points $y_{\alpha\beta}$ could be identified for the whole restricted Preisach plane P_r and form the surface $y(\alpha, \beta)$. From a physical point of view, the surface $y(\alpha, \beta)$ should be smooth and then it can be differentiated to generate the weighting function

$$\mu(\alpha, \beta) = \frac{1}{2}\frac{\partial^2 y(\alpha, \beta)}{\partial\alpha\partial\beta} \tag{2.11}$$

In [45] another form of the weighting surface is used in building the Preisach model of piezoceramic and SMA hysteresis. The weighting surface now is separated into two parts:

$$\mu(\alpha, \beta) = v(\alpha, \beta) + \kappa(\beta)\,\delta(\alpha - \beta). \tag{2.12}$$

$v(\alpha, \beta)$ represents the hysteretic effect and is a continuous surface, and $\kappa(\beta)$ represents the reversible behaviour of the material. Moreover, $\kappa(\beta)$ is the magnitude of the slope of the FOD curve at the point where it branches off the major loop due an input reversal at $u(t) = \beta$, as

shown in Figure 2.11 [45]. With the distribution $\kappa(\beta)\,\delta(\alpha-\beta)$ along $\alpha=\beta$, this form of weighting surface will illustrate the hysteresis of piezoceramic more precisely because reversible behaviour can also be described by such a weighting surface and it is not over constrained to be continuous as $\beta \to \alpha$. Recall Eq. (A.28). The initial slopes of the FOD curves will be always zero if the weighting surface is restricted to be continuous in P_r, which is clearly not true as shown in Figure 2.11. Thus, the weighting surface in this thesis is considered and identified in the form of Eq. (2.12), where

$$v(\alpha,\beta) = \frac{1}{2}\frac{\partial^2 y(\alpha,\beta)}{\partial\alpha\partial\beta} \tag{2.13}$$

$$\kappa(\beta) = \frac{1}{2}\left.\frac{\partial y(\alpha,\beta)}{\partial\beta}\right|_{\beta\uparrow\alpha} \tag{2.14}$$

Practically the input range is divided into n sections, defined by $\{u_i\}$ where i is from 0 to n. Then for all pairs (u_i, u_j), where $j \le i$, FOD curves can be generated and $\frac{n}{2}(n+3)$ FOD data points can be collected. In this thesis, it is assumed that the input $u(t)$ is continuous, then the FOD curves are smooth in nature from the physical point of view. Then a smooth surface $\tilde{y}(\alpha,\beta)$ is fit to those FOD data points by the least-squares method and the smooth surface $\tilde{y}(\alpha,\beta)$ is differentiated to obtain an approximate weighting surface $\tilde{\mu}$. In the thesis, a Nelder-Mead simplex algorithm is used to do the least-squares fit. It should be noted that, for those FOD curves with few data points, the simplex algorithm is likely to fail to converge and result in many minima since the data points on those curves exhibit the linearity, and a nonlinear candidate function is used in curve fitting in order to fit the curvature of most FOD curves. In order to avoid divergence of the algorithm, the identified parameters of the candidate function for the previous FOD curve is used as the initial condition of those parameters of the candidate function for the next FOD curve. Moreover, when we choose the candidate function, there is always a trade-off between accuracy and stability for the model to be identified.

2.7 State-Space Representation of Preisach Model

A state-space representation of Preisach models is developed in [48]. This concept is introduced in order to discuss the influence of the initial *states* during control with hysteretic actuators. The system is defined through the input, output and state spaces U, Y and Ψ respectively, together with the state transition operator ϕ and the read-out operator Γ_r.

The input space U is defined as

$$U = \left\{ u \in C^0(-\infty,\infty) : \|u(t)\|_\infty \le \hat{u} \text{ and } \lim_{t\to-\infty} u(t) = 0 \right\} \tag{2.15}$$

where $\hat{u}$ is positive number depending on system itself. The output space Y is the set of real-valued continuous functions $C^0(-\infty,\infty)$. As stated previously the Preisach boundary ψ represents the memory of the Preisach model, so it is a natural state choice.

Definition 1 *[State-Space]* [48] *The state-space Ψ is defined to be the set of continuous functions $\psi : [0,\hat{u}] \to R$ which satisfy the following properties:*

$$\begin{aligned} &\text{Lipschitz condition:} && |\psi(r_1) - \psi(r_2)| \le |r_1 - r_2|,\ \forall r_1, r_2 \in [0,\hat{u}] \\ &\text{initial condition:} && \psi(\hat{u}) = 0 \end{aligned}$$

So the state-space Ψ is the subset of Lipschitz continuous $\psi \in C[0, \hat{u}]$ with $\psi(\hat{u}) = 0$ and the Lipschitz constant $L = 1$.

The state transition operator $\phi : R^2 \times \Psi \times U \rightarrow \Psi$ satisfies the properties of consistency, determinism, semi-group and stationarity [48].

Given the desired output $y_d \in Y$, suppose all the states start from a state of zero stored energy, such as the anhysteretic state for which the boundary corresponds to the line $\alpha = -\beta$ or $s = 0$, in which no remnant hysteresis is present. In other words, no remnant polarization exists in the piezoceramics or no memory is stored. Let ψ_{ini} denote the initial boundary, which is assumed to be the line $s = 0$. The state transition operator ϕ determines the state $\psi = \phi(t_1, t_0, \psi_0, u(t))$ which results at time t_1 from applying an input $u(t) \in [t_0, t_1]$ to a system starting in state ψ_0 at time t_0. For this operation to be well-posed, the state ψ_0 must be reachable and $u(t)$ must be admissible to ψ_0; that is $u(t_0) = \psi(t_0, 0)$. According to [48], even though the entire state-space Ψ is not exactly reachable, it is approximately reachable in L_1 norm.

The read-out operator Γ_r provides the system output corresponding to a particular state ψ. Recall the Preisach model output in Eq. (2.4). Clearly, relays have output $+1$ below the boundary and output -1 above the boundary. The read-out operator can be defined as a function of ψ:

$$y(t) = \Gamma_r(\psi(t)) = \int_0^{\infty} \int_{-\infty}^{\psi(t)} \mu(r, s)\, dsdr - \int_0^{\infty} \int_{\psi(t)}^{\infty} \mu(r, s)\, dsdr \tag{2.16}$$

If μ is bounded, piece-wise continuous, and non-negative inside P_r, then the set of μ is named M_p. It has been shown in [47] that if μ is bounded and piece-wise continuous then $\Gamma_r : C^0 \rightarrow C^0$. Moreover if $\mu \in M_p$, then $\Gamma_r : W_1^2 \rightarrow W_1^2$. W_1^2 is the Sobolev space which is the space of real-valued functions satisfying $\int_{-\infty}^{\infty} \left(\dot{u}^2 + uH2\right) dt < \infty$.

2.8 Neutral State Definition and Discussion

The advantages of the neutral state is investigated in this thesis. Thus, the definition of equivalent states is described mathematically, and the neutral state is defined graphically in this section.

For a given Preisach system with weighting surface μ and a desired output $y_d \in [y_-, y_+]$, there exists a range $[u_1, u_2] \in [-\hat{u}, \hat{u}]$, where $y = y_d$, as shown in Figure 2.12.

Definition 2 *[Equivalent State] Given a Preisach system with readout operator: $\Gamma_r(\Psi) \longrightarrow Y$ and a desired output $y_d \in Y$, the set of equivalent states $\Psi_{eq}^{y_d}$ is defined as*

$$\Psi_{eq}^{y_d} = \{\psi \in \Psi : \Gamma_r(\psi) = y_d\}$$

Figure 2.12 shows the boundaries corresponding to the points on the major hysteresis loop at (u_1, y_d) and (u_2, y_d), such that both ψ_1 and $\psi_2 \in \Psi_{eq}^{y_d}$ and $\Gamma_r(\psi_1) = \Gamma_r(\psi_2) = y_d$.

As demonstrated in [7] from experimental results, there exists specific states $\psi_n^{y_d}$ in Ψ_{eq}^{d} which hold an attracting property such as high noise rejection, and thus this observation provides one more degree of freedom to accomplish the open-loop regulation task for a hysteretic system. Then the open-loop regulation task can be considered as choose the initial state $\psi_n^{y_d}$ and design an input $u_d(t)$ to drive the hysteretic system to that state, so that the derivative of the output with

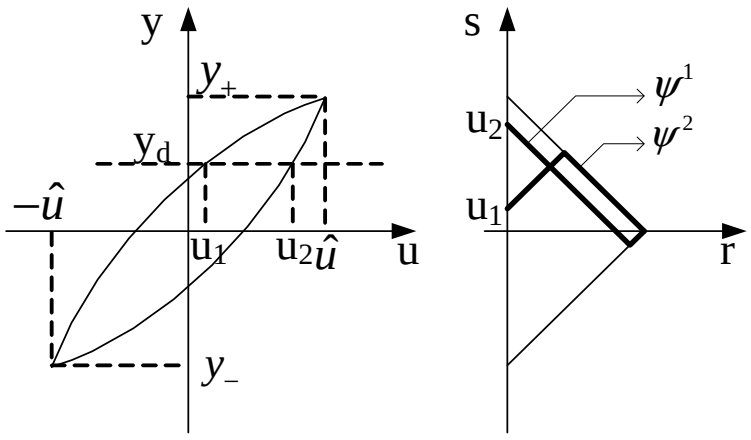

Figure 2.12: Input range of a given desired output.

respect to the input during open-loop regulation in the presence of input noise is minimized, i.e. the maximum output transient caused by noises is minimized.

The state space representation is adapted [7] in order to discuss the so-called neutral states for a given desired output y_d. Moreover, the neutral state is defined graphically on the Preisach Plane. According to [7], there exist one or more states which result in better natural rejection of random input disturbances among those multiple states for a given desired output y_d. Any of these states can be chosen as the neutral state, ψ_n^l, which is approximately reached by ψ_n. The advantages of the neutral state have been demonstrated by means of both simulations and experiments in open-loop and closed-loop tests. [7] also illustrates a neutral state on the Preisach plane, which can only be approximately approached, since it contains a horizontal segment. For instance, the neutral states $\psi_n^{l_1}$ and $\psi_n^{l_2}$ are shown in Figure 2.13 and can be described by Eq. (2.17) in a general format. In particular, when $l = l_1 > 0$, the Preisach boundary $\psi_n^{l_1}$ consists of the horizontal segment $s = l_1$ ($r \in [0, \hat{u} - l_1]$) and the segment $s = -(r - \hat{u})$ ($r \in (\hat{u} - l_1, \hat{u}]$). If $l = l_2 < 0$, then the Preisach boundary $\psi_n^{l_2}$ consists of the horizontal segment $s = l_2$ ($r \in [0, \hat{u} + l_2]$) and the segment $s = r - \hat{u}$ ($r \in (\hat{u} + l_2, \hat{u}]$).

$$\begin{array}{lll} \psi_n^l \quad : & s = l & \text{if } 0 \le r \le \hat{u} - |l| \\ & s = -sgn(l) \cdot (r - \hat{u}) & \text{if } \hat{u} - |l| < r \le \hat{u} \end{array} \tag{2.17}$$

A theorem is provided in [7] which states that given $l \in [-\hat{u}, \hat{u}]$, $u_l \in U$ can be constructed so that $\psi^l = \phi(t_1, t_0, \psi_0, u_l)$ approximates ψ_n^l arbitrarily closely in the metric on Ψ, for any $\psi_0 \in \Psi$ and $t_1 > t_0$. Moreover, the output corresponding to the boundary ψ_n^l is defined as $N(l)$ and can be defined by the following equation:

$$N(l) \triangleq \Gamma_r\left(\psi_n^l\right) = 2\int_0^{\infty}\int_0^{\psi_n^l} \mu(r,s)\, ds dr + y_0 \tag{2.18}$$

In addition, if μ is piece-wise continuous, then $N(l)$ is continuous in l and there exists a value $l \in [-\hat{u}, \hat{u}]$ such that $N(l) = y_d$ for every $y_d \in [y_-, y_+]$, where y_- and y_+ are the output of the

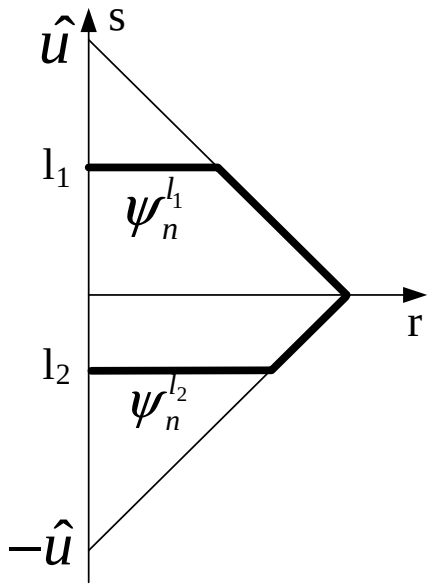

Figure 2.13: Neutral state illustrated on preisach plane.

Preisach model when the inputs are at negative and positive saturation respectively [7]. Moreover, if μ is positive in P_r additionally, i.e. $\mu \in M_p$, then $N(l)$ is monotonic and l is unique for a given y_d. Let N^{inv} represent the inverted function of $N(l)$ defined as Eq. (2.18). If $\mu \in M_p$, then $N(l)$ is invertible and N^{inv} is defined to be

$$N^{inv} \equiv N^{-1} \tag{2.19}$$

Otherwise N^{inv} is defined below according to [7]:

$$N^{inv}(y) \triangleq \min\left\{ \ |l| \quad l \in [-\hat{u}, \hat{u}] \ \ : N(l) = y \right\} \tag{2.20}$$

As indicated in [7] the locus N appears to connect those points inside the major hysteresis loop where internal ascending and descending branches have similar slopes.

It should be noticed that, there may be multiple values of l corresponding to the same output y_d in cases where $N(l)$ is non-monotonic. As shown in Figure 2.14, there exists distinct equivalent neutral states ψ_{n1}^d and ψ_{n2}^d for a given desired output y_d. According to Eq. (2.20), the value with the smallest $|l|$ should be taken in this case, which means that the last horizontal segment of the Preisach boundary should be the longest. Thus, ψ_{n2}^d in the case shown in Figure 2.14 should be taken as the neutral state according to the definition in [7].

Subsequently, Chapter 3 introduces the experimental setup of a hysteretic system, for which the Preisach model is identified. Chapters 4 and 5 will apply these concepts to data from the experimental apparatus where the notion of neutral state noise rejection is demonstrated.

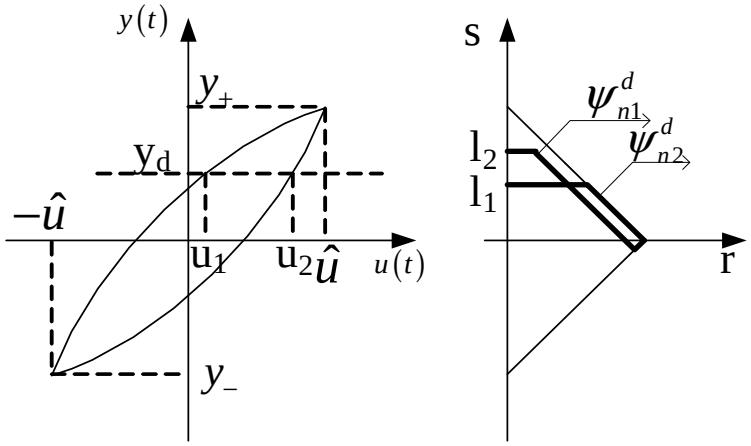

Figure 2.14: Different neutral states of a given desired output.

Chapter 3

Experimental Setup and Model Identification

In this chapter, a Preisach model is constructed in order to model the hysteresis behaviour of a piezoelectric actuator in a custom-designed shape control unit (Sensor Technologies SS15). The first section introduces the system structure and the important parameters. The second section describes the calibration process of the entire shape control system.

As detailed in Section 2.5, the wiping-out property and congruent minor loop property are the necessary and sufficient conditions for a hysteresis loop to be modeled using a Preisach model [9]; and these conditions are discussed in Section 3.3 as the representation tests.

The ensuing Preisach model is built for the shape control system by following the identification procedure described in Section 2.6. FOD (First Order Descending) data is collected and subsequently curve and surface fitting techniques are used to represent this data. Subsequently, the Preisach model is verified by comparing the output of the model with the collected experimental output data corresponding to the wiping-out test, the congruent minor loop test and the FOD curves.

3.1 Experimental Apparatus

The computer based shape control system setup is described and a photograph of the apparatus is shown in Figure 3.1.

The SS15, designed by Sensor Technology Limited, can be used to study and improve the understanding of the hysteretic behaviour of piezoceramic actuators and to determine better and more useful ways of using piezoceramic materials. The SS15 consists of four piezoceramic bimorph actuators arranged in a manner to control the orientation of a central circular platform (see Figure 3.2). The bimorphs act in pairs as shown in Figure 3.2 (a), bending out of plane based on the applied voltage, and affecting the pitch and yaw of the central platform. The bimorph actuators act as bender actuators, namely, Flexmorphs as termed by Sensor Technology. External high-voltage is used to drive each of the Flexmorphs, which are the piezoelectric flexure elements.

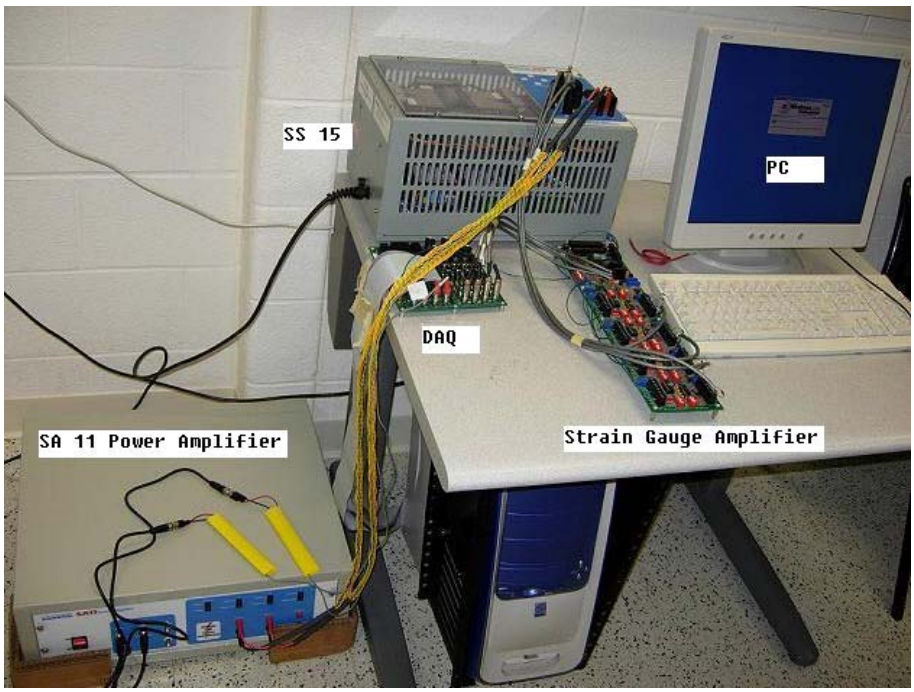

Figure 3.1: Computer based shape control system.

Flexure elements consist of two plates of PZT (an abbreviation of the chemical formula of lead-zirconate-titanate) bonded together with electrodes and are arranged in a parallel configuration in the SS15. The strain experienced by each of the bimorphs is indicative of their bending and allows the orientation of the central platform to be determined. Thus, the desired orientation of the circular platform could be achieved with the proper voltage across each bimorph.

In the experiments for the present work, the circular platform is released from the bimorphs in order to focus on the hysteresis behaviour generated by the piezoelectric actuator itself without interference from additional mechanical parts. Thus, in this system the input is the voltage applied to the biomorph piezos by the SA11 amplifier and the output is the deflection of the bimorphs as determined by the voltage generated by the strain gauge amplifier.

In order to supply control voltage to the SS15 and measure the strain on each bimorph, a data acquisition board is used in the system. In this experiment the Quanser[1] Data Acquisition Card (DAQ) is used (model number: Quanser PCI MultiQ - V1), which can produce analog output voltages in the range of ± 10 V by using DACs (digital to analogue converters), and read analogue voltages in the range (-5, +5) volts by using ADCs (analogue to digital converters).

On the input side, each Flexmorph has two layered piezoceramic plates connected in parallel where one plate has the opposite polarity with respect to the other. The Flexmorph tip displacement increases with the magnitude of the applied voltage. For these bimorphs, voltages with magnitudes in excess of 100 V produce noticeable deflection. As recommended by the manufacturer, the input voltage should lie between ± 200 V [23]. A high voltage amplifier is needed to amplify the output voltage from the data acquisition card so that the range of the supplied voltage is large enough to bend the Flexmorphs noticeably. Using the Sensor SA11 high voltage amplifier with the Quanser DAQ can supply a voltage in the range of ± 135 V. Although the limits of this voltage range are not sufficient to drive the Flexmorphs to their extreme limits, this supplied voltage is sufficient for the current experiments towards hysteresis modelling. It is assumed that the input voltage to SS15 generated by SA11 directly affects the identified Preisach model and other effects are negligible.

On the output side, as shown in Figure 3.2, each bimorph has a SG-7/350-LY13 strain gauge from Omega Engineering attached to each side. The strain gauges have a resistance of 350 Ohms and a nominal gage factor of 2.0 [49]. When the Flexmorphs bend, the resistance of the strain gauges attached to the Flexmorphs plate changes. The SS15 provides an output connection which connects directly across the strain gauges. Figure 3.3 shows how the 3 pin female XLR connector is connected across the strain gauges.

Figure 3.4 shows the relative positioning of the two strain gauges on a piezoceramic bimorph with one on each side. It should be noted that when the material is driven by a high voltage causing the bimorph to bend, one strain gauge undergoes tension and the other undergoes compression. For ease of calculation, the change in resistance on the two strain gauges is considered to be the same magnitude. The half-bridge configuration for a Wheatstone bridge is capable of the precise comparisons, and thus, it is suitable to measure the resistance change in the strain gauges. The strain gauge transforms applied strain into a proportional change in resistance. The bridge circuit is shown in Figure 3.5 and the excitation voltage (V_{ex}) supplied to the bridge is set at 4 V.

The resistance variation obtained from the strain gauges on the SS15 bimorphs is approximately 0.0525 Ohms [51], so the output of the strain gauge is 0.3 mV in magnitude. The inputs

[1] Quanser Inc. Markham, Ontario, Canada.

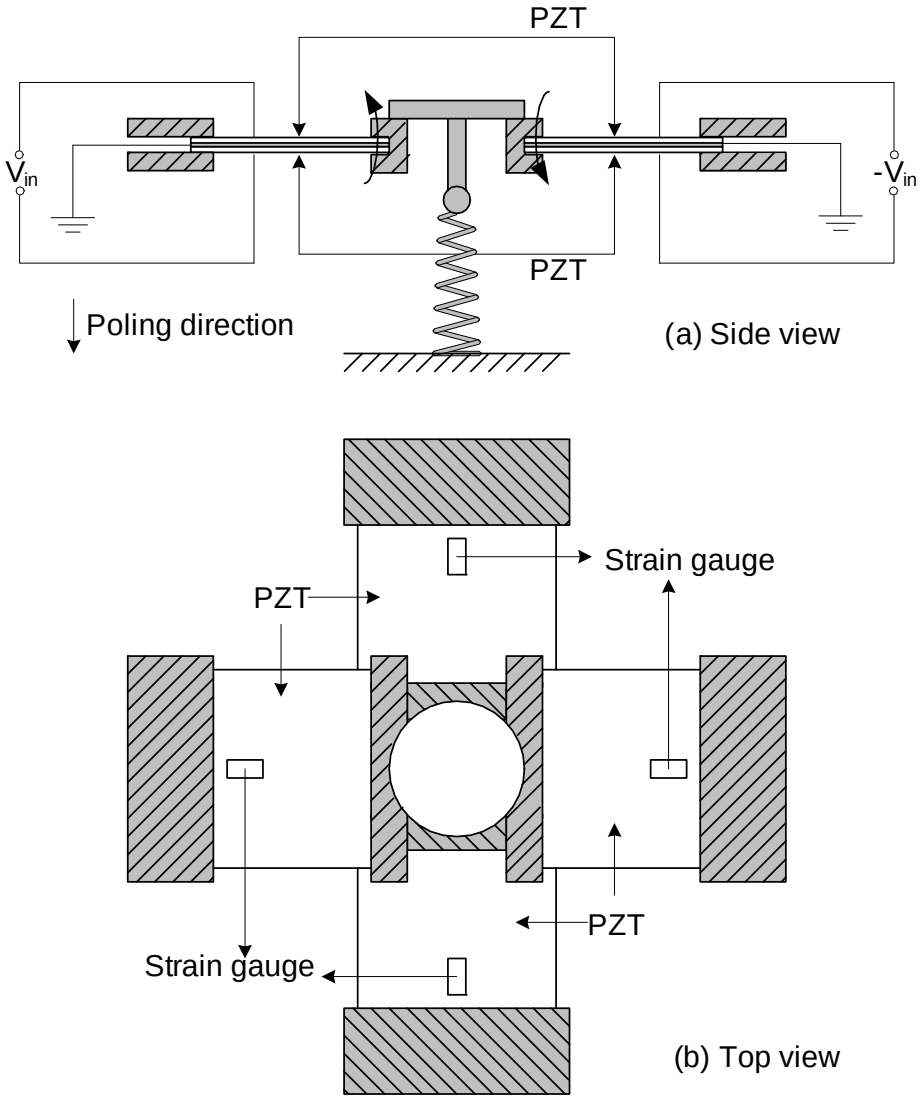

Figure 3.2: Shape control unit SS15 schematic prior to the removal of the circular platform.

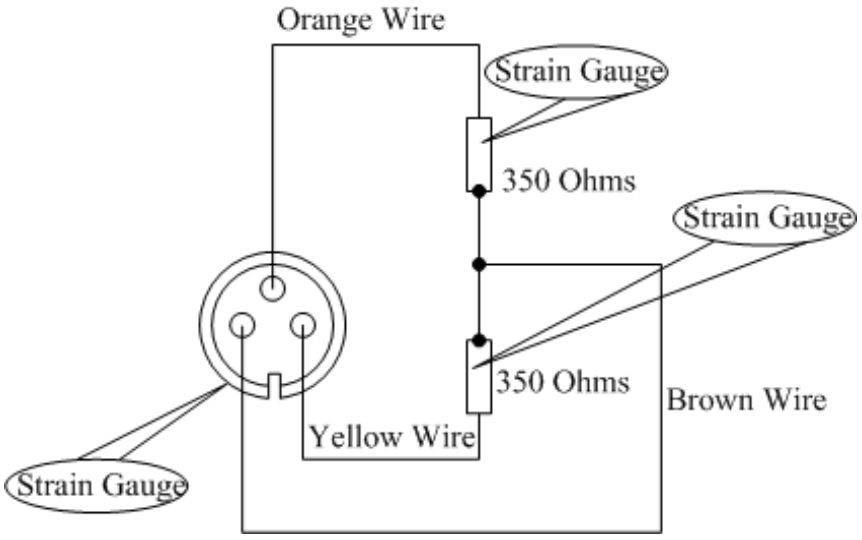

Figure 3.3: Strain gauge wiring [23].

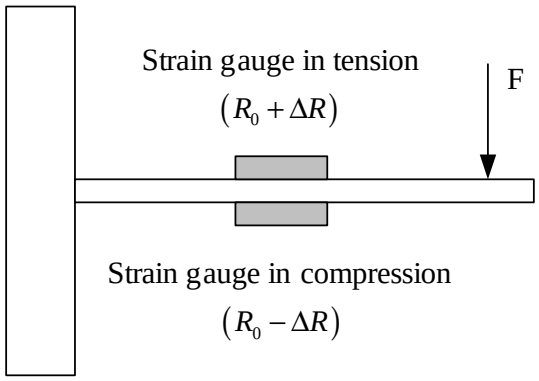

Figure 3.4: Strain gauges mounted on a piezoceramic plate experiencing strain [50].

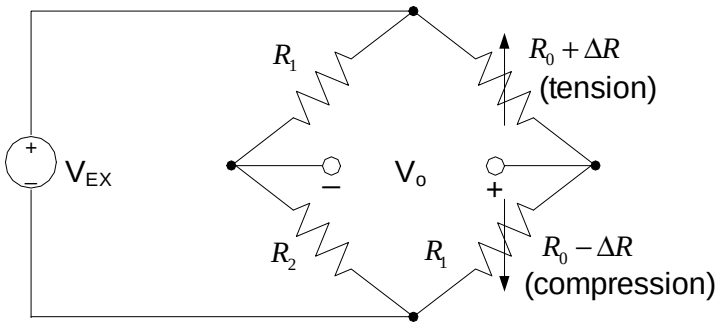

Figure 3.5: Half bridge configuration for a Wheatstone bridge [50].

read from the data acquisition card only have a resolution of 0.6 mV. Therefore, such small output voltages as obtained from the bridge cannot be precisely read from the DAC. Proper amplification of this voltage is required in order to acquire higher precision in the calculations. The CIO-EXP-GP manufactured by ComputerBoards Inc. is a common strain gauge amplifier which is highly customizable to the needs of the experiment and can be easily configured to suit the current setup. The strain gauge amplifier has eight input channels where each channel has the ability to amplify the voltage up to a maximum 1000 times of its current value (0.3V max magnitude of output voltage). However, this amplification is still not sufficient and further amplification is required. Since the SS15 has four bimorphs, only four of the eight channels of the strain gauge amplifier are used. The remaining four channels are used for further amplification of the output voltage obtained out of the currently connected channels. Finally, a gain of 10000 is achieved through the strain gauge amplifier (CIO-EXP-GP) and a 3 V maximum output voltage is achieved. There are variable resistors used to adjust the offset to achieve a 0 V output from the board when there is no strain applied on the Flexmorphs. With this signal preparation, the computer based system setup is ready to implement the experiment for the hysteresis modelling. For calibration details of the interface with the SS15, please see Appendix B.

3.2 Preisach Model Suitability Test

As stated in [9], the wiping-out and congruent minor loop properties are the sufficient and necessary conditions to describe hysteresis behaviour with the Preisach model. Therefore, these two tests are performed to demonstrate that the hysteresis relationship between the input voltage and the amplified output voltage of the SS15 can be represented by Preisach modelling. In order to produce repeatable results, a decaying sinusoidal input voltage is applied to the SS15 before each test in order to approximate the anhysteretic state so that all traces of remnant hysteresis can be removed before a new trial [52]. This process is called initialization.

3.2.1 Wiping-Out Test

As stated in Section 2.5, the wiping-out property is one of the two necessary and sufficient conditions for a certain hysteretic system to be described by the Preisach model. For the wiping-out

test, the input voltage Vb_{in} of the power amplifier (SA11) is controlled via the Quanser DAC. Signals at frequencies of $f = 1$, 2 and 4 Hz used in the test. After initialization, the high input voltage of the SS15 V_{in} goes to negative saturation and the wiping-out test input signal is applied as shown in Figure 3.6 (a), which starts at testing time $t = 12$ s. In Figure 3.6 (a), T represents the input signal period, i.e. $T = 1/f$. The two marked segments (A & B) generate four nested branches. Then the output V_{out} generated by high input voltages with the frequencies $f = 1$, 2 and 4 Hz are shown with respect to time in Figure 3.6 (b) through (d). If the hysteresis of the SS15 satisfies the wiping-out property, then the peak at the beginning of segment B should be able to remove any memory of the input up to that point, and the loops traced for input segment B shown by the dash-dotted curve should re-trace exactly those generated by segment A as shown by the solid curve. Moreover, the output data points are also shown in Figure 3.6 (b) through (d) when the input signals first achieve zero from negative saturation. Note that the absolute values of these outputs become larger when the input frequency increases, which means that the major hysteresis loops of the piezoceramic actuator becomes wider when the input signal is higher in frequency.

From the input-output graph shown from Figure 3.7 through Figure 3.9, the loops can be retraced exactly for all input signals with various frequencies. However, the peak at the start of segment B does not exactly remove all the memory of the input up to that point. If we define that the first increasing segment of the input generates the first ascending branch, then the increasing input between segments A and B generates the fourth ascending branch. During segment A there are second and third ascending branches. The difference between the 1st and 4th, 2nd and 4th, 3rd and 4th ascending branches are shown from Figure 3.10 through Figure 3.12. According to the wiping-out property, it is expected that, at points $V_{in} = -98.85$, -70.61, and -42.37 V the difference should be equal to zero. There exists a maximum offset of 0.080 V, 0.18 V, and 0.32 V from 0 (these represent the possible modelling errors) when the frequency of the input signal is $f = 1$, 2, and 4 Hz respectively as shown by Datatips[2], which allow to read data directly from a graph by displaying the values of points selected on plotted curves, in these figures. Note that the output is in the range of $[-3.5, 3.5]$ V and the largest offset 0.32 V is within 5% of the whole output range. Thus, this is considered to be sufficiently close to zero and it is concluded that the wiping-out property for the hysteresis of the SS15 is satisfied. It is also expected that the higher input frequency results in increasing offset. However, the classical model introduces a maximum 5% error by this measurement. The theory for the effect of initial states has not yet been extended to dynamic models [7], and thus, the classical model is used as a first pass to investigate the influence of initial states in this thesis. Since the present work uses the classical model for the described application, future work could investigate the necessity, and conditions required for a dynamic model.

3.2.2 Congruent Minor Loop Test

As noted in Section 2.5, the congruency property is the other necessary and sufficient condition to ensure that a hysteretic system can be described by the Preisach model. The results of the congruent minor loop (CML) test of the input signal with frequencies $f = 1$, 2 and 4 Hz are shown in Figure 3.13. The test input voltage V_{in} signal is shown from $t = 12$ s in Figure 3.13 (a), which is applied to generate two minor loops. On the x-axis of Figure 3.13 (a), $T = 1/f$. If the hysteresis loop for the SS15 supports the congruent minor loop property, then these two minor

[2]Data Exploration Tools (Graphics) of Matlab Version 7.5.0.342 (R2007b)

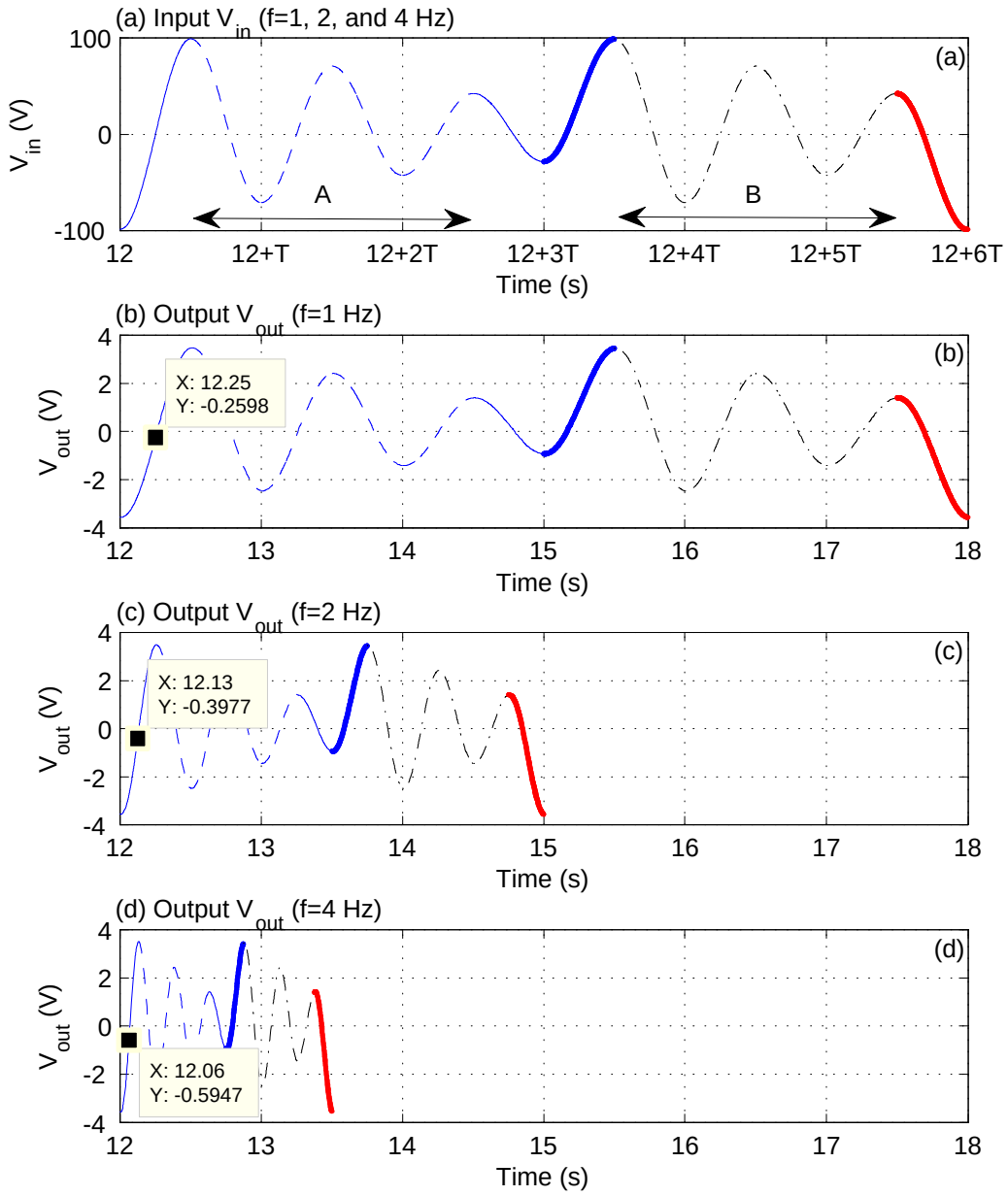

Figure 3.6: Input voltage V_{in} and strain gauge output voltage V_{out} w.r.t time t in wiping-out test with different frequencies.

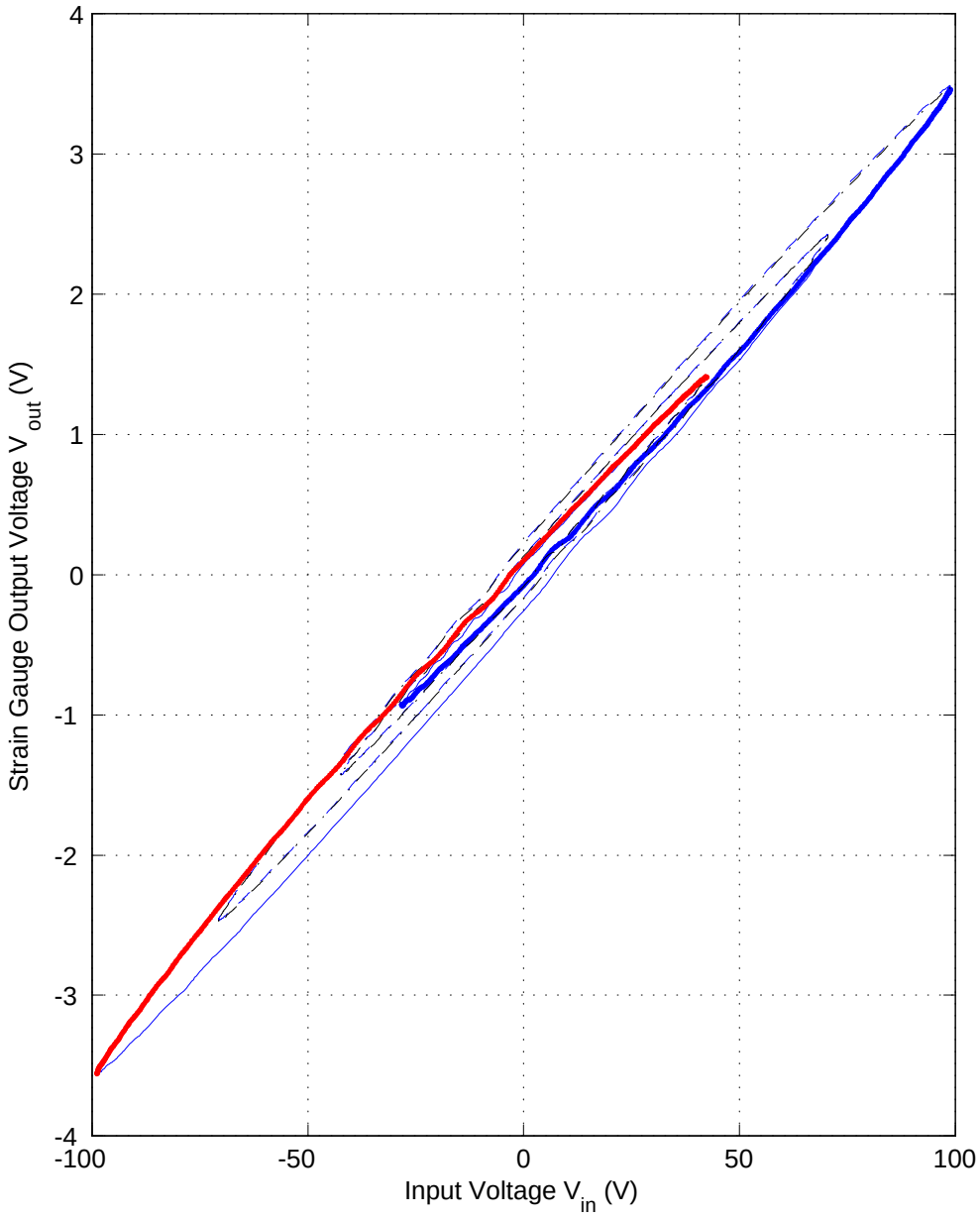

Figure 3.7: Input V_{in} vs output V_{out} in the wiping-out test at $f = 1$ Hz.

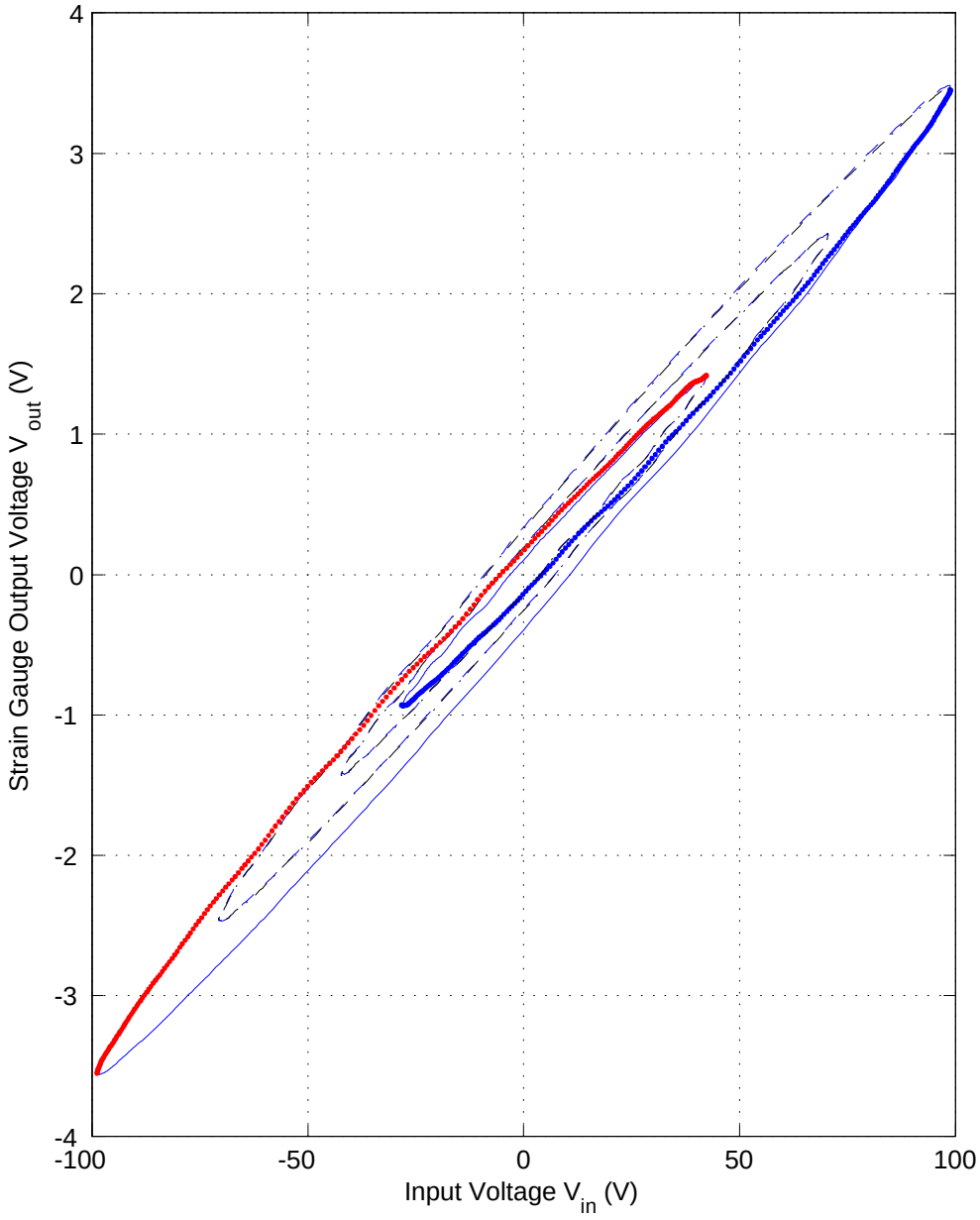

Figure 3.8: Input V_{in} vs output V_{out} in the wiping-out test at $f = 2$ Hz.

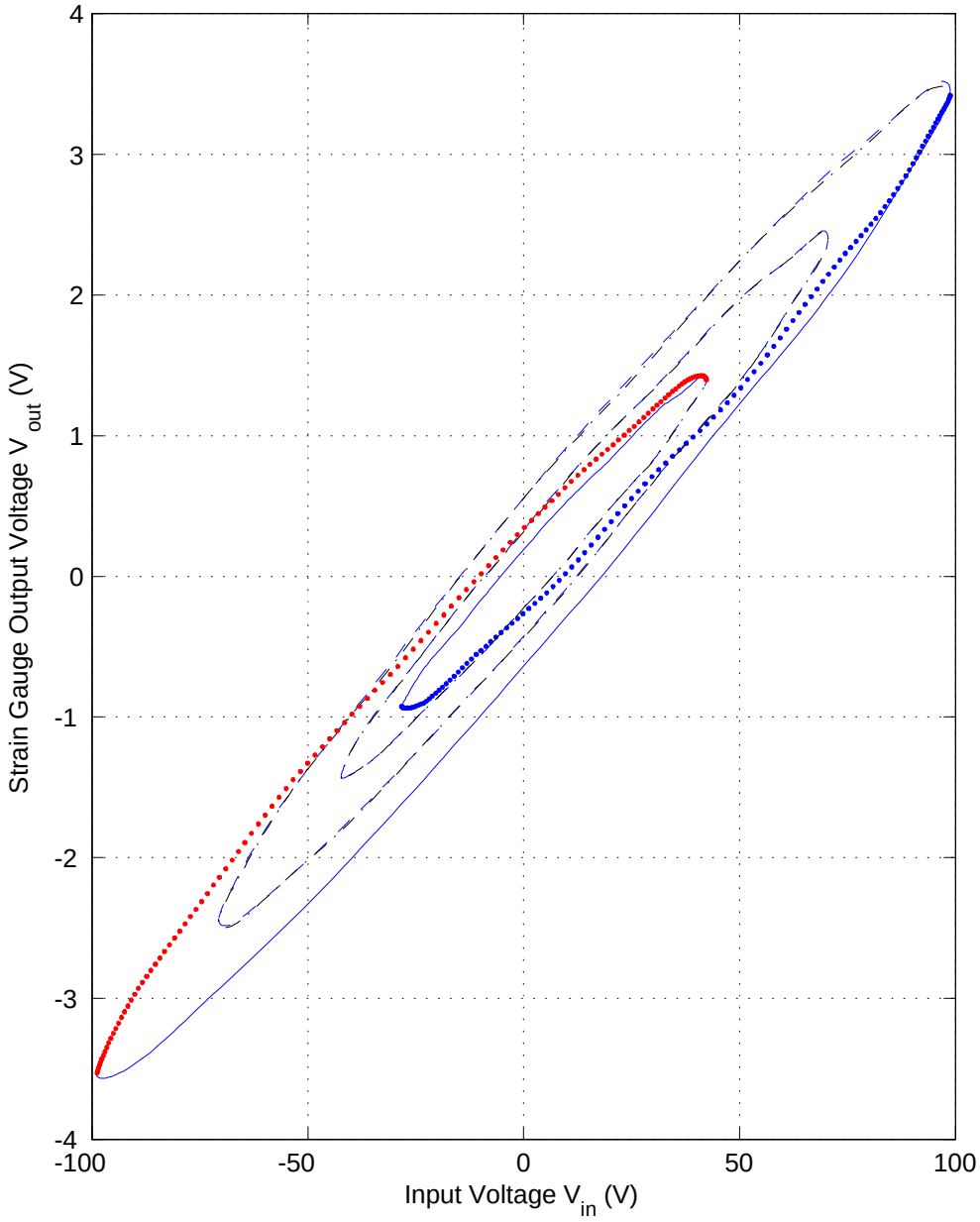

Figure 3.9: Input V_{in} vs output V_{out} in the wiping-out test at $f = 4$ Hz.

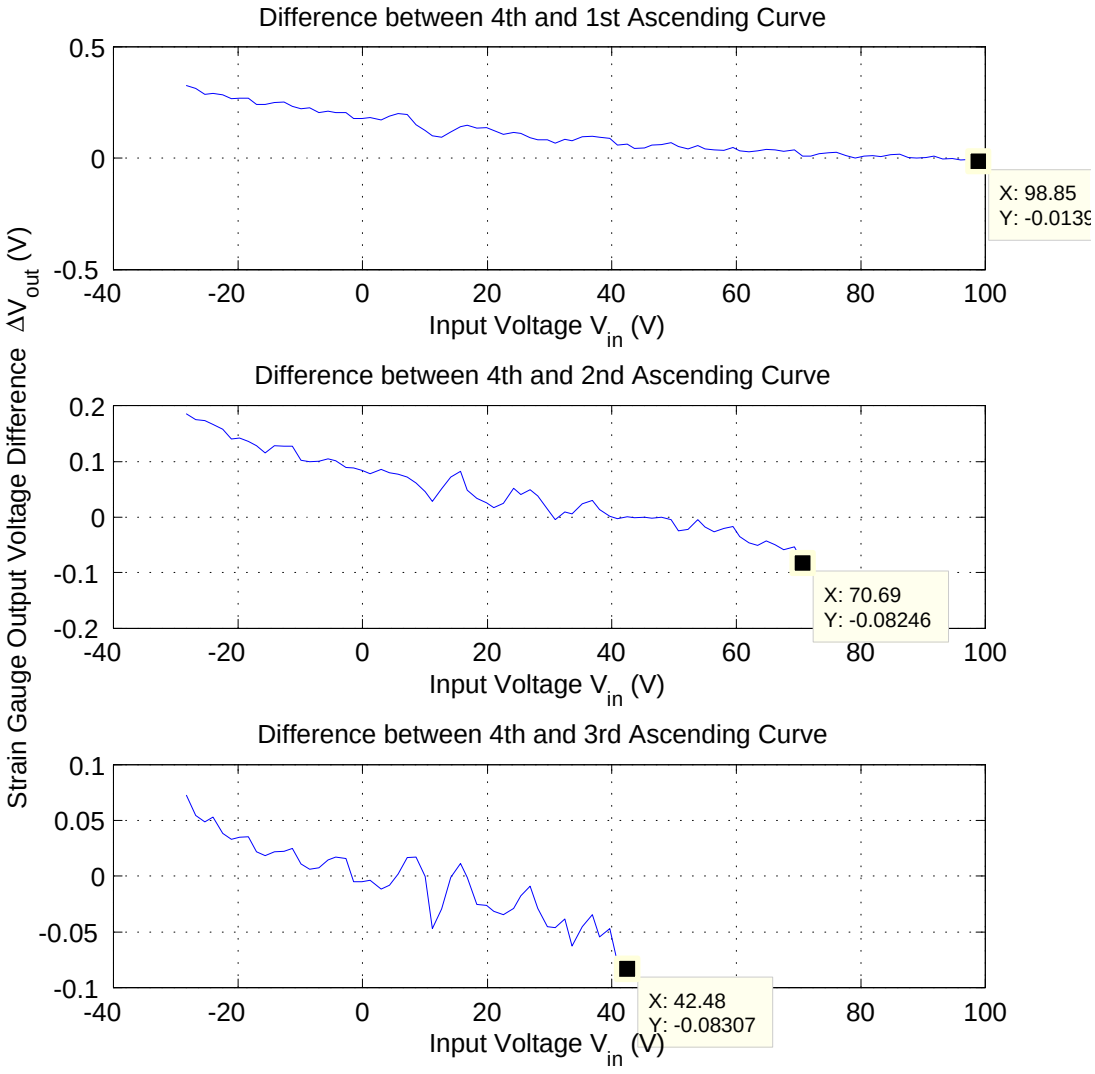

Figure 3.10: Output difference ΔV_{out} between ascending branches in the wiping-out test at $f = 1$ Hz.

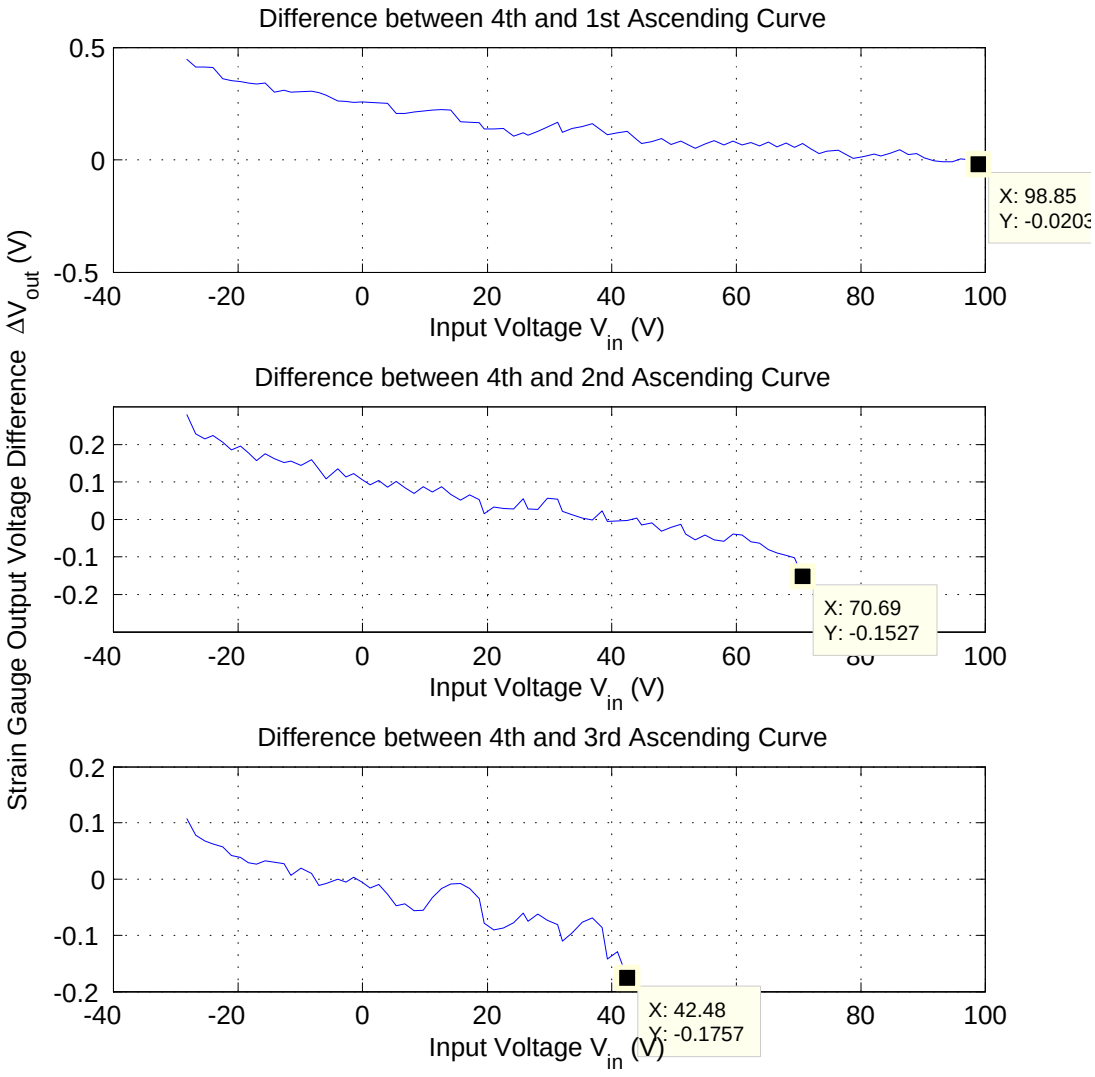

Figure 3.11: Output difference ΔV_{out} between ascending branches in wiping-out test $f = 2$ Hz.

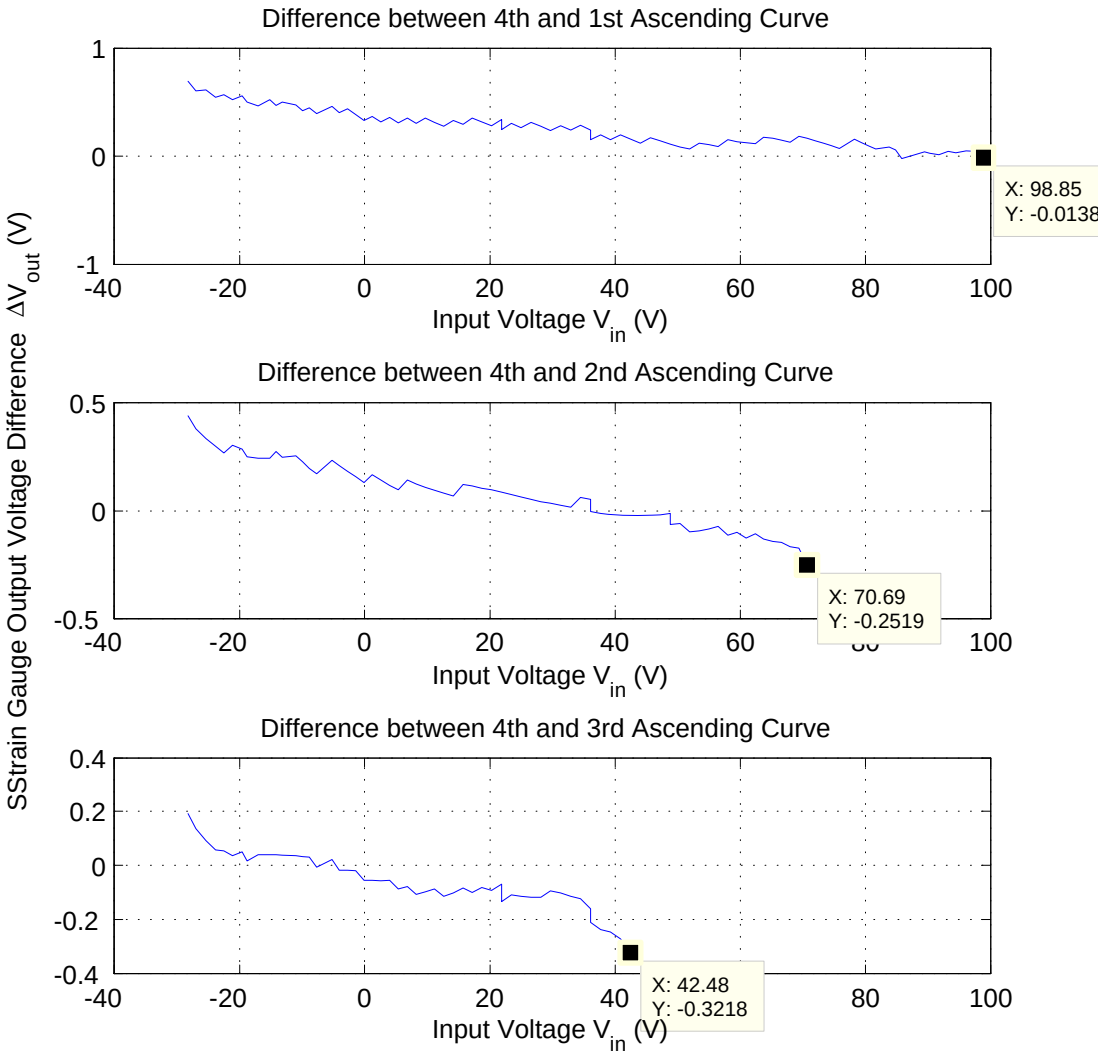

Figure 3.12: Output difference ΔV_{out} between ascending branches in wiping-out test $f = 4$ Hz.

loops should have the same shape. The first minor loop is generated by input segment A shown by a dashed line, while the second is generated by segment B shown as a dash-dotted line. The peak at $t = 12 + 1.5T$ s shifts the second minor loop upwards. The measurement of the output voltage V_{out} is shown from Figure 3.13 (b) through (d) corresponding to the input voltage at $f = 1$, 2 and 4 Hz respectively. The CML test results are shown on the input/output plane (I/O plane) from Figure 3.14 to Figure 3.16. Each graph is drawn with a solid line, dashed line and dash-dotted line, which correspond to the major loop, the first minor loop and the second minor loop. Moreover, the magnified parts of the first and second minor loops are shown in part (b) of Figure 3.14 through Figure 3.16. The second minor loops are shifted along the output axis of the I/O plane and rotated along the origin such that it can be compared to the first minor loop on the I/O plane directly. Even though the loops are not exactly congruent, their general shapes are similar, and therefore the CML property is satisfied.

Based on the experimental results of the wiping-out and congruent minor loop tests, the classical Preisach model can be used to characterize the hysteresis loop inherent in piezoceramic actuators with reasonable modelling error provided the input frequency is below 4 Hz.

3.3 Preisach Model Identification

A Preisach model is constructed for one Flexmorph in the SS15 by following the modelling identification process described in [53]. Generally speaking, the first order descending curve (FOD) data are collected for the whole restricted Preisach plane to form the surface $y(\alpha, \beta)$ which should be smooth based on an assumption of continuity for the system being modelled [53]. Then a smooth surface $\tilde{y}(\alpha, \beta)$ is fit to those FOD data points and the smooth surface $\tilde{y}(\alpha, \beta)$ is differentiated to obtain an approximate weighting surface $\tilde{\mu}(\alpha, \beta)$ according to Eq. (2.12), (2.13) and (2.14).

The experimental identification data are provided in subsection 3.4.1 for input signals with different frequencies, i.e. $f = 1$, 2, and 4 Hz. Surfaces $\tilde{y}^1(\alpha, \beta)$ $\tilde{y}^2(\alpha, \beta)$ and $\tilde{y}^4(\alpha, \beta)$ are obtained to fit the identified data generated from the different input signals in subsection 3.4.2. Then, those surfaces are respectively differentiated to generate the weighting functions $\tilde{\mu}^1(\alpha, \beta)$ $\tilde{\mu}^2(\alpha, \beta)$ and $\tilde{\mu}^4(\alpha, \beta)$. Simulation results of the identified model are subsequently provided to show that the model can capture the fundamental characteristics of the wiping-out test and the congruent minor loop test.

3.3.1 Model Identification Data Collection

This subsection presents the FOD data collected in experiments in order to determine the Preisach weighting surfaces that are subsequently used and detailed in the next two subsections.

As mentioned in Section 3.1, the circular platform is released from the four Flexmorphs in order to focus on the hysteresis behaviour generated by the piezoceramic actuator itself without the interference from additional mechanical parts. The range of the input voltage applied to SA11 controlled by DACs, i.e. the range of Vb_{in}, is approximately reduced to ± 7 V in order to reduce the strain gauge output voltage of the four connected ADCs within the reading range of ± 5 V. Then the high input voltage V_{in} applied to SS15 is divided into 20 equal sections, i.e.

$$\{V_{in}\} = \{-100 + 10 * i : i = 0, 1, \cdots, 20\}$$

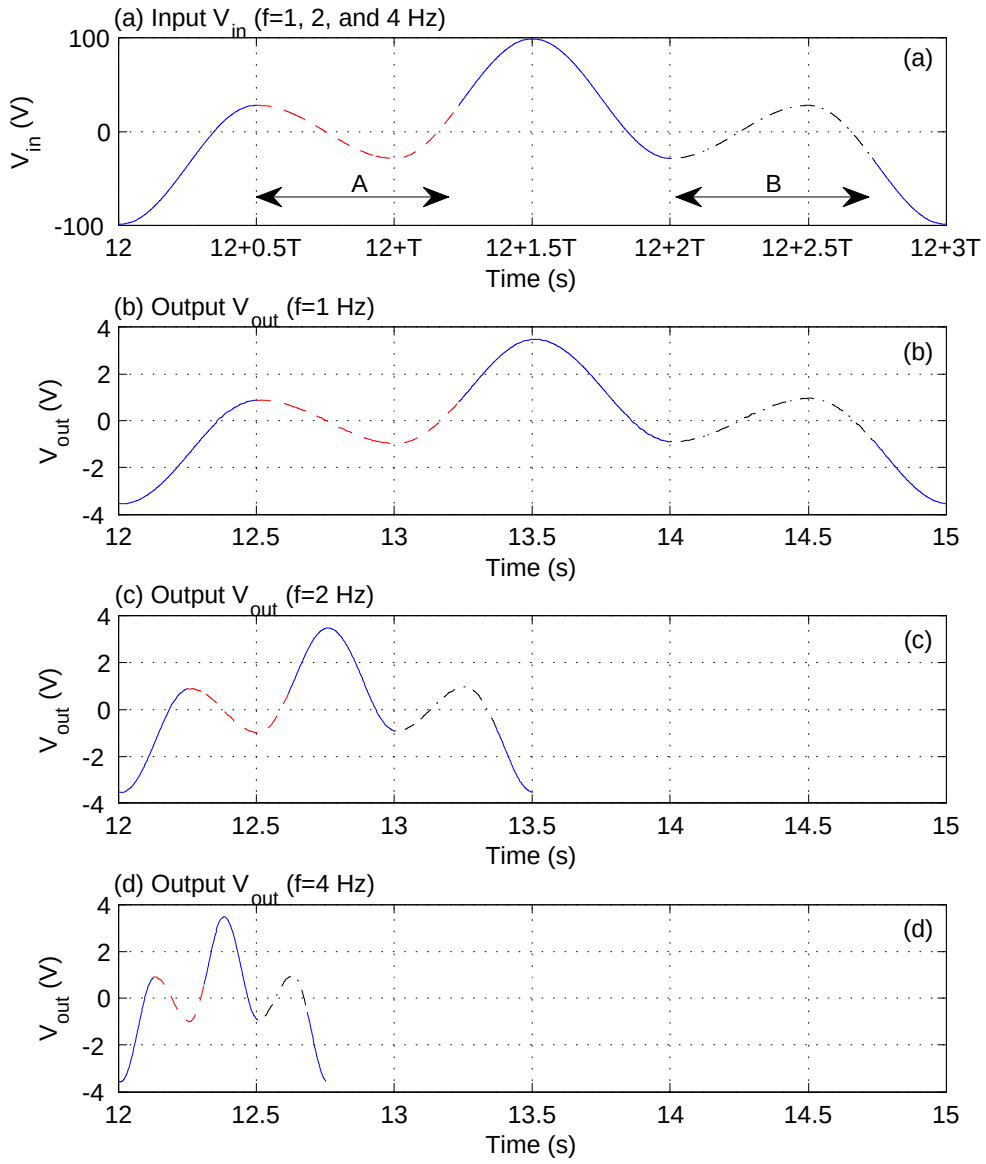

Figure 3.13: Input voltage V_{in} and strain gauge output voltage V_{out} w.r.t time t in CML test with different frequencies.

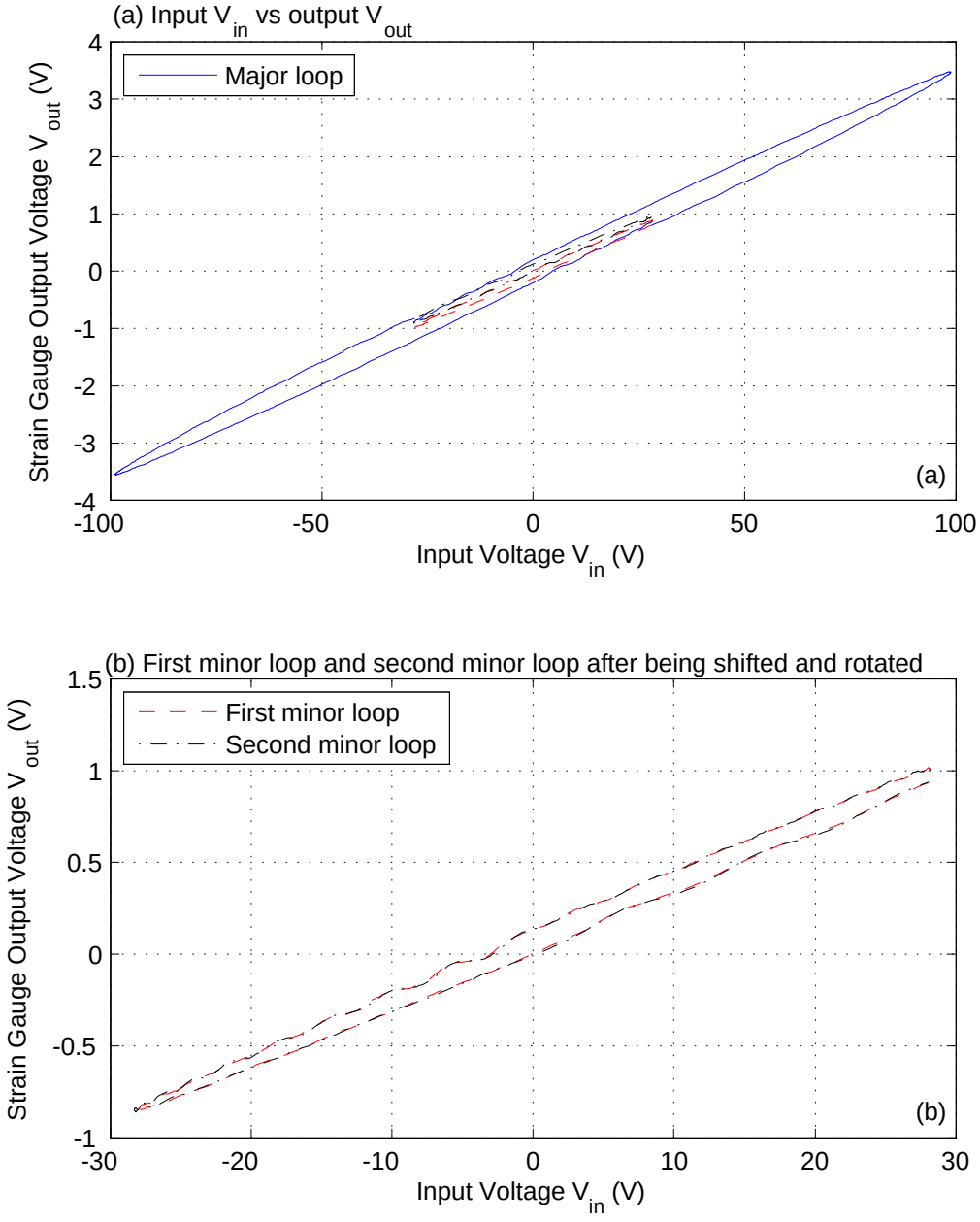

Figure 3.14: CML test results $f = 1$ Hz.

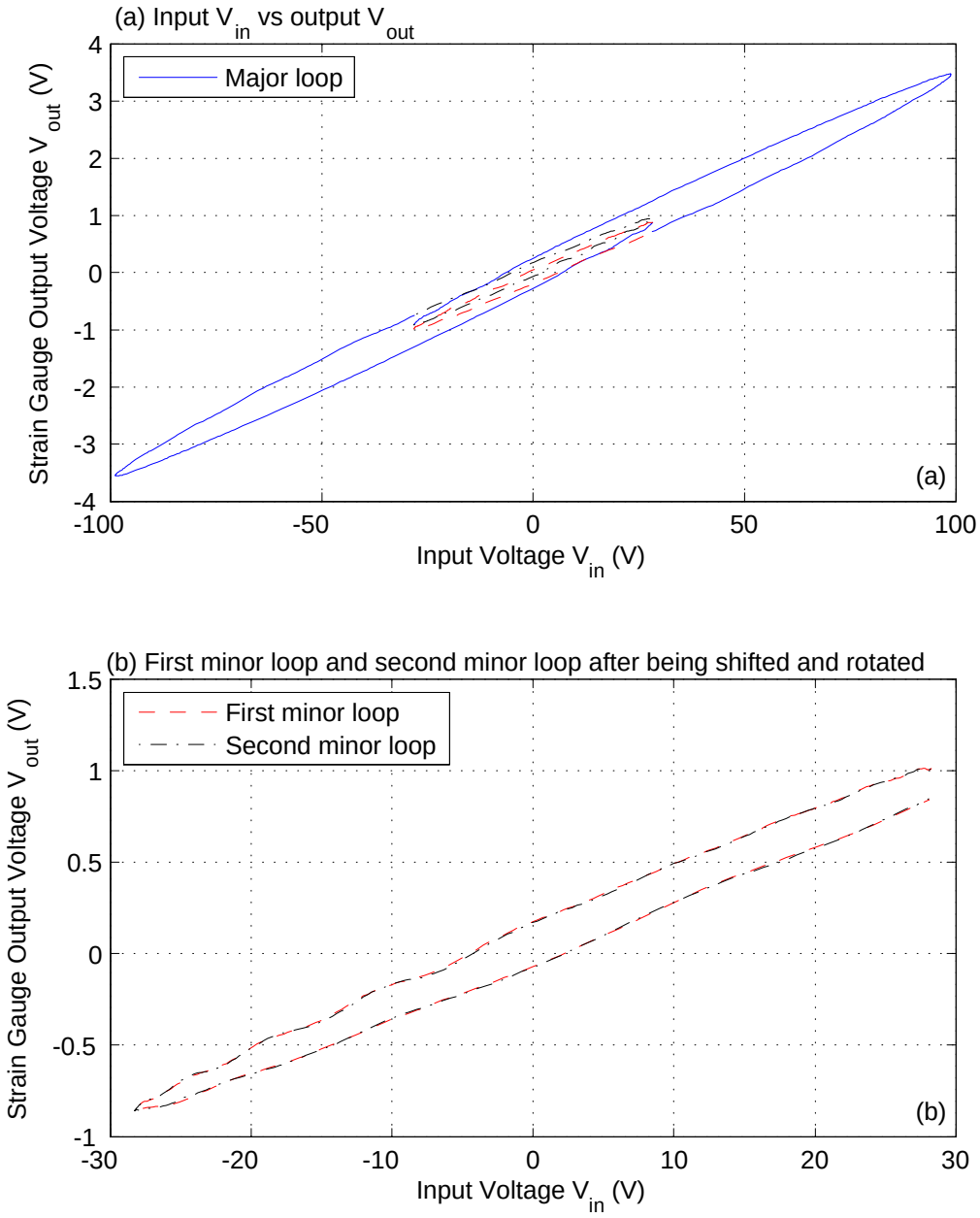

Figure 3.15: CML test results $f = 2$ Hz.

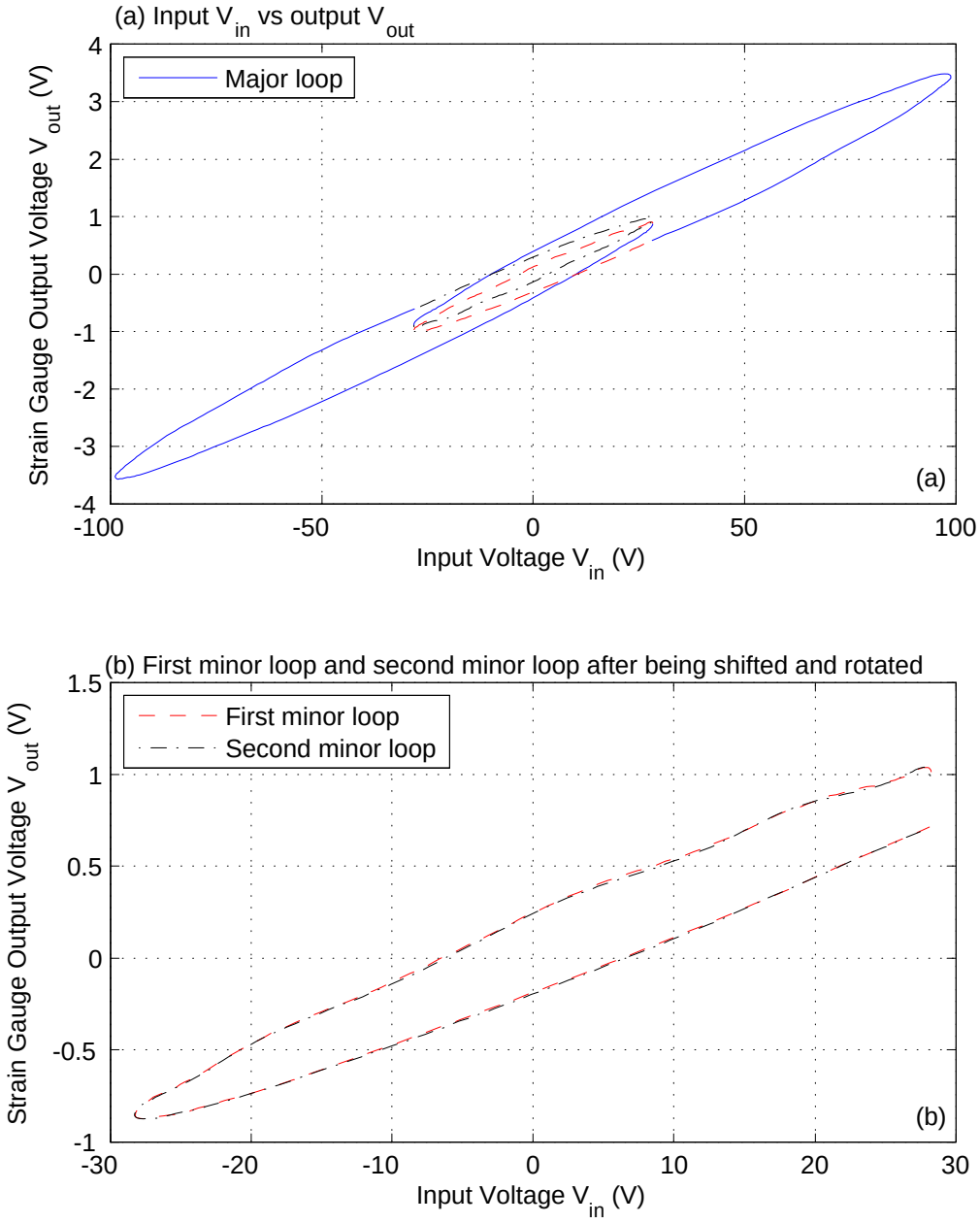

Figure 3.16: CML test results $f = 4$ Hz.

The input voltage signals V_{in} with frequencies $f = 1$, 2, and 4 Hz are shown in Figure 3.17 which generated the twenty FOD curves for each input signal. T in the x-axis of Figure 3.17 presents the period of the input signal and is equal to $1/f$, thus the 3 different frequencies are included in the figure by $T = 1$, 0.5, and 0.25 s for $f = 1$, 2, and 4 Hz respectively. The circle points represent the corresponding input of the FOD data points. In Figure 3.17 the FOD data points shown with asterisks is an example curve of the twenty FOD curves to be fit. The corresponding measured output of those 21 asterisks data points can be denoted by y_{α_1} and $y_{\alpha_1\beta_i}$ ($i = 1$, 2, ... 20), where $\alpha_1 = 100$ and $\beta_i = 100 - 10i$, also shown as asterisks on the I/O plane from Figure 3.18 through Figure 3.20.

The measured outputs of those FOD curves are shown from Figure 3.18 through Figure 3.20, in each of which the FOD data points are joined by dashed line segments to show the general shape of the hysteresis generated by the input signals with frequencies $f = 1$, 2, and 4 Hz correspondingly. Even though it is not evident from the figure directly, the FOD curves indeed do not intersect within the major loop. This can, however, be observed when the figure is magnified. A magnified section of each figure is also shown from Figure 3.18 through Figure 3.20 when the input voltage V_{in} is around 40 V. Moreover, the actuator is not fully exercised since the width of the hysteresis loop is quite narrow and no output saturation appears. Figure 3.21 through Figure 3.23 illustrate the FOD data in three dimensions generated by input voltage signals with frequencies $f = 1$, 2, and 4 Hz respectively. Surfaces $\tilde{y}^1(\alpha,\beta)$ $\tilde{y}^2(\alpha,\beta)$ and $\tilde{y}^4(\alpha,\beta)$ are generated to fit those FOD data points and the weighting functions $\tilde{\mu}^1(\alpha,\beta)$ $\tilde{\mu}^2(\alpha,\beta)$ and $\tilde{\mu}^4(\alpha,\beta)$ of the hysteresis behaviour are obtained by numerically differentiating the surfaces $\tilde{y}^1(\alpha,\beta)$ $\tilde{y}^2(\alpha,\beta)$ and $\tilde{y}^4(\alpha,\beta)$ respectively.

3.3.2 FOD Surface Fit

In [45], a third-order, two-dimensional surface is fit to the FOD surface of a piezoceramic actuator. The approach to surface fitting applied in this thesis is modelled after that used in [47] because of its high degree of applicability to the system studied in the present work. From the experimental data with input voltage signals at frequencies $f = 1$, 2, and 4 Hz, it is observed that the curvature of the FOD curves is similar to that of the square root function for each input voltage signal. Thus, curve fitting is implemented first on each FOD curve by a least-square fit of the function

$$\tilde{y}^i_\alpha(\beta) = X^i_1(\alpha) + X^i_2(\alpha)\sqrt{\beta - X^i_3(\alpha)} \qquad i = 1, 2, 4$$

for each constant α. Polynomial curves are avoided because they can increase model order and introduce oscillations which will cause problems when differentiated. Then, the parameters X^i_1, X^i_2, and X^i_3 are examined as a function of α in order to determine a candidate surface to fit the FOD surface finally. In the following, the superscript $i = 1$, 2, and 4 indicates the corresponding function or variable based on the FOD data sets generated by input voltage signals with frequencies $f = 1$, 2, and 4 Hz respectively, and are named by Case 1, 2 and 3.

The least-square fit is applied in the data fitting by using the $fminsearch$ command in Matlab which is based on a Nelder-Mead simplex algorithm [54]. The results are shown from Figure 3.24 through Figure 3.26. Since three parameters are used to determine the curve function for each FOD data set, only those FOD curves that contain more that three data points were fit and the resulting parameters X^i_1, X^i_2, and X^i_3 are parameterized as a function of α in order to perform the surface fitting. Comparing to the result shown in [45], the FOD curves have very similar shapes

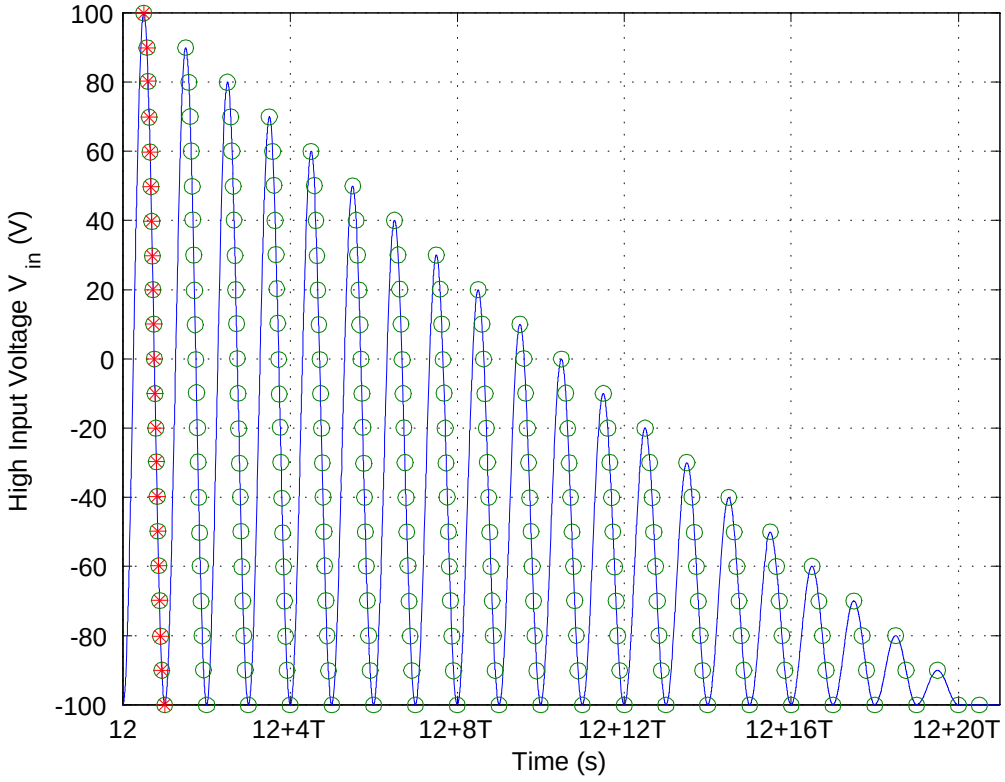

Figure 3.17: Identification input with frequencies $f = 1$, 2, 4 Hz and $T = 1/f$.

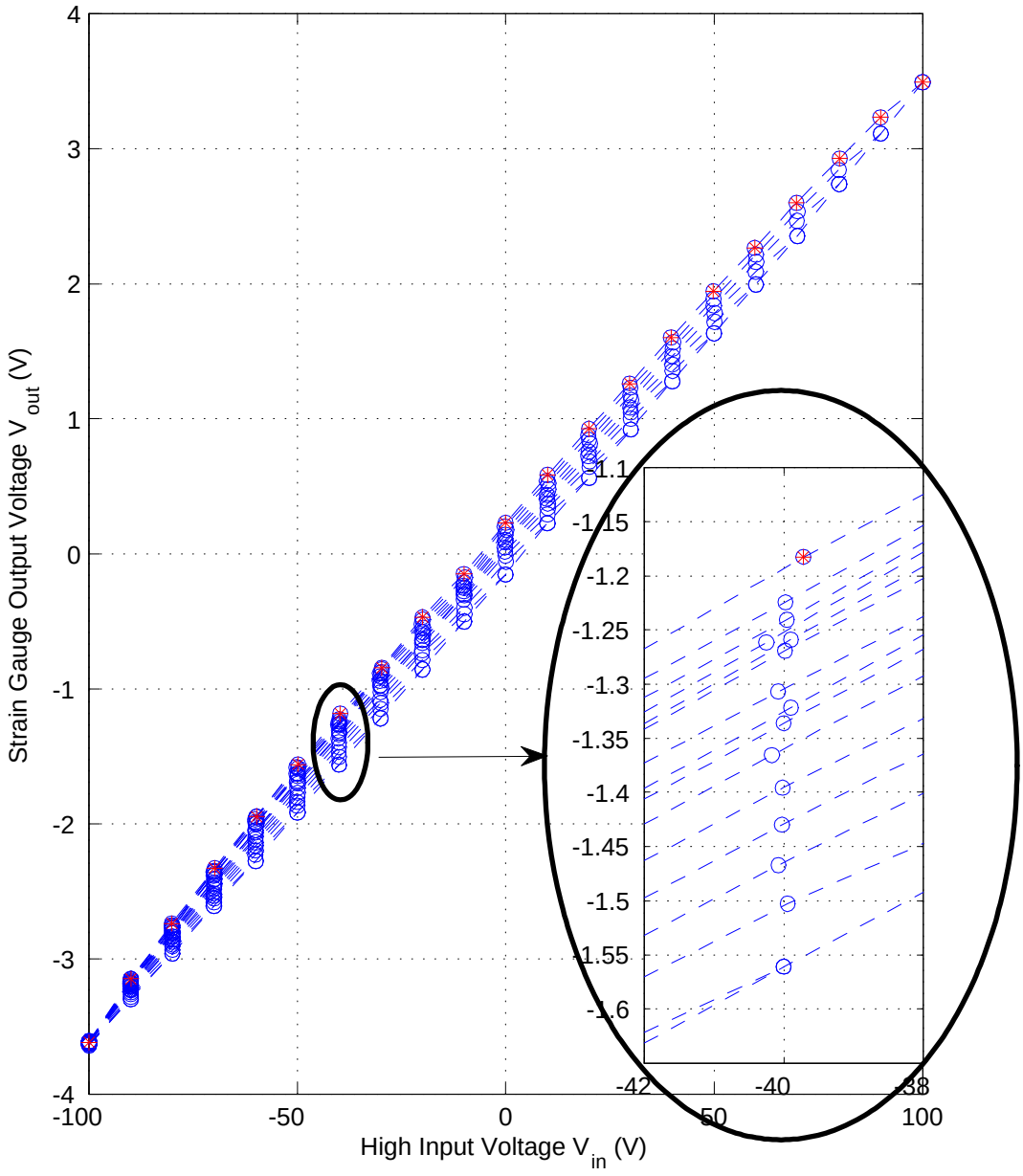

Figure 3.18: Measured FOD data ($f = 1$ Hz).

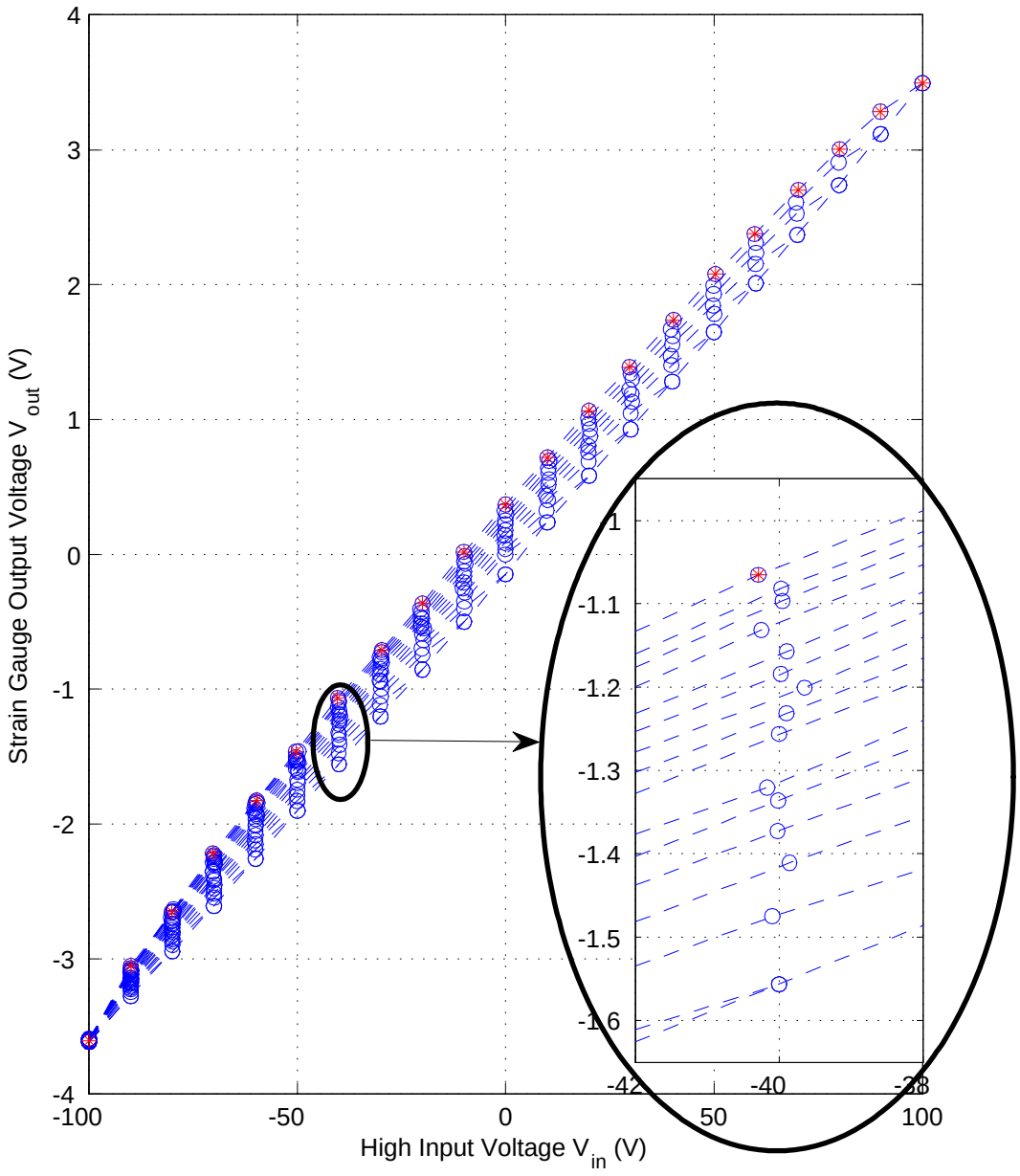

Figure 3.19: Measured FOD data ($f = 2$ Hz).

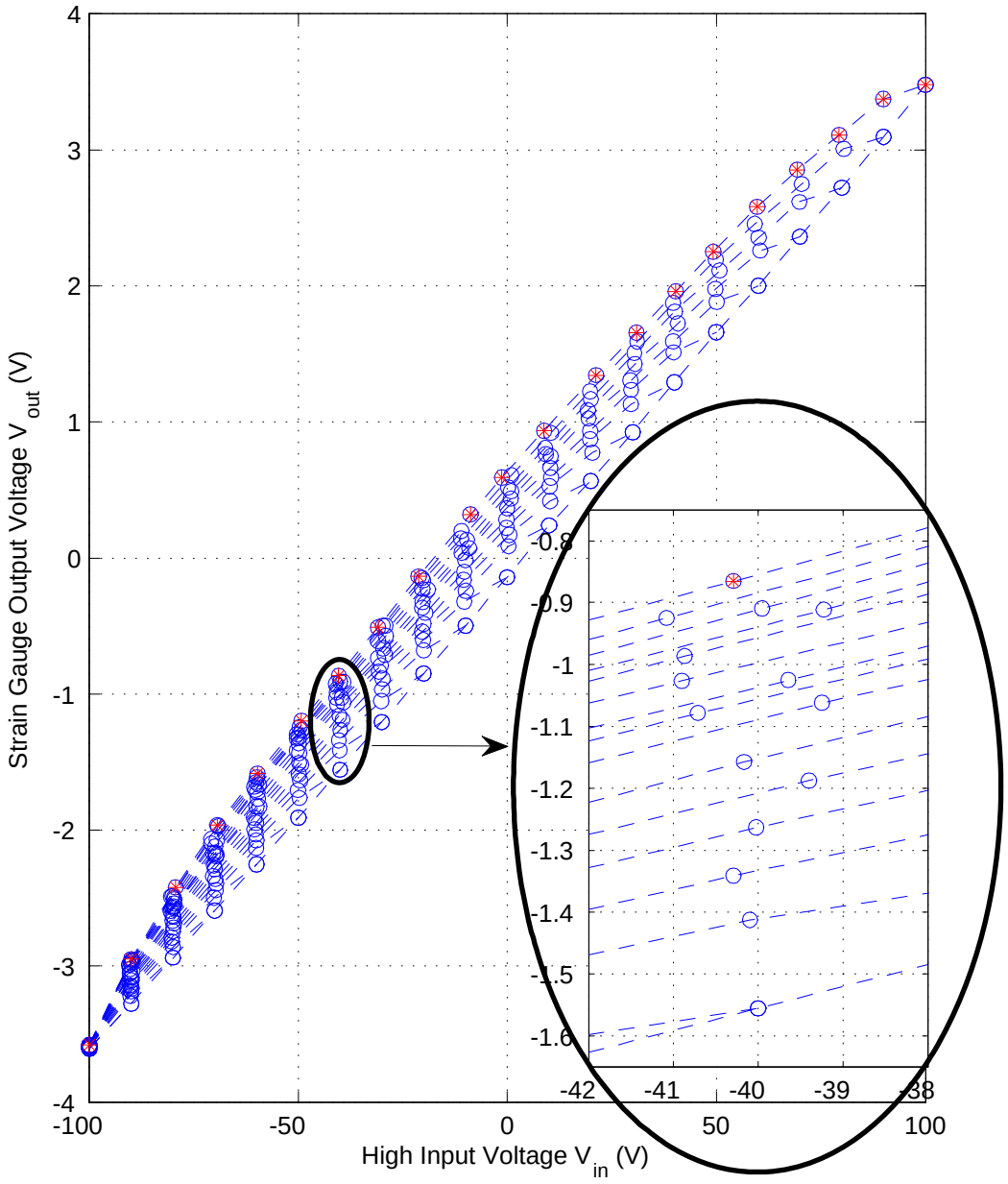

Figure 3.20: Measured FOD data ($f = 4$ Hz).

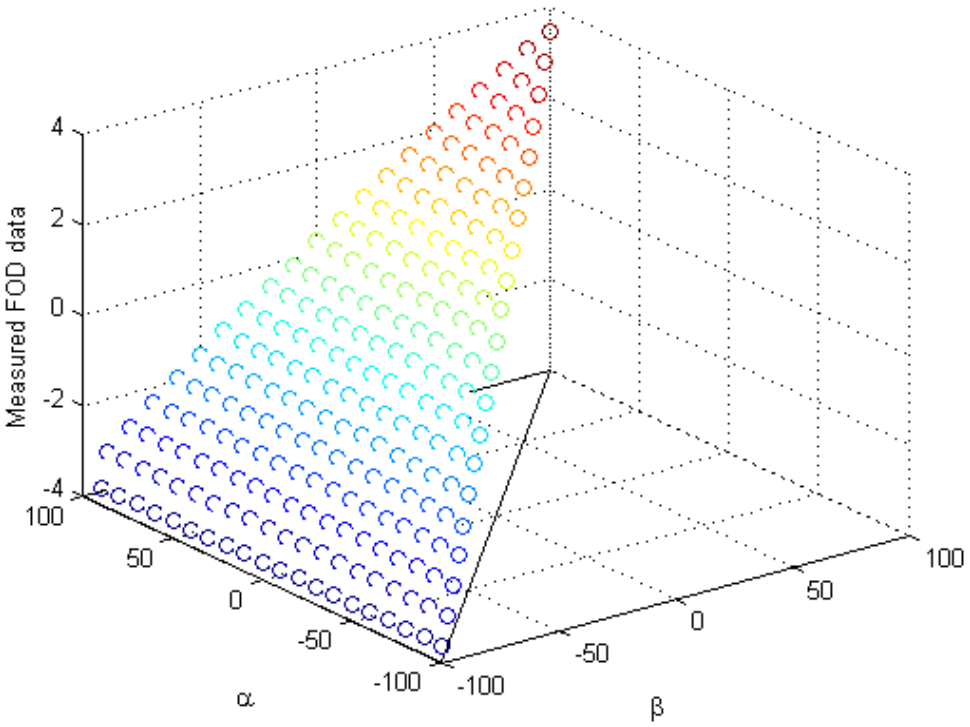

Figure 3.21: FOD fit data in three dimensions ($f = 1$ Hz).

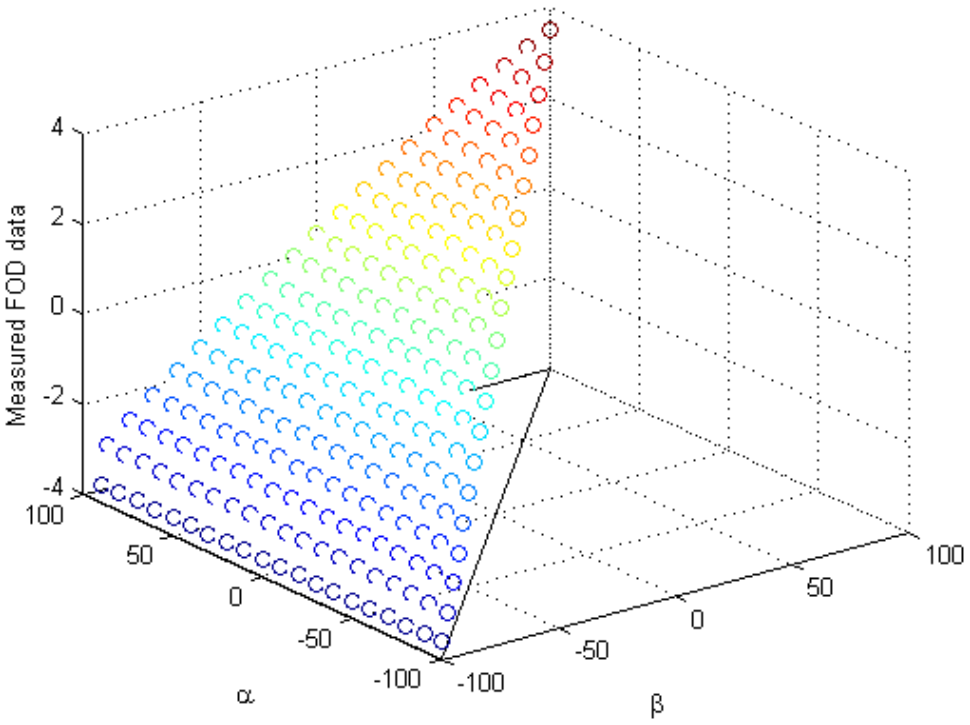

Figure 3.22: FOD fit data in three dimensions ($f = 2$ Hz).

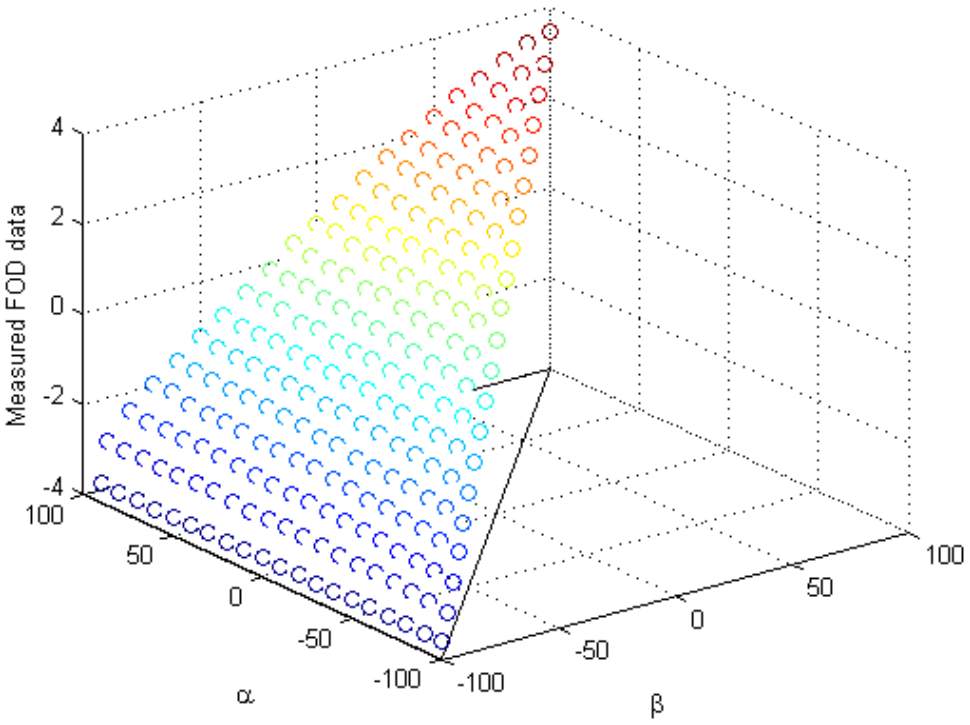

Figure 3.23: FOD fit data in three dimensions ($f = 4$ Hz).

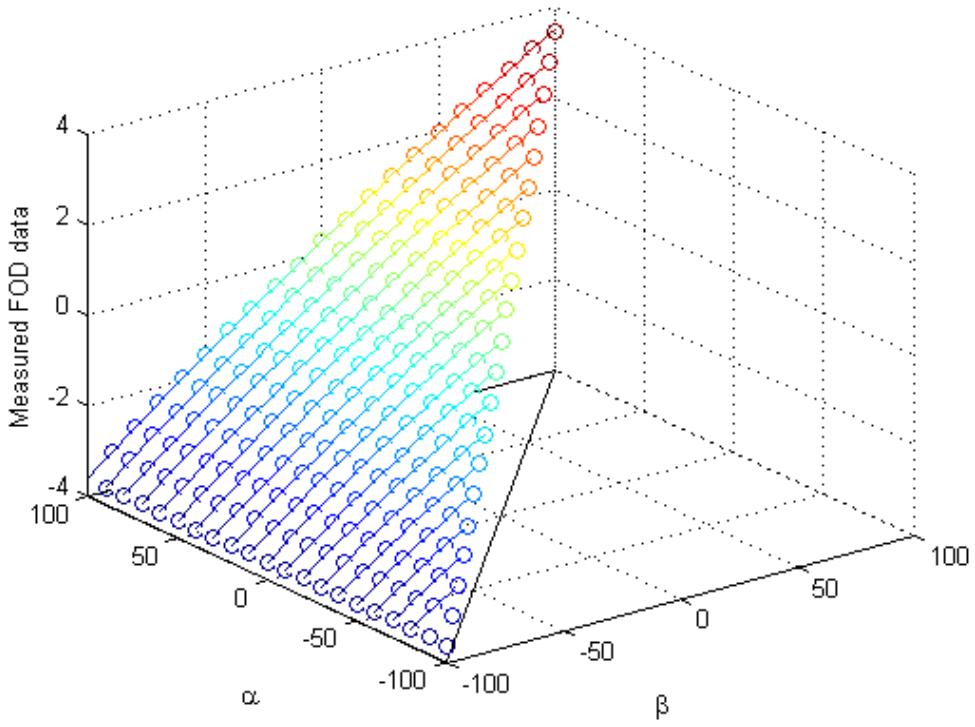

Figure 3.24: FOD curve fit ($f = 1$ Hz).

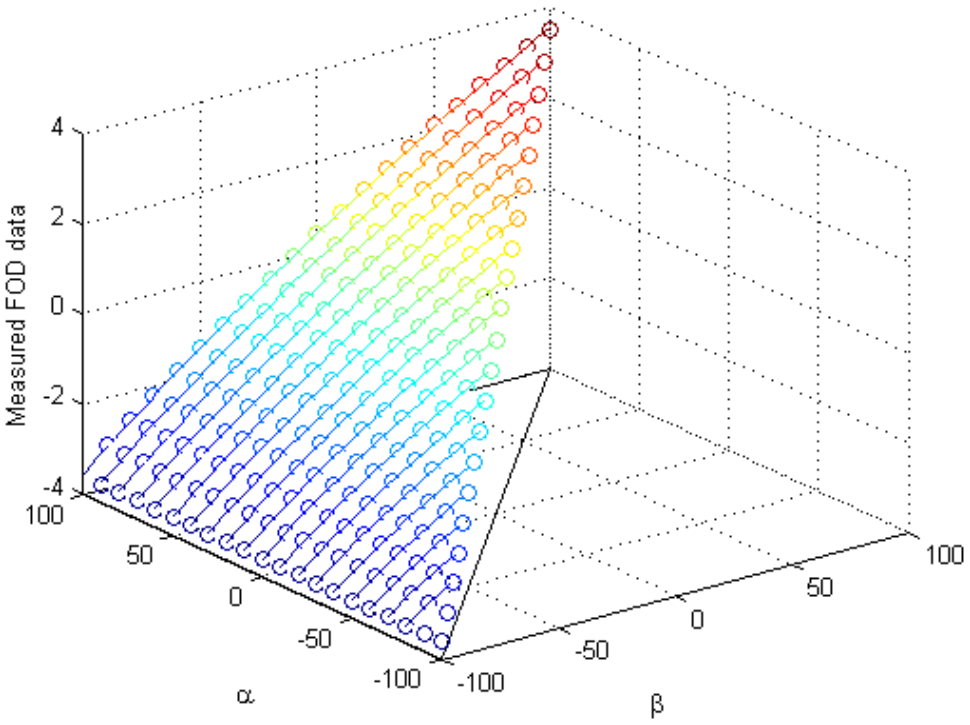

Figure 3.25: FOD curve fit ($f = 2$ Hz).

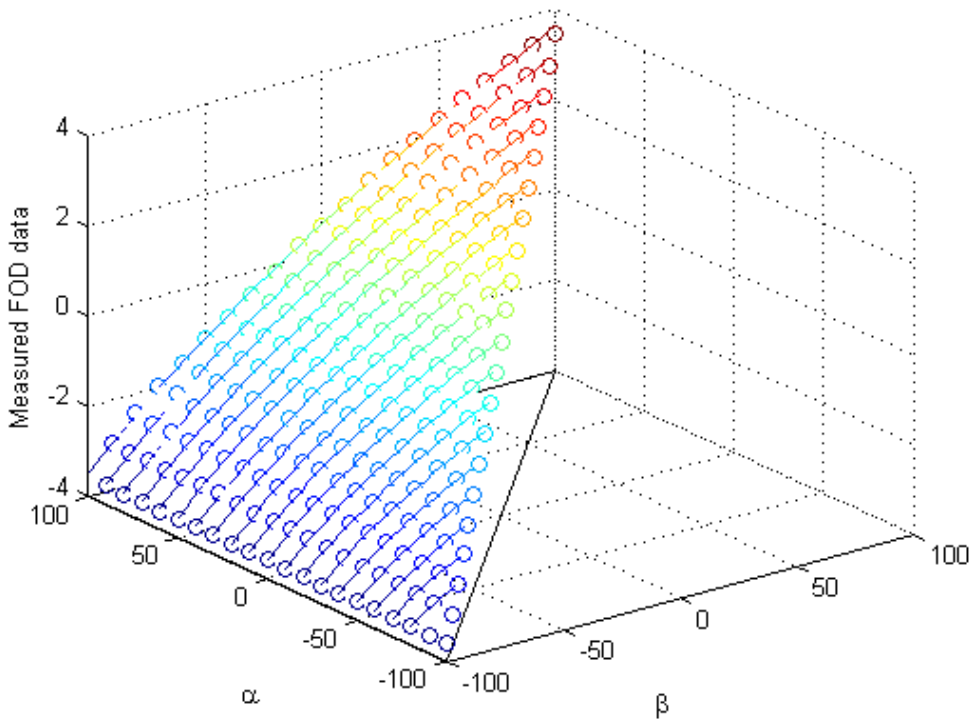

Figure 3.26: FOD curve fit ($f = 4$ Hz).

especially when the input voltages have lower frequency since the FOD data collected in [45] is generated by "low rate of change command trajectories".

Initially the candidate surface is denoted by $\tilde{y}_i'$ where $i = 1,\ 2,\ 4$ and indicates that the candidate surface is for the FOD data set generated by the input voltage signal with frequencies $f = 1$, 2, and 4 Hz respectively. $\tilde{y}_i'$ is defined by the following equation:

$$\tilde{y}_i'(\alpha,\beta) = \tilde{y}_\alpha^i(\beta) = X_1^i(\alpha) + X_2^i(\alpha)\sqrt{\beta - X_3^i(\alpha)}$$

The parameters X_1^i to X_3^i are shown from Figure 3.27 through Figure 3.29 as functions of α for Case 1, 2 and 3 respectively, which are all fit by second order polynomials in order to keep the order of the model low and fit the data curvature appropriately at the same time. The Matlab command *polyfit* is used to implement the data fitting in a least-square sense. The parameters are defined as follows:

$$\begin{aligned} X_1^i(\alpha) &= f_1^i(\alpha) = x_1^i\alpha^2 + x_2^i\alpha + x_3^i \\ X_2^i(\alpha) &= f_2^i(\alpha) = x_4^i\alpha^2 + x_5^i\alpha + x_6^i \\ X_3^i(\alpha) &= f_3^i(\alpha) = x_7^i\alpha^2 + x_8^i\alpha + x_9^i \end{aligned}$$

In order to match the output when the input is at the saturation point, the candidate surface needs to be modified for a perfect match.

Now, $y^i(\hat{u},\hat{u})$ is defined as the maximum output when the input keeps increasing to the maximum identification input value $\hat{u}$. Similarly $y^i(\hat{u},-\hat{u})$ represents the minimum output when the input is increased to $\hat{u}$ first and then decreased to the minimum identification input value $-\hat{u}$. As shown in Figure 3.18 through Figure 3.20, all the FOD curves merge at $-\hat{u}$. Thus, $y^i(\hat{u},-\hat{u})$ should be reached on every FOD curve, i.e. $y^i(\alpha,-\hat{u}) = y^i(\hat{u},-\hat{u})$ for each α. $y^i(\hat{u},\hat{u})$ and $y^i(\hat{u},-\hat{u})$ were obtained in identification experiments.

In order to match the minimum output value, a zero offset term is added to the candidate surface and three parameters x_1^i x_2^i and x_3^i can be removed for parameter minimization in each case:

$$\begin{aligned} \tilde{y}^i(\alpha,\beta,f) &= \tilde{y}_i'(\alpha,\beta) - \tilde{y}_i'(\alpha,-\hat{u}) + y^i(\hat{u},-\hat{u}) \\ &= f_2^i(\alpha)\left(\sqrt{\beta - f_3^i(\alpha)} - \sqrt{-\hat{u} - f_3^i(\alpha)}\right) + y^i(\hat{u},-\hat{u}) \end{aligned} \tag{3.1}$$

On the other hand, one more parameter can be removed for parameter minimization in each case. In order to make $\tilde{y}^i(\hat{u},\hat{u})$ match the maximum output value $y^i(\hat{u},\hat{u})$, x_6^i can be isolated by substituting $\alpha = \beta = \hat{u}$ into Eq. (3.1), setting $\tilde{y}^i(\hat{u},\hat{u}) = y^i(\hat{u},\hat{u})$ and rearranging the equation. The function f_2^i is redefined as $\bar{f}_2^i$ as follows, which is not equal to zero in the input range of $[-100, 100]$ as observed from Figure 3.27 through Figure 3.29:

$$\bar{f}_2^i(\alpha) = \bar{x}_4^i\alpha^2 + \bar{x}_5^i\alpha + 1$$

where $\bar{x}_4^i = x_4^i/x_6^i$ and $\bar{x}_5^i = x_5^i/x_6^i$. It is observed that $\bar{f}_2^i(\hat{u}) \neq 0$ from Figure 3.27 through Figure 3.29. Thus, x_6^i is calculated based on $y^i(\hat{u},\hat{u})$, $y^i(\hat{u},-\hat{u})$, $\bar{f}_2^i(\hat{u})$, and $f_3^i(\hat{u})$ for the parameter minimization, as shown below:

$$x_6^i = \frac{y^i(\hat{u},\hat{u}) - y^i(\hat{u},-\hat{u})}{\bar{f}_2^i(\hat{u})\left(\sqrt{\hat{u} - f_3^i(\hat{u})} - \sqrt{-\hat{u} - f_3^i(\hat{u})}\right)}$$

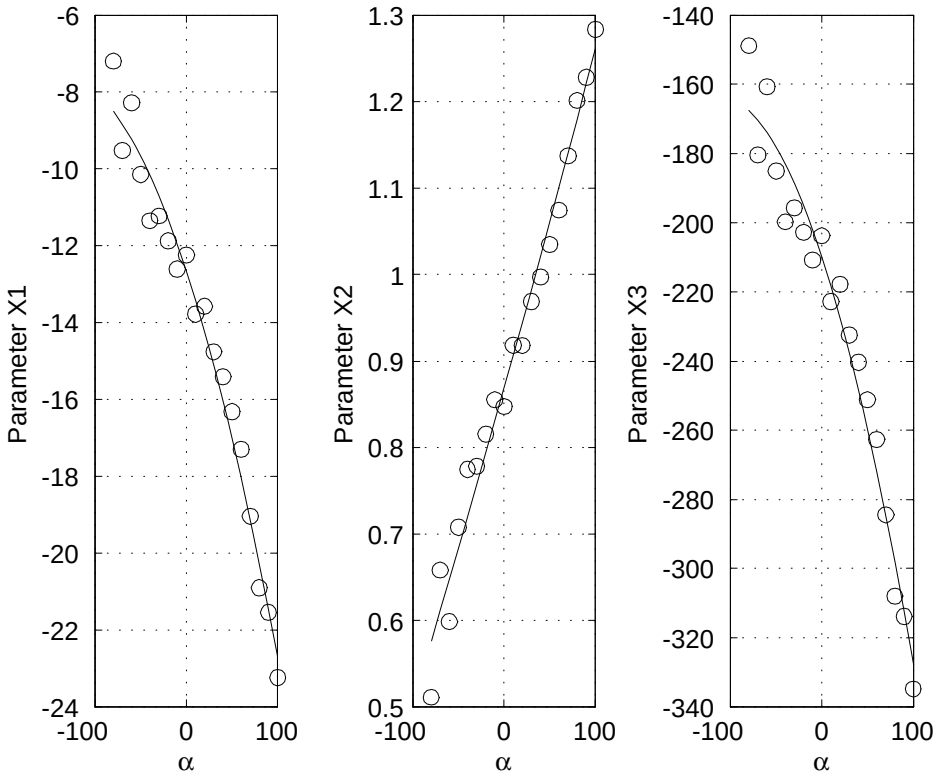

Figure 3.27: Parameters variation and fitting ($f = 1$ Hz).

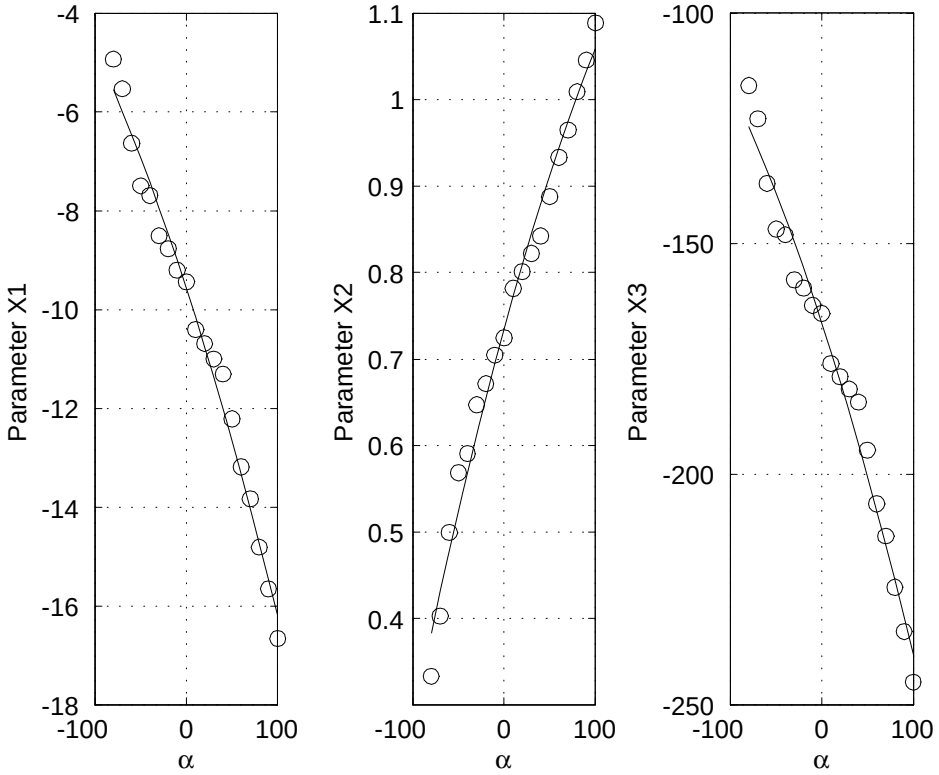

Figure 3.28: Parameters variation and fitting ($f = 2$ Hz).

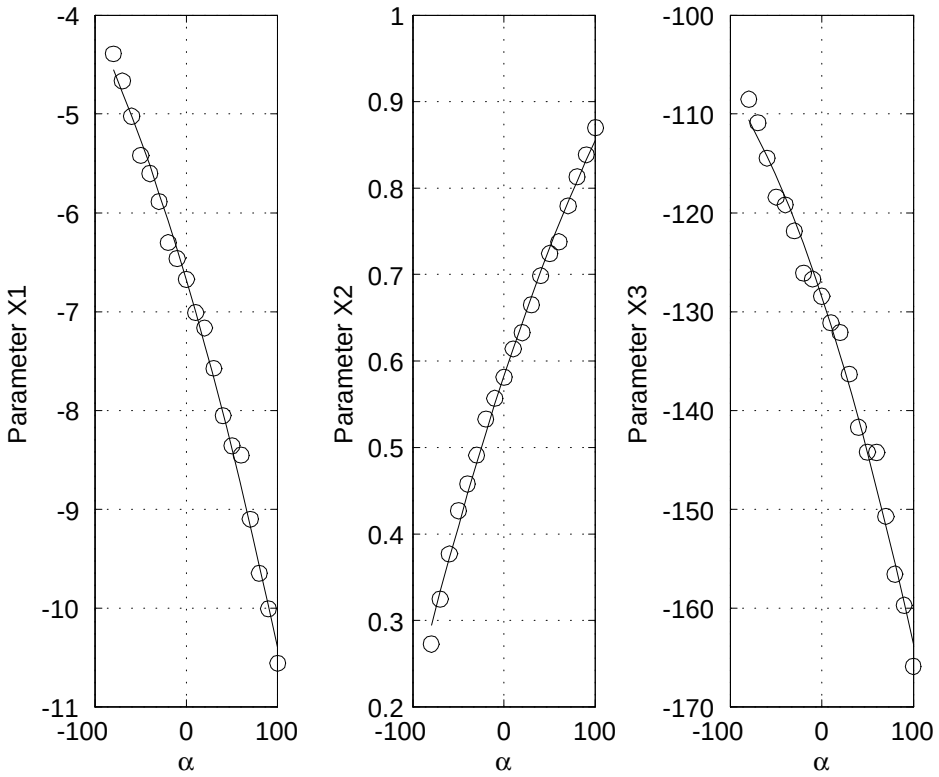

Figure 3.29: Parameters variation and fitting ($f = 4$ Hz).

The modified form of the candidate surface is

$$\tilde{y}^i(\alpha,\beta,f) = \left(y^i(\hat{u},\hat{u}) - y^i(\hat{u},-\hat{u})\right)\frac{\left(\bar{x}_4^i\alpha^2+\bar{x}_5^i\alpha+1\right)\left(\sqrt{\beta-f_3^i(\alpha)}-\sqrt{-\hat{u}-f_3^i(\alpha)}\right)}{\left(\bar{x}_4^i\hat{u}^2+\bar{x}_5^i\hat{u}+1\right)\left(\sqrt{\hat{u}-f_3^i(\hat{u})}-\sqrt{-\hat{u}-f_3^i(\hat{u})}\right)} + y^i(\hat{u},-\hat{u}) \tag{3.2}$$

It is straight forward to show that $\tilde{y}^i(\hat{u},\hat{u}) = y^i(\hat{u},\hat{u})$ and $\tilde{y}^i(\alpha,-\hat{u}) = y^i(\hat{u},-\hat{u})$.

Table 3.1: FOD surface fit data

f (Hz)	1	2	4
$\bar{x}_4$	8.81e-06	2.24e-06	-5.28e-06
$\bar{x}_5$	3.47e-03	3.99e-03	4.39e-03
x_7	-4.16e-03	-1.73e-03	-3.41e-04
x_8	-4.83e-01	-3.19e-01	-1.33e-01
x_9	-1.94e+02	-1.55e+02	-1.24e+02
$u_{\max}$	100.00		
$u_{\min}$	-100.00		
$y_{\max}$	3.49	3.49	3.48
$y_{\min}$	-3.63	-3.62	-3.60
error	0.38	0.57	1.10

The results of surface fitting based on this least-squares technique are shown in Figure 3.30 through 3.32 and Figure 3.33 through 3.35 based on the different FOD data sets and the different elementary hysteresis block notation $\gamma_{\alpha,\beta}$ and $\gamma_{r,s}$ respectively. The FOD data measurement from experiments is also shown in those six figures. The surface matches the experimental data exactly at the minimum saturation input. All the parameters of the surface are listed in Table 3.1 together with the square root of the least-squares error over all the FOD data points for three cases. The average error at each sampled data point is only 0.0016, 0.0025, and 0.0047 V and within 0.07% of the whole output measurement range for each case. This is indicative that the matching result is quite good.

An interesting aspect of the current research is that data sets have been collected and surfaces fit for multiple input frequencies. Thus, these data sets suggest that the parameters of the surfaces listed in Table 3.1 could be re-parameterized as functions of frequency. In this way, the effective expanding of these static data sets could be used to generate a dynamic model for the frequency-dependent piezo system with hysteresis. Although the current data sets only cover three input frequencies and would not be sufficient to generate a meaningful result, future work could augment these data sets so that a weighting surface μ could be fit as a function of frequency and retain a high degree of fidelity over a broad range of frequencies.

3.3.3 Weighting Surface

Differentiating the fitted FOD surface results in the weighting functions. For each FOD data set, the weighting functions are illustrated by two parts as shown in Figure 3.36 and Figure 3.37 based

on the notation of the basic hysteresis block $\gamma_{\alpha,\beta}$ when the input voltage signal is at $f = 1$ Hz. The results of the other two cases are shown from Figure 3.38 through Figure 3.41. There are two parts of the weighting function: a new two-dimensional surface $v(\alpha, \beta)$ and a one-dimensional curve $\kappa(\alpha)$ along the diagonal line ($\alpha = \beta$).

By using $\gamma_{r,s}$ as the notation of the elementary hysteresis block, the corresponding two-dimensional surface of the weighting $v(r, s)$ is shown from Figure 3.42 through 3.44 for all the three cases. The corresponding one-dimensional curve $\kappa(s)$ along the vertical axis ($r = 0$) has the exact same shape as the curve $\kappa(\alpha)$ shown from Figure 3.37 through 3.41 for all the three cases since $s = \frac{\alpha+\beta}{2} = \alpha$ when $\alpha = \beta$.

Figure 3.36 and Figure 3.37 show that the weighting function $\mu(\alpha, \beta)$ is bounded and piecewise continuous as expected from the form of FOD surfaces $\tilde{y}^i(\alpha, \beta)$. $\mu(\alpha, \beta)$ is also non-negative when the input voltage signal is at 1 Hz. Thus, $\mu(\alpha, \beta) \in M_p$ when $f = 1$ Hz. Moreover, when the input signal is at 2 and 4 Hz, the weighting function $\mu(\alpha, \beta)$ is bounded and piecewise continuous as shown in Figure 3.38 through Figure 3.41. However, with careful observation, it is found that the negative part of the weighting function $\mu(\alpha, \beta)$ is very small. When the input signal is at 2 Hz, the negative values appear at four points which are $(100, -100)$, $(94.87, -100)$, $(89.74, -100)$ and $(84.62, -100)$ and the minimum value is -1.177×10^{-6} at the point $(94.87, -100)$. In particular, when the input signal is at $f = 4$ Hz, a negative value appears at only one point which is $(100, -100)$ and the value is -1.451×10^{-6}. From a physical point of view, the negative value of the weighting function should not exist for the hysteresis of piezoceramic actuators. This could be caused by forcing all the FOD curves to merge at $-\hat{u}$ or the effect of measurement noise in the FOD data. Considering that the area and the magnitude of the weighting function $\mu(\alpha, \beta) < 0$ is relatively small, $\mu(\alpha, \beta)$ is considered to belong to M_p for all input frequencies tested.

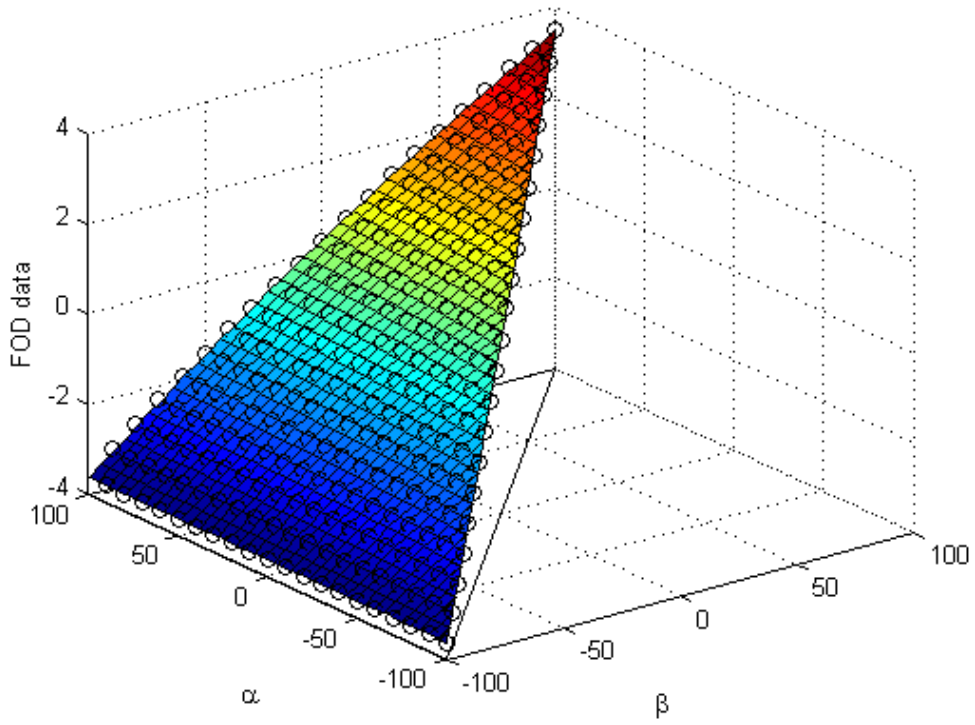

Figure 3.30: FOD surface fit based on $\gamma_{\alpha,\beta}$ as the basic hysteresis block ($f = 1$ Hz).

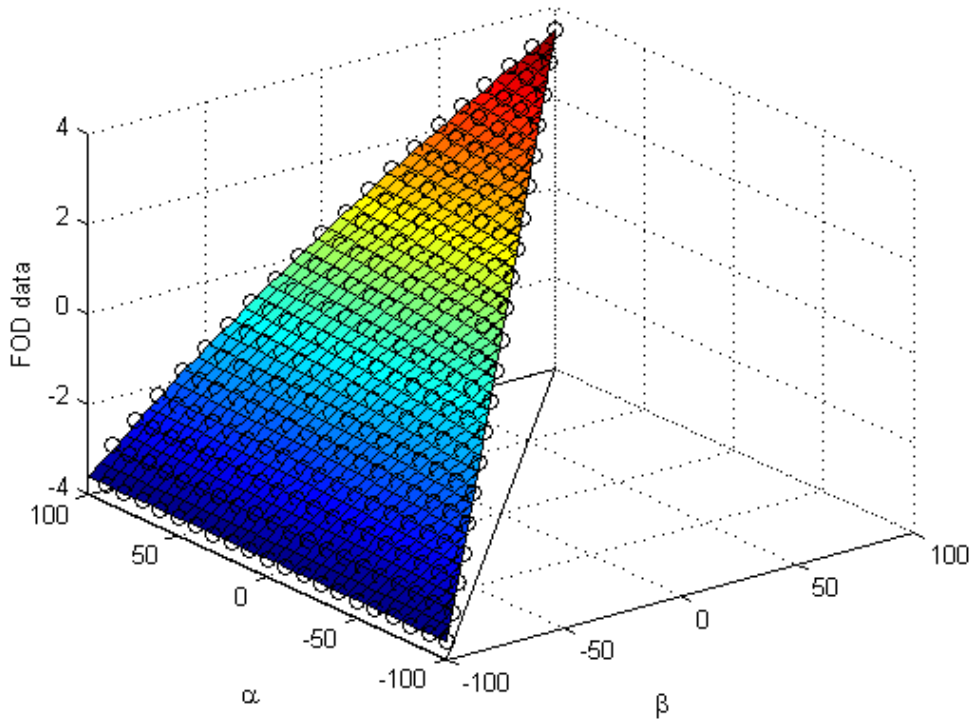

Figure 3.31: FOD surface fit based on $\gamma_{\alpha,\beta}$ as the basic hysteresis block ($f = 2$ Hz).

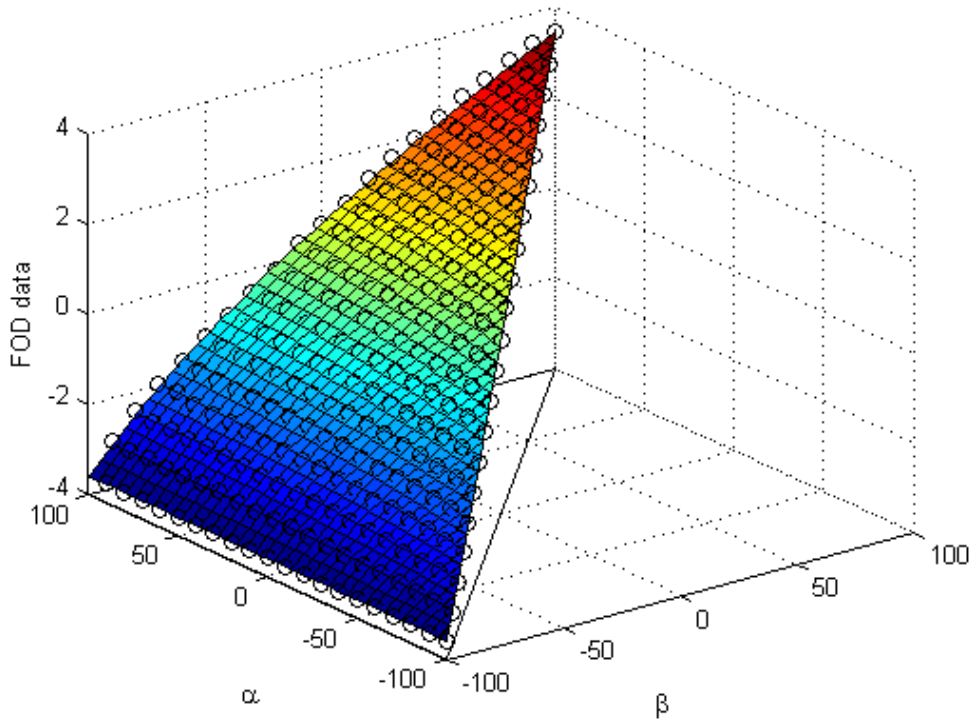

Figure 3.32: FOD surface fit based on $\gamma_{\alpha,\beta}$ as the basic hysteresis block ($f = 4$ Hz).

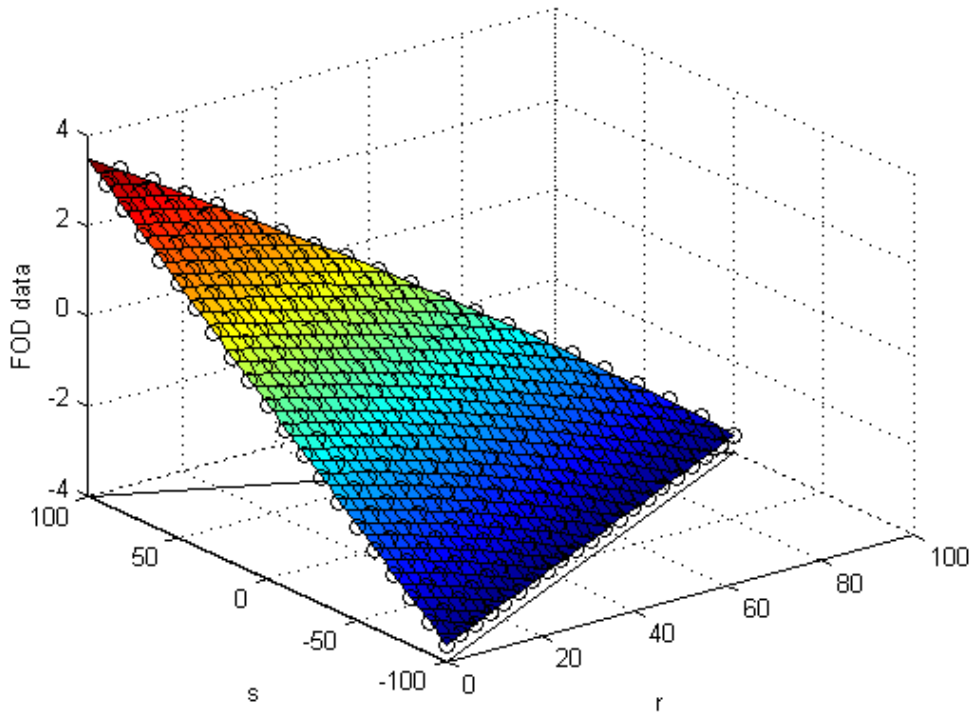

Figure 3.33: FOD surface fit based on $\gamma_{r,s}$ as the basic hysteresis block ($f = 1$ Hz).

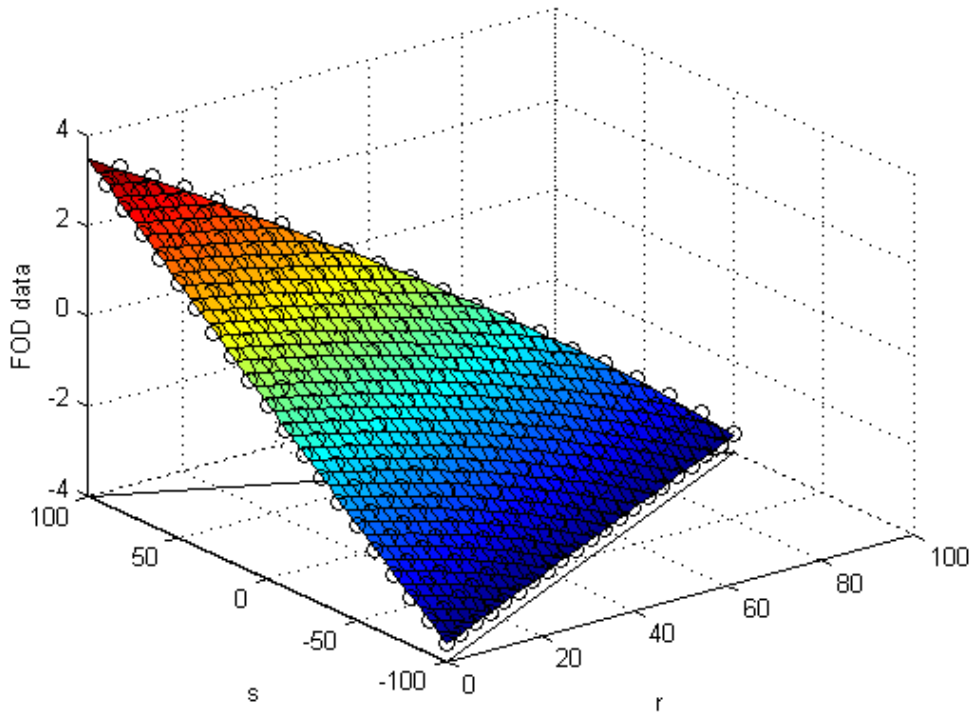

Figure 3.34: FOD surface fit based on $\gamma_{r,s}$ as the basic hysteresis block ($f = 2$ Hz).

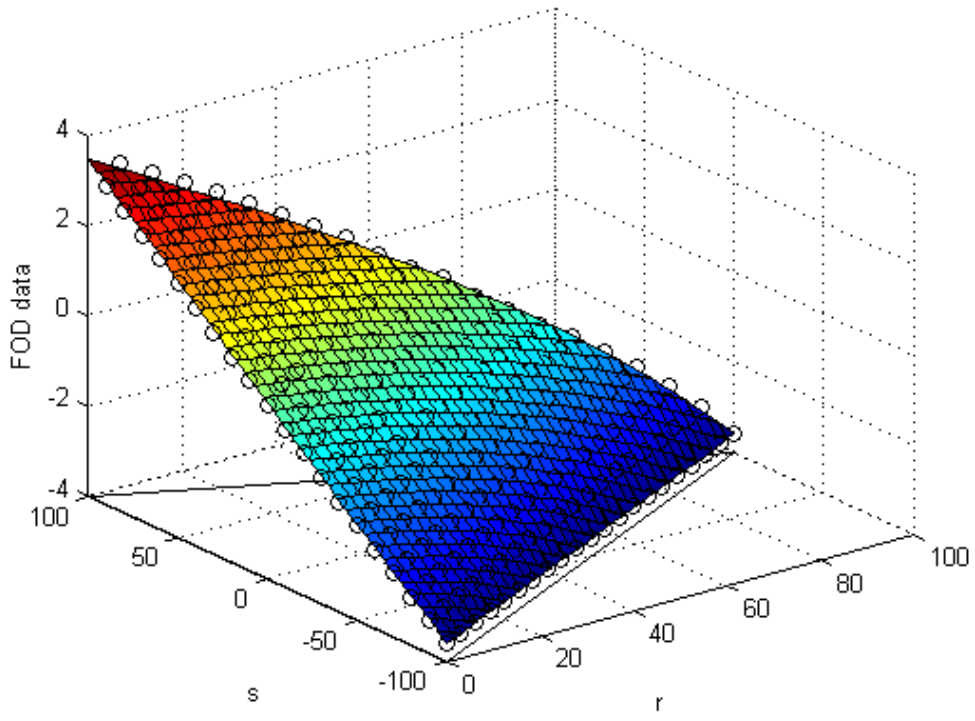

Figure 3.35: FOD surface fit based on $\gamma_{r,s}$ as the basic hysteresis block ($f = 4$ Hz).

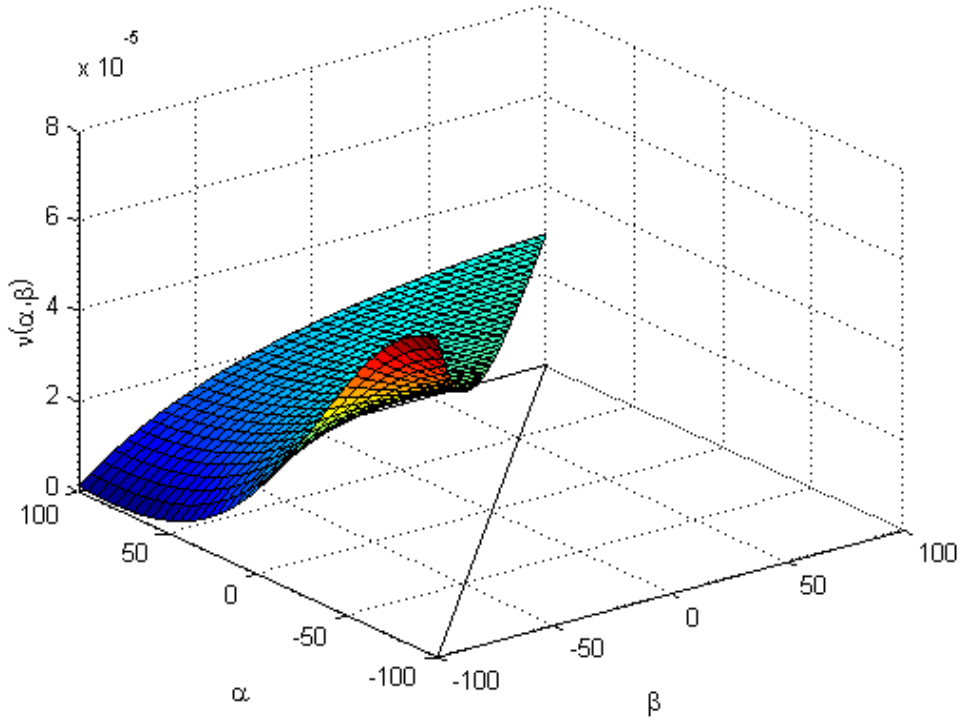

Figure 3.36: Identified weighting function: surface part based on $\gamma_{\alpha,\beta}$ as the basic hysteresis block ($f = 1$ Hz).

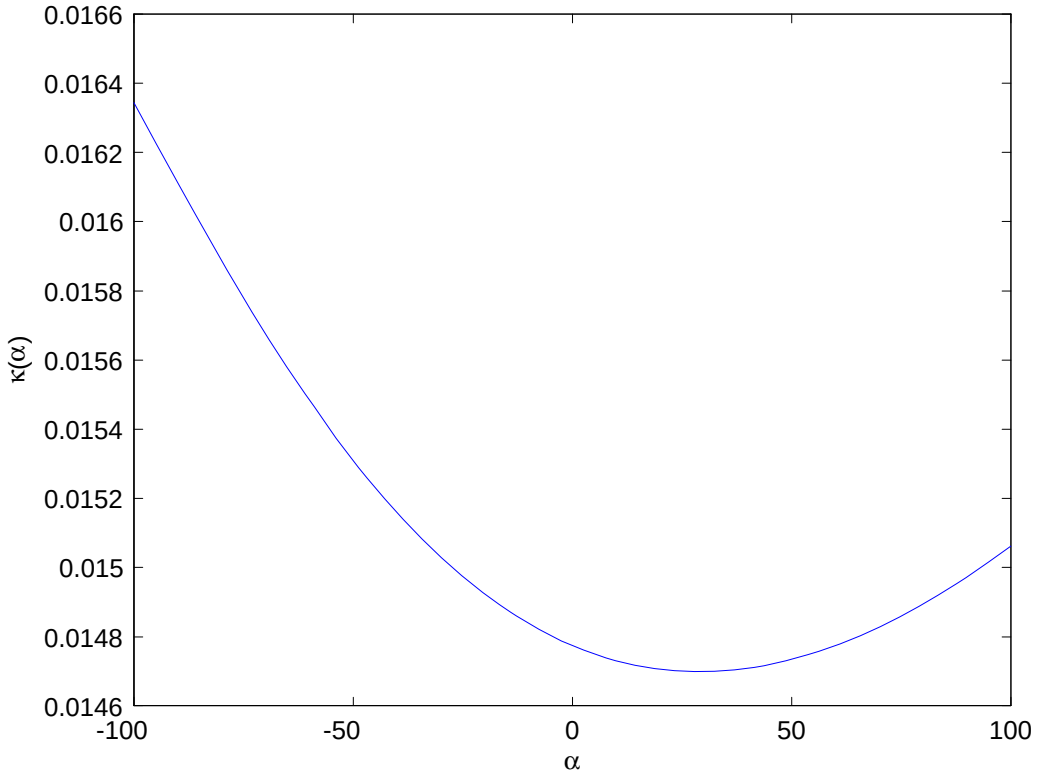

Figure 3.37: Identified weighting function: curve part based on $\gamma_{\alpha,\beta}$ as the basic hysteresis block ($f = 1$ Hz).

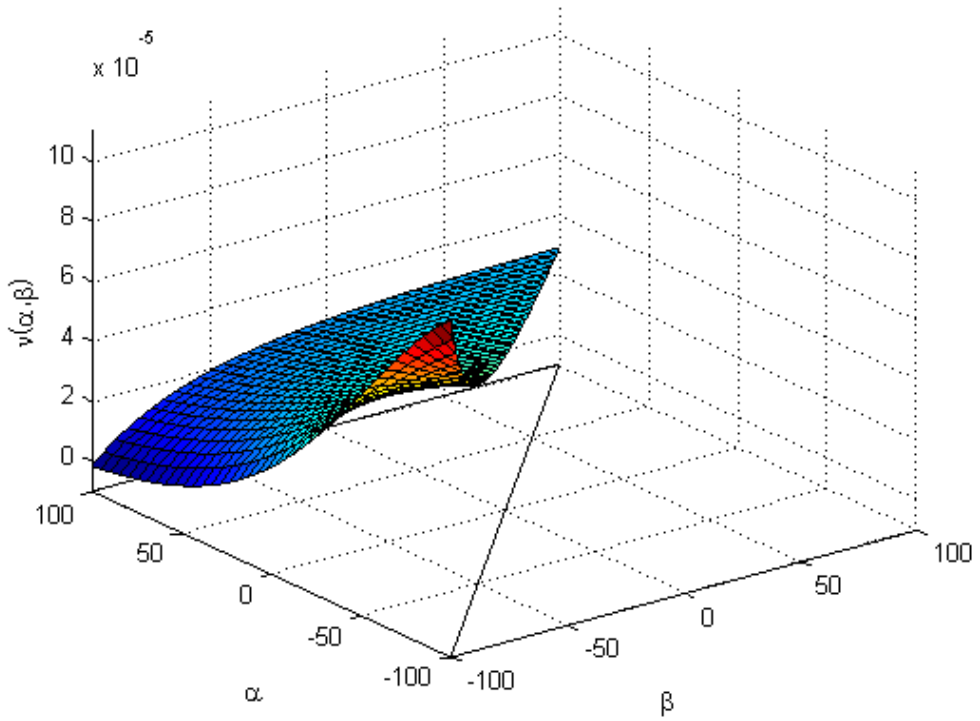

Figure 3.38: Identified weighting function: surface part based on $\gamma_{\alpha,\beta}$ as the basic hysteresis block ($f = 2$ Hz).

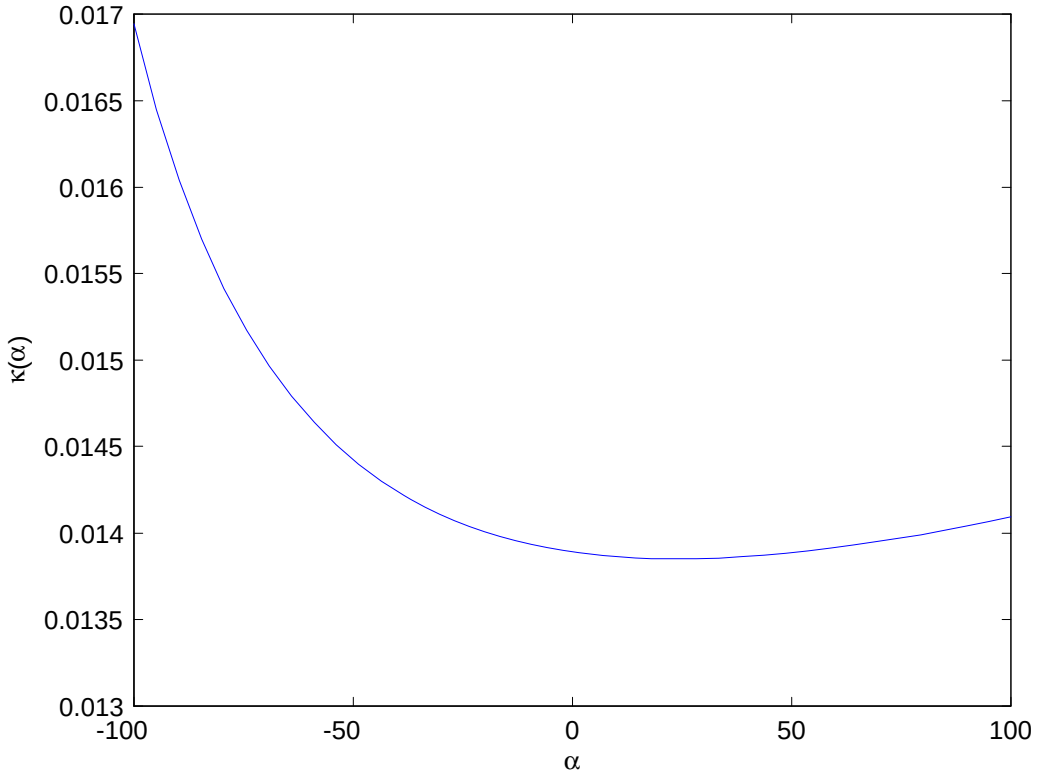

Figure 3.39: Identified weighting function: curve part based on $\gamma_{\alpha,\beta}$ as the basic hysteresis block ($f = 2$ Hz).

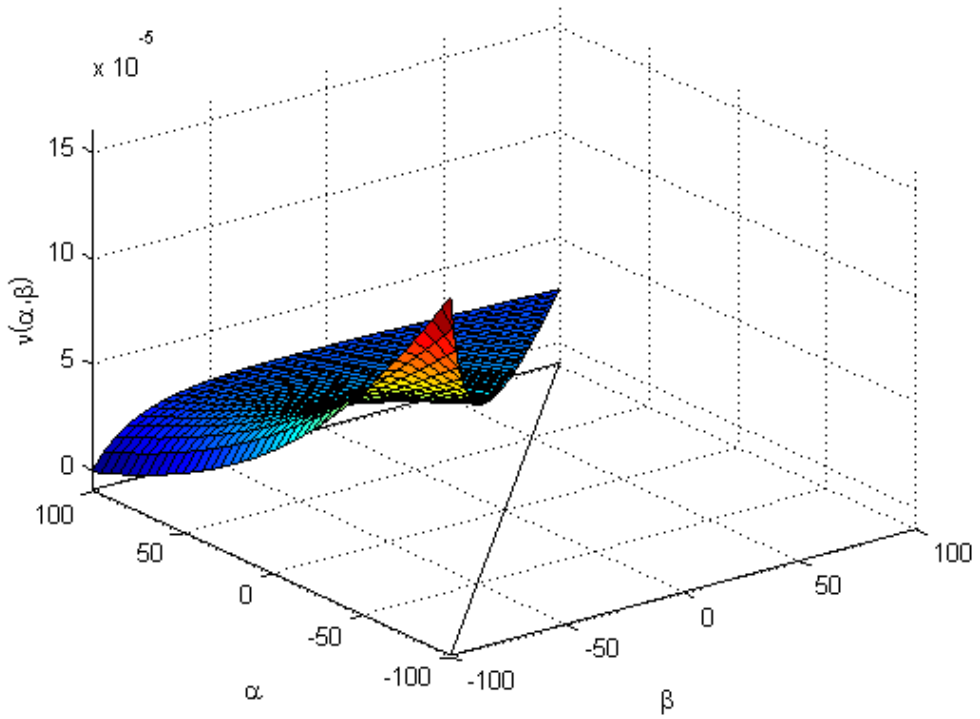

Figure 3.40: Identified weighting function: surface part based on $\gamma_{\alpha,\beta}$ as the basic hysteresis block ($f = 4$ Hz).

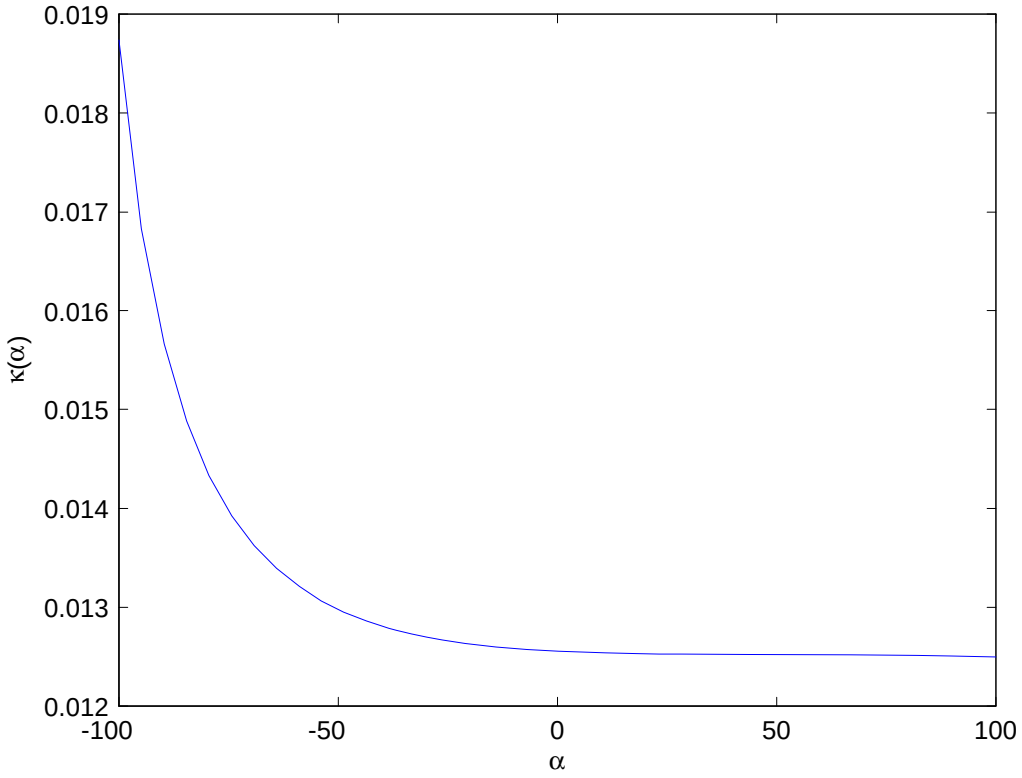

Figure 3.41: Identified weighting function: curve part based on $\gamma_{\alpha,\beta}$ as the basic hysteresis block ($f = 4$ Hz).

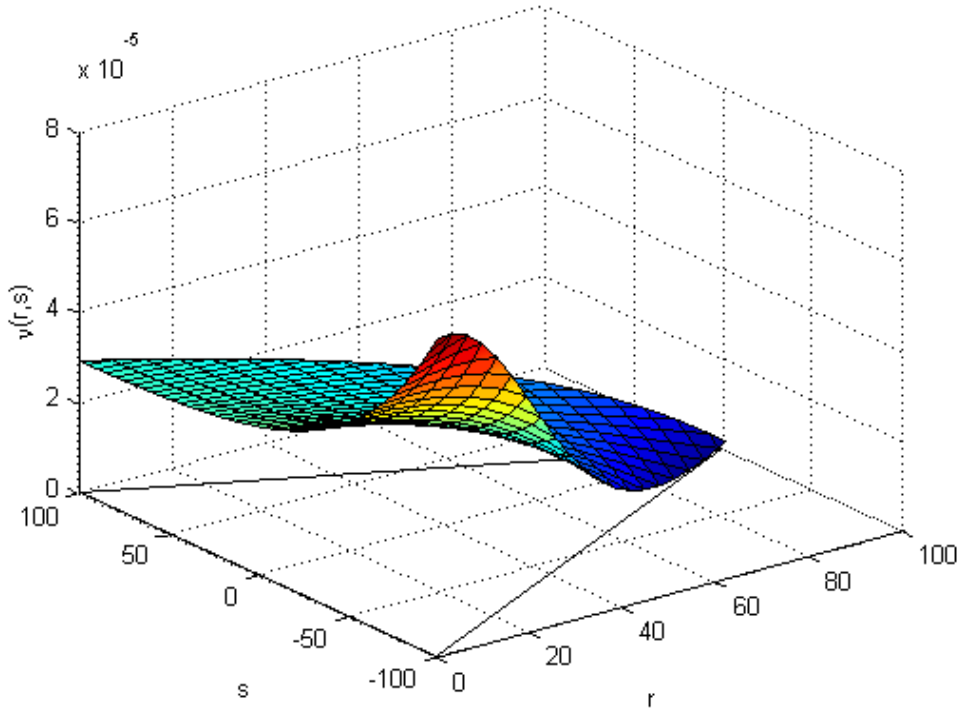

Figure 3.42: Identified weighting function: surface part based on $\gamma_{r,s}$ as the basic hysteresis block ($f = 1$ Hz).

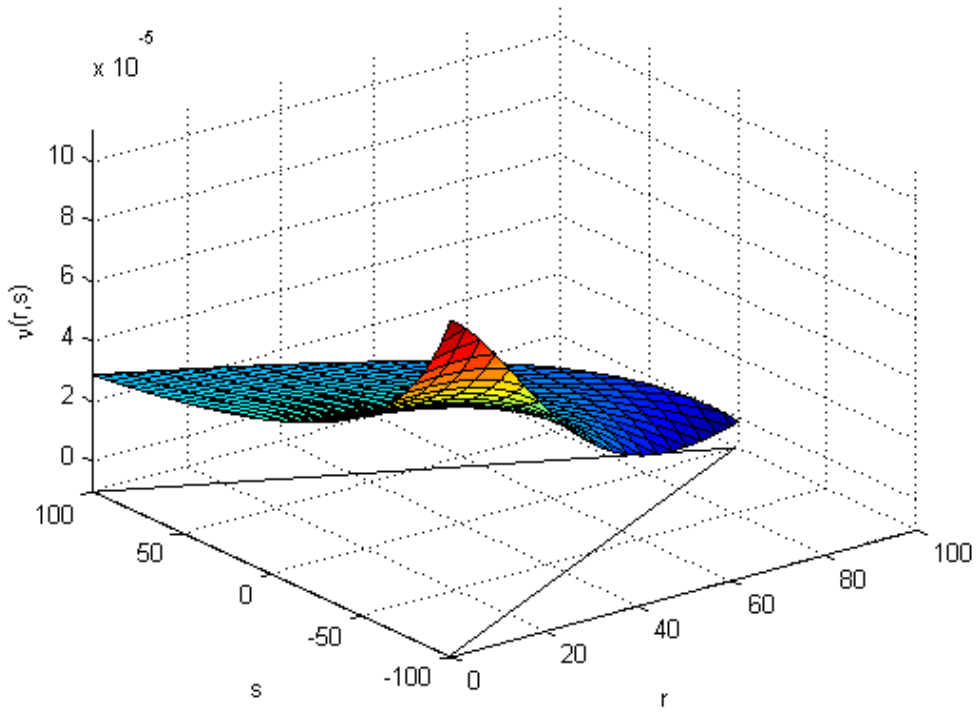

Figure 3.43: Identified weighting function: surface part based on $\gamma_{r,s}$ as the basic hysteresis block ($f = 2$ Hz).

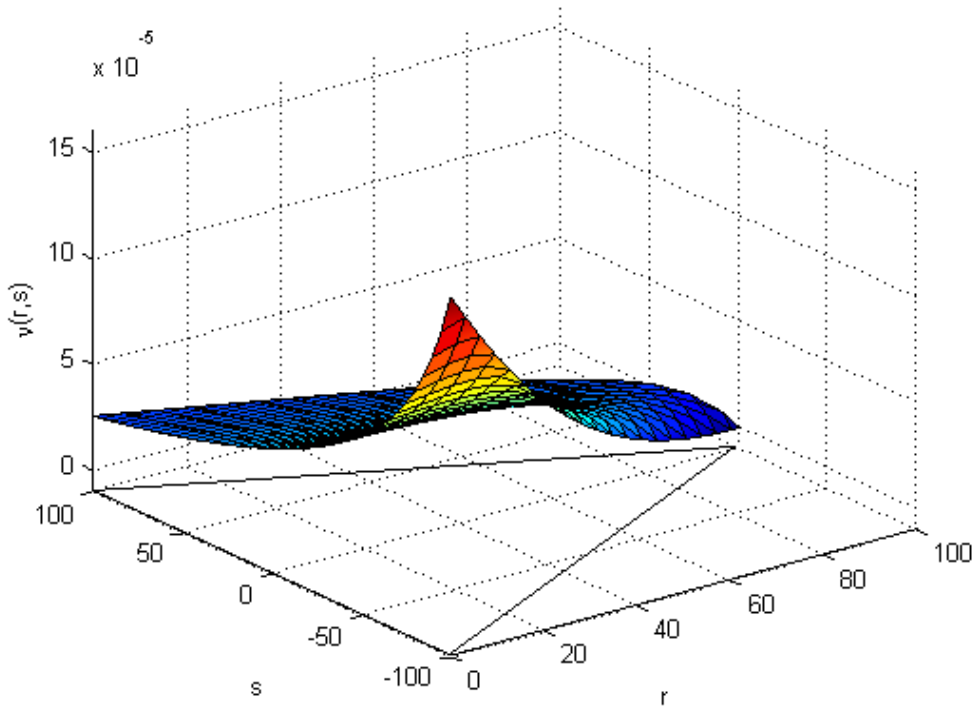

Figure 3.44: Identified weighting function: surface part based on $\gamma_{r,s}$ as the basic hysteresis block ($f = 4$ Hz).

3.3.4 Model Verification

In order to validate the model, the output of the wiping-out test, congruent minor loop (CML) test and identification input are simulated for all of the three cases. The simulation model developed in [7] is used to generate simulation results. The FOD data applied in the simulation is a linear interpolation from the experimentally collected FOD data. The simulation and experimental results of the wiping-out test in the input and output plane are shown from Figure 3.45 through 3.47 for Case 1, 2 and 3 respectively. The scalloped behavior on the ascending branches is likely caused by the linear interpolation of the FOD data since this effect is more obvious when the input signal has a higher frequency causing the hysteresis loop of a piezoceramic actuator to have a larger curvature. The error between experimental data and simulation results is represented in Figure 3.48 with stretching in the time axis for different cases. It can be observed that the error becomes larger when the input signal is at higher frequency. The error of the maximum magnitude over the whole output range is about 2.33% 4.51% and 9.23% when the input signal is at $f = 1$, 2, and 4 Hz respectively.

Similarly, the comparisons between the simulated output and experimental data in the CML test are shown from Figure 3.49 and 3.51 followed by the error between the experimental data and simulated output presented in Figure 3.52 with stretching in the time axis for different cases. Note that the modelling error increases with respect to the frequency of the input signal. The error of the maximum magnitude over the whole output range is about 2.05% 4.16% and 7.38% for the input signals at $f = 1$, 2, and 4 Hz respectively.

Finally, the comparisons between the FOD experimental data and the simulated result are shown from Figure 3.53 to 3.55. The error between the experimental output data and the simulated output data with respect to time is shown in Figure 3.56 with suitable stretching in the time axis for different cases. Note that the error between the experimental and simulated result is increased when the piezoceramic actuator is driven by the input with a higher frequency. It is found that the error of the maximum magnitude over the whole output range is about 2.42% 4.52% and 8.69% at $f = 1$, 2, and 4 Hz respectively.

From the wiping-out test, the congruent minor loop (CML) test and the FOD data, it is obvious that the error between the experimental data and simulated output increases when the frequency of the input voltage signal increases. There could be two sources of the increasing modelling error. First, the classical Preisach model is intended to describe static hysteresis, and thus, may not capture frequency dependent effects. The second likely source of discrepancy pertains to the piezoceramic actuator configuration. The experimental apparatus used in this research employs bimorph piezo actuators in a cantilevered arrangement. Recall that the bimorphs consist of piezo elements bonded on the upper and lower faces of a metal substrate. Thus, when the piezos actuate and produce a bending moment in the bimorph, the glued interface between the piezos and the metal substrate would experience shear stress. The response of this glued interface in shear is unknown. An additional mechanical factor with the bimorph is that the free end has a relatively large clip adhered to it for the purpose of interacting with the circular platform (removed in these experiments). This additional mass would undoubtedly introduce a dynamic effect that would be highly correlated with frequency. In its totality, there are several aspects of the bimorphs which likely involve mechanical dynamics, and modelling such effects is beyond the scope of the current work.

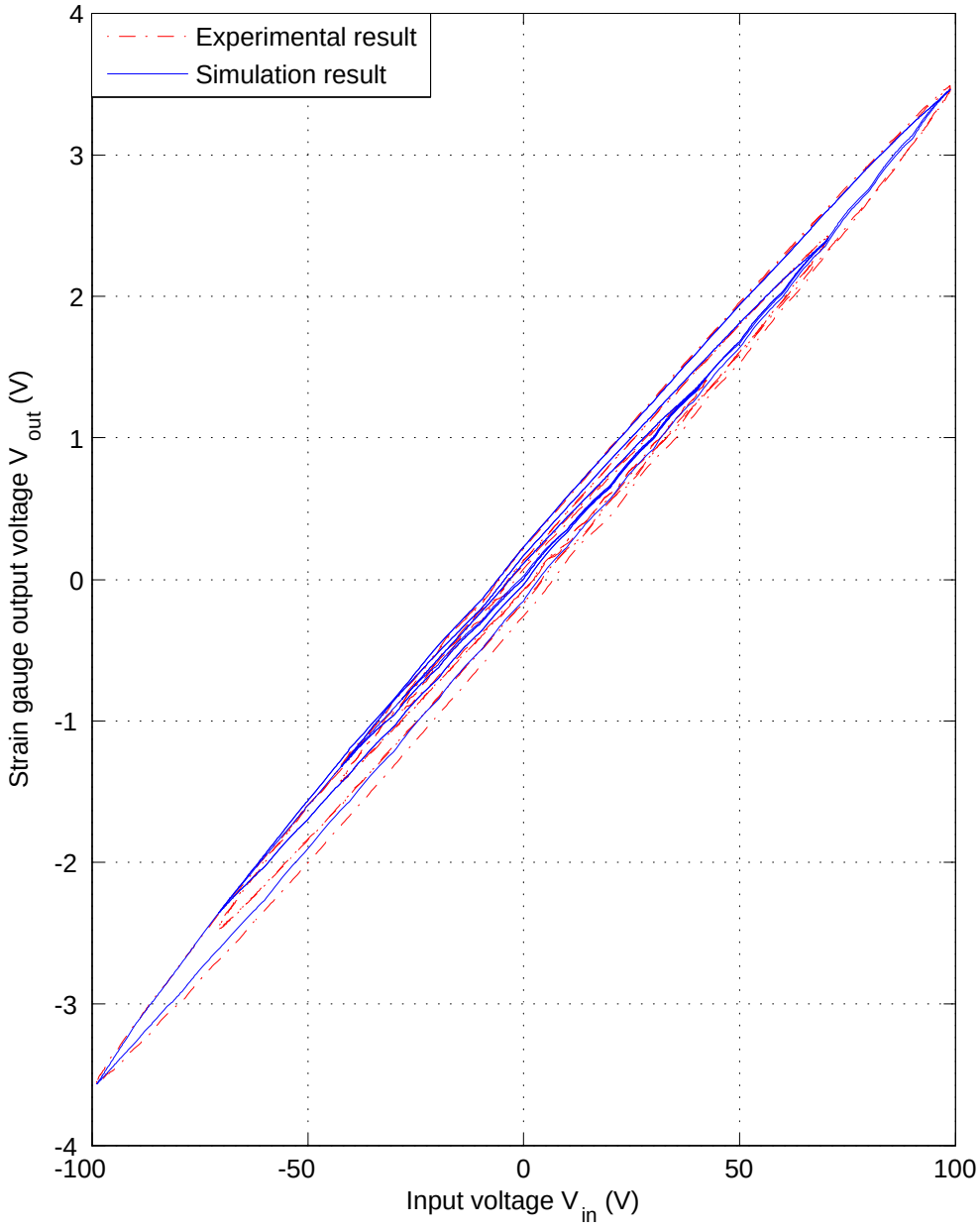

Figure 3.45: Comparison between simulation and experiment results of wiping-out test ($f = 1$ Hz).

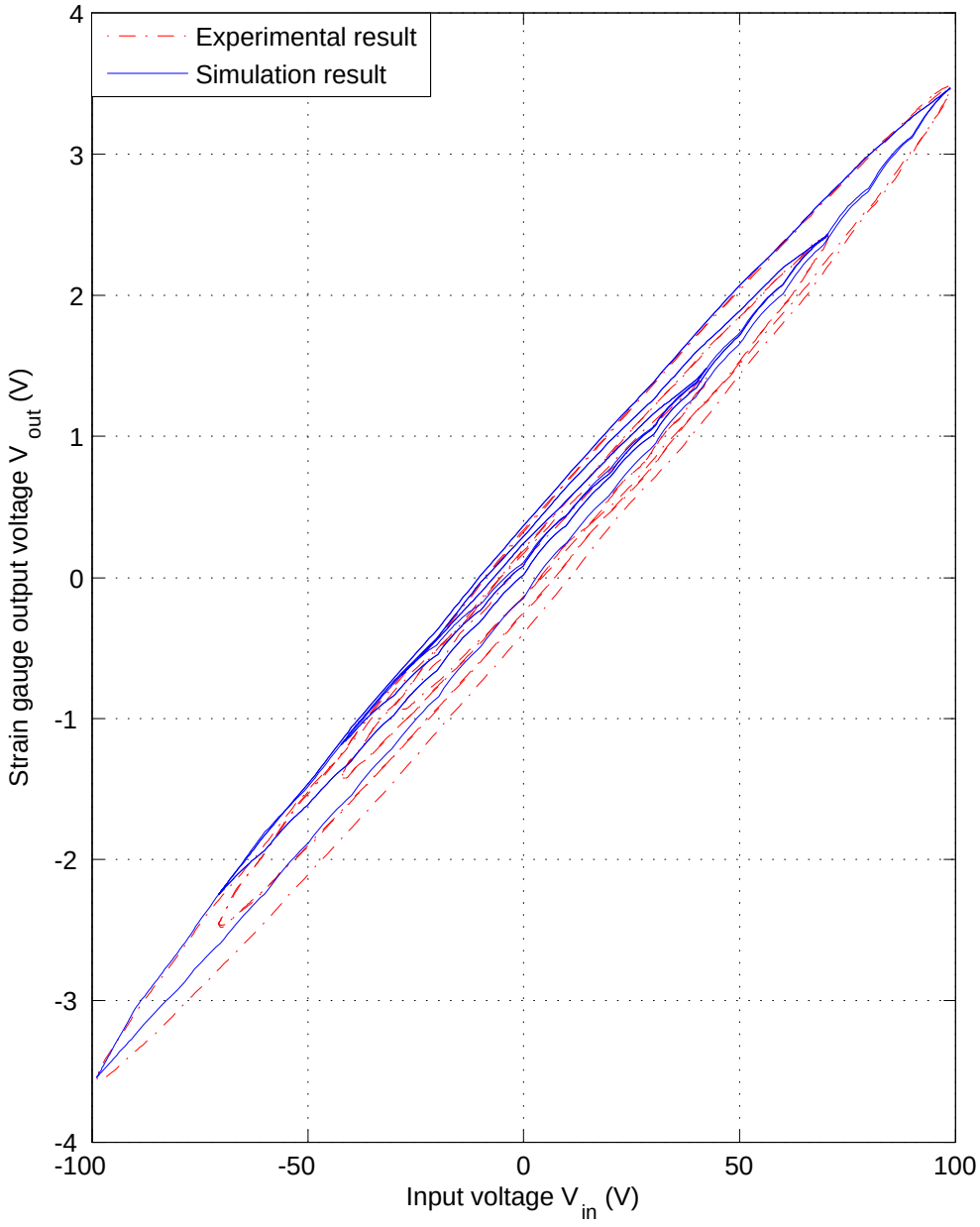

Figure 3.46: Comparison between simulation and experiment results of wiping-out test ($f = 2$ Hz).

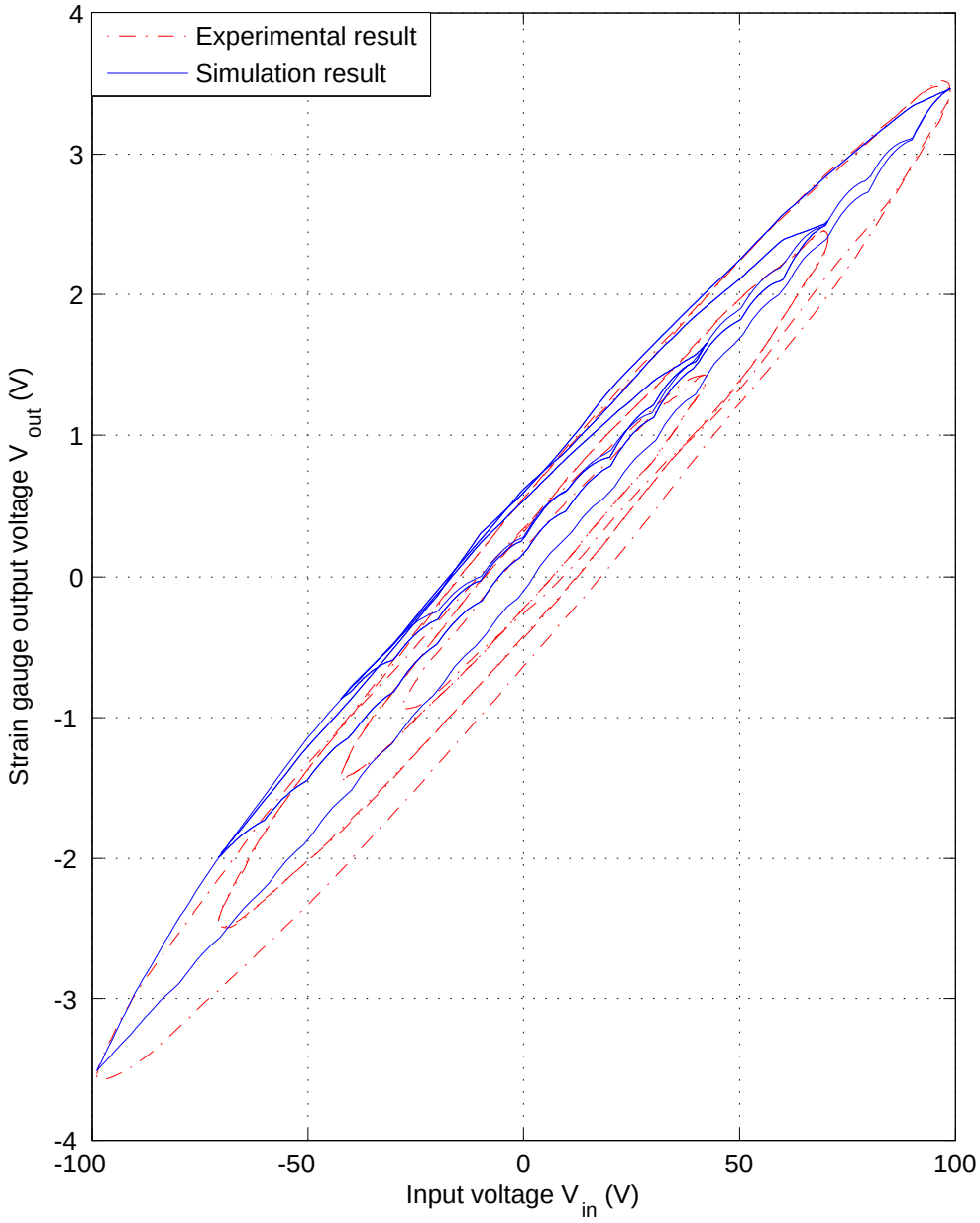

Figure 3.47: Comparison between simulation and experiment results of wiping-out test ($f = 4$ Hz).

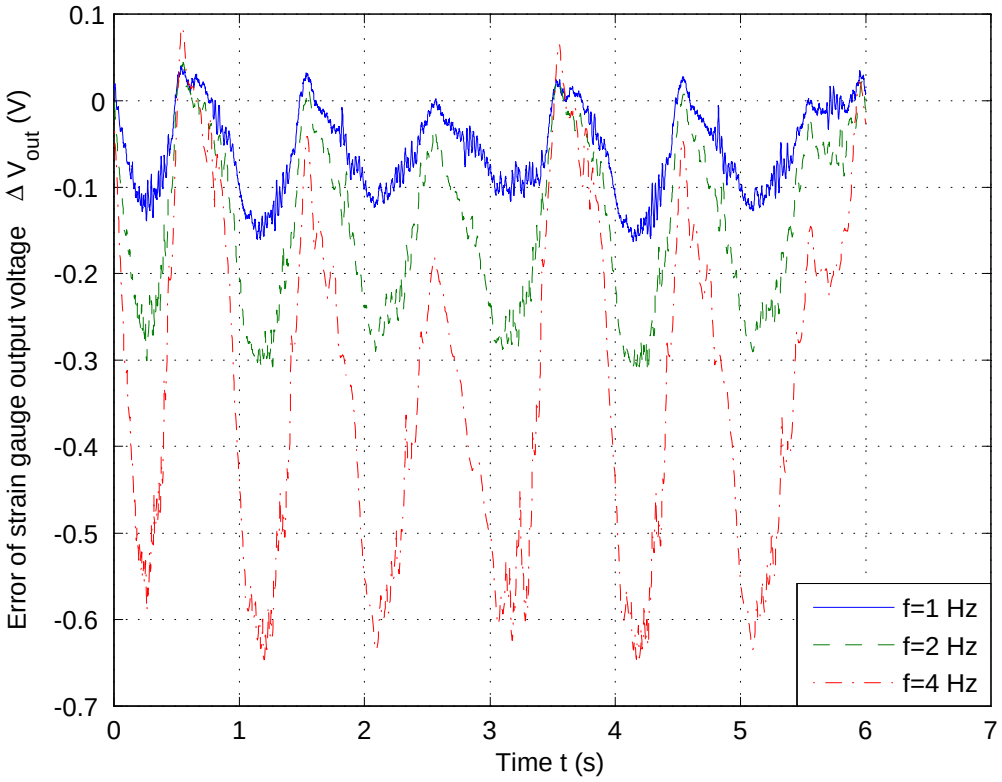

Figure 3.48: Error between experiment output and simulation output in wiping-out test (f = 1, 2, 4 Hz).

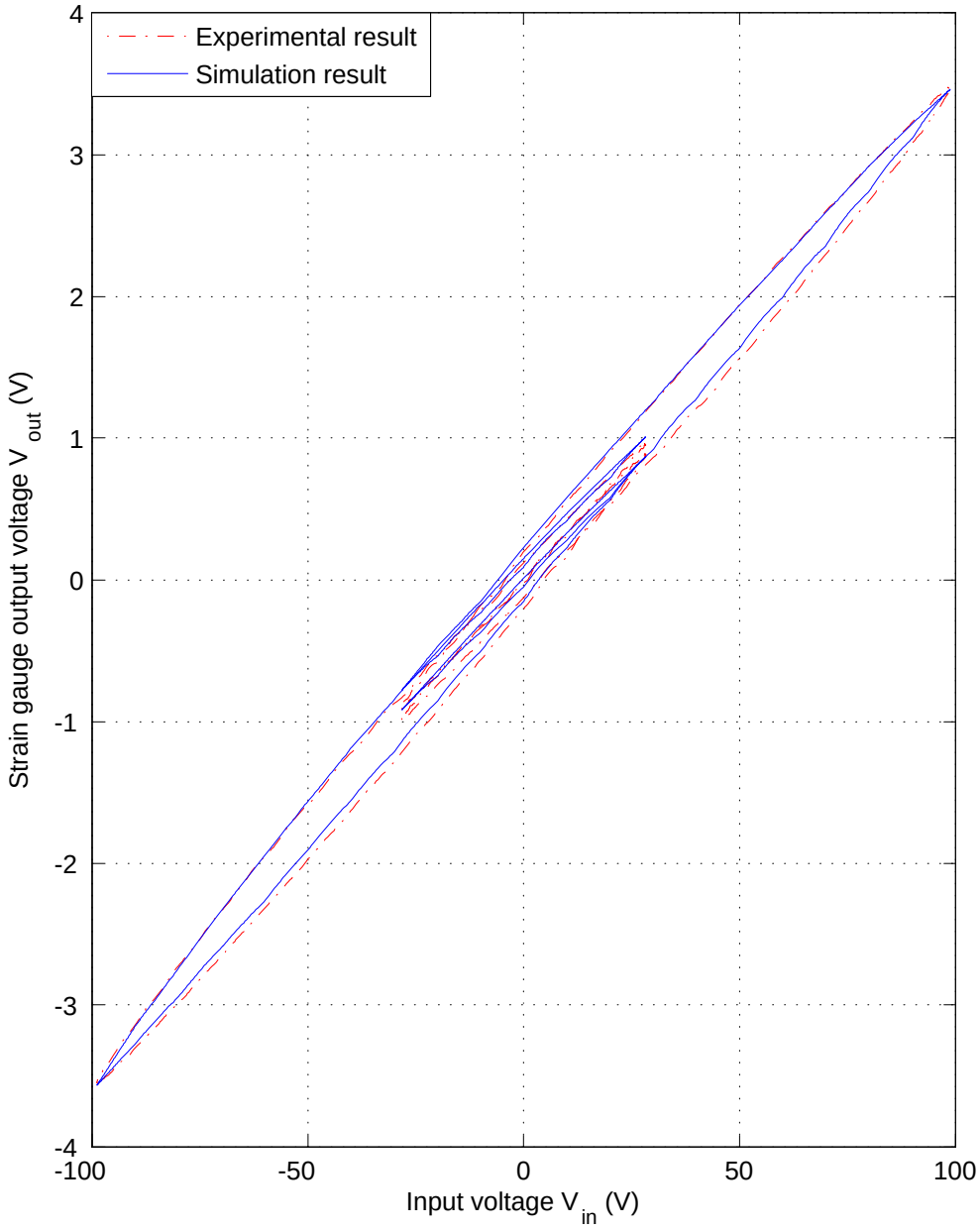

Figure 3.49: Comparison between simulation and experiment results of CML test ($f = 1$ Hz).

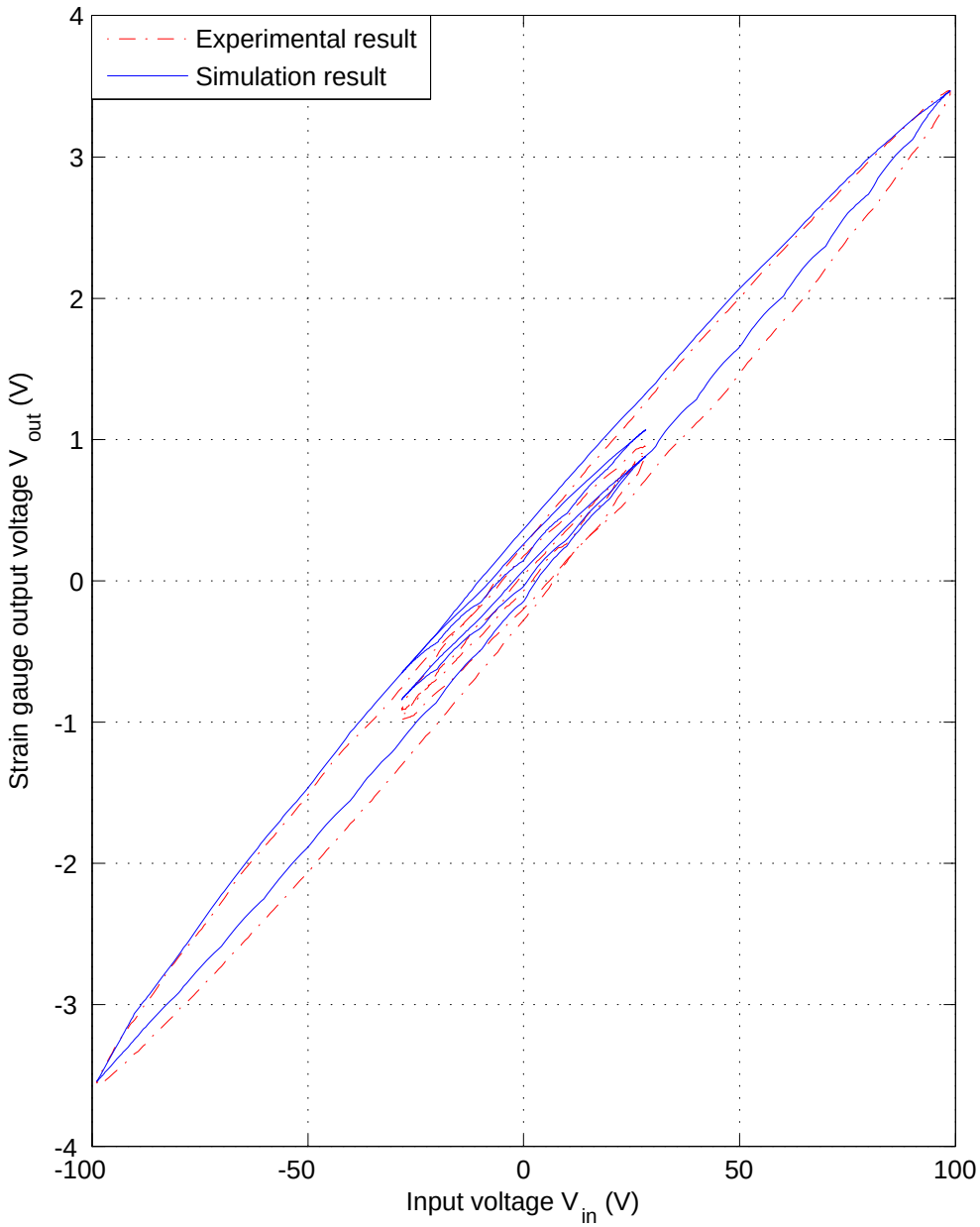

Figure 3.50: Comparison between simulation and experiment results of CML test ($f = 2$ Hz).

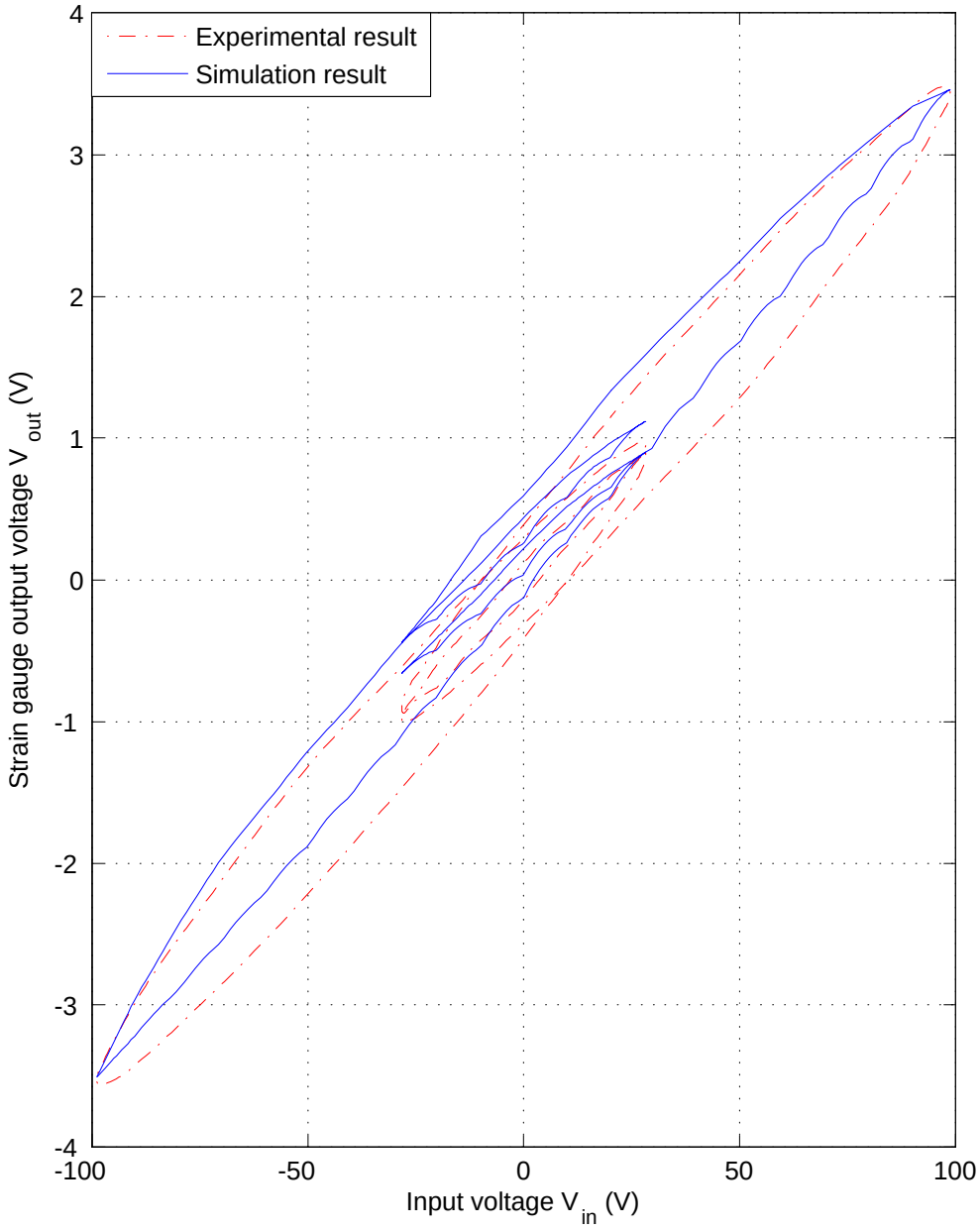

Figure 3.51: Comparison between simulation and experiment results of CML test ($f = 4$ Hz).

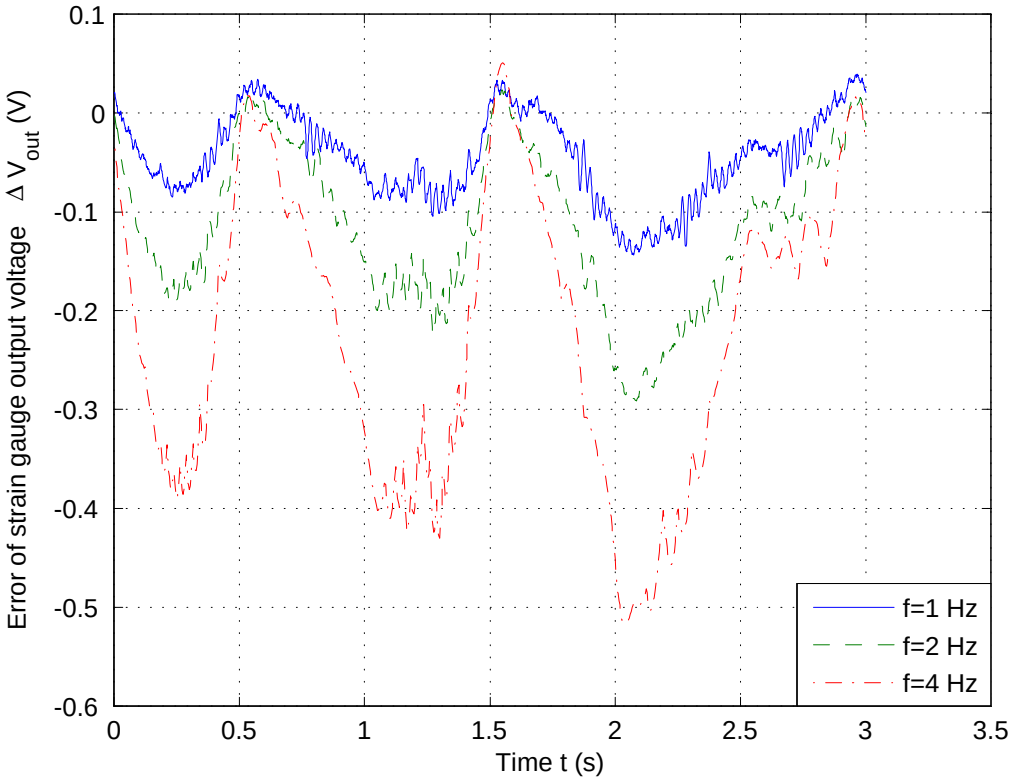

Figure 3.52: Error between experiment output and simulation output in CML test (f = 1, 2, 4 Hz).

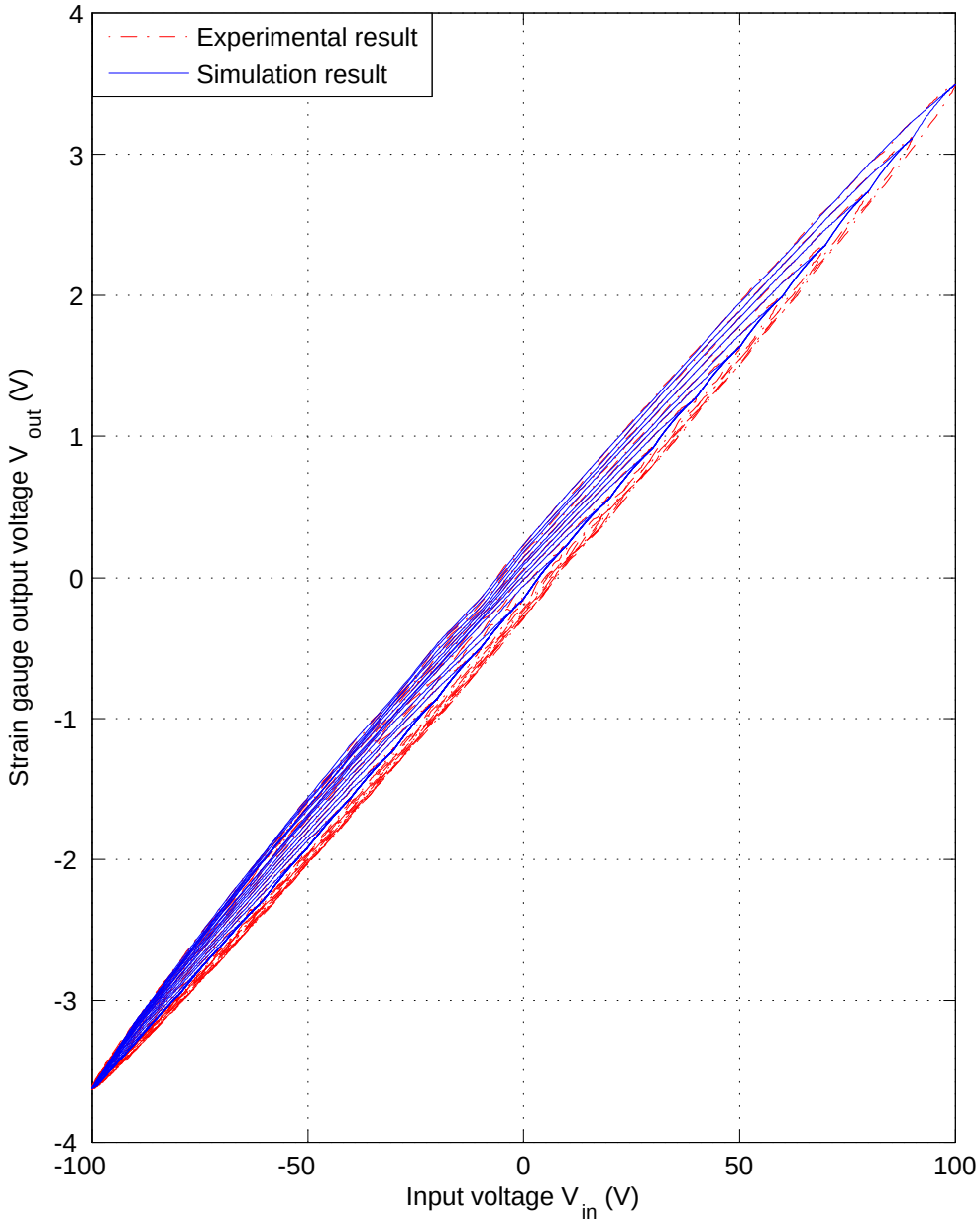

Figure 3.53: Comparison between simulation and experiment results of identified FOD data ($f = 1$ Hz).

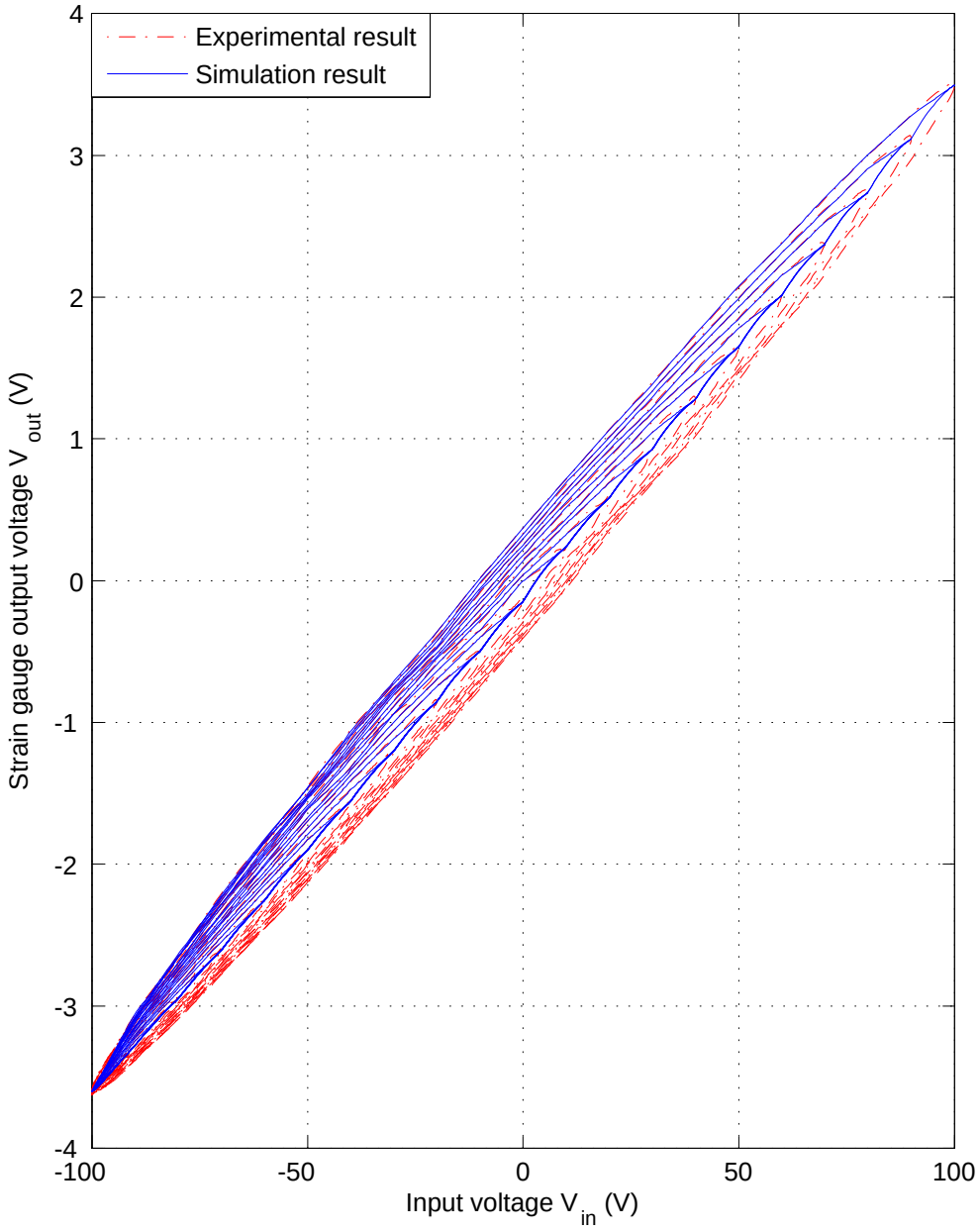

Figure 3.54: Comparison between simulation and experiment results of identified FOD data ($f = 2$ Hz).

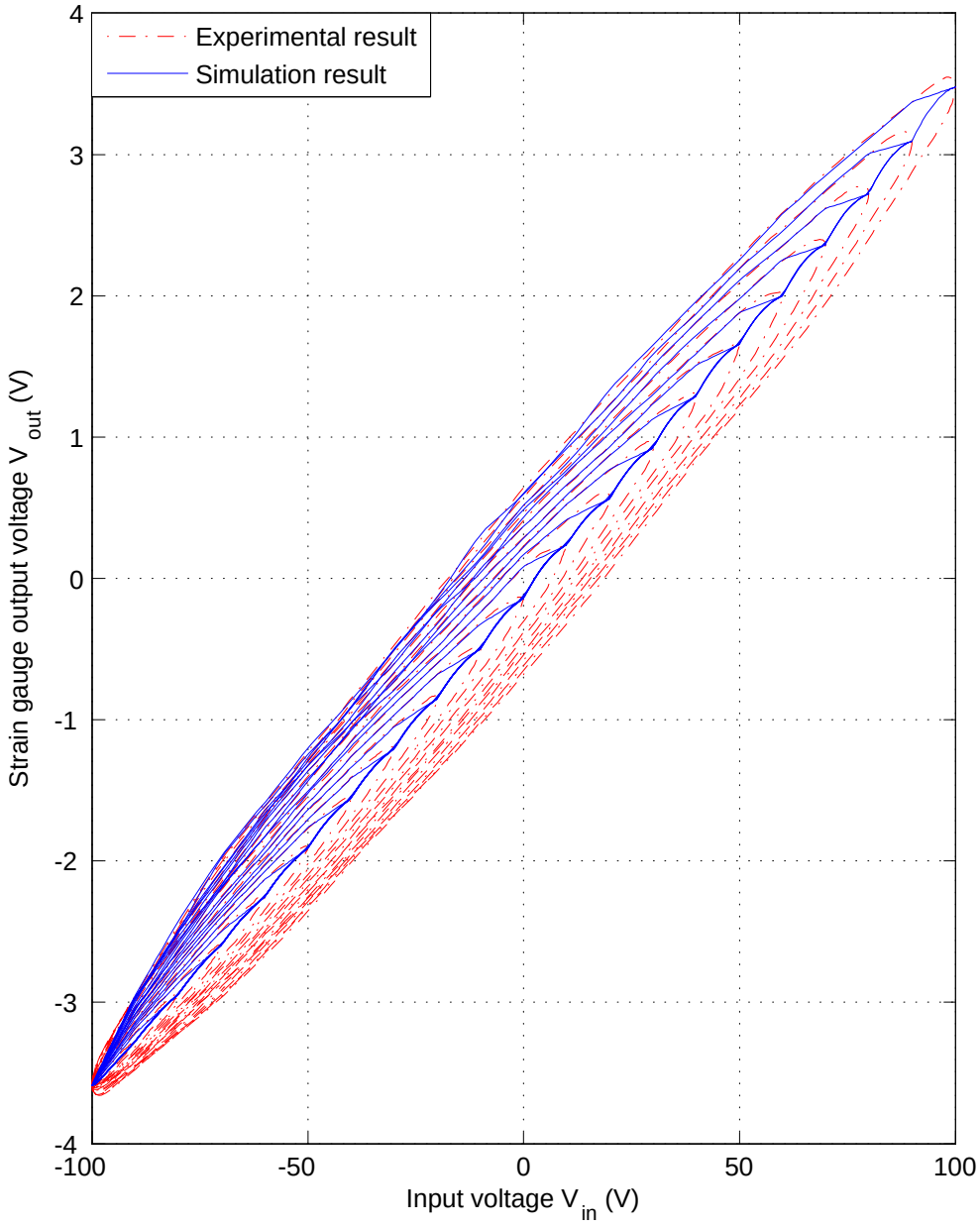

Figure 3.55: Comparison between simulation and experiment results of identified FOD data ($f = 4$ Hz).

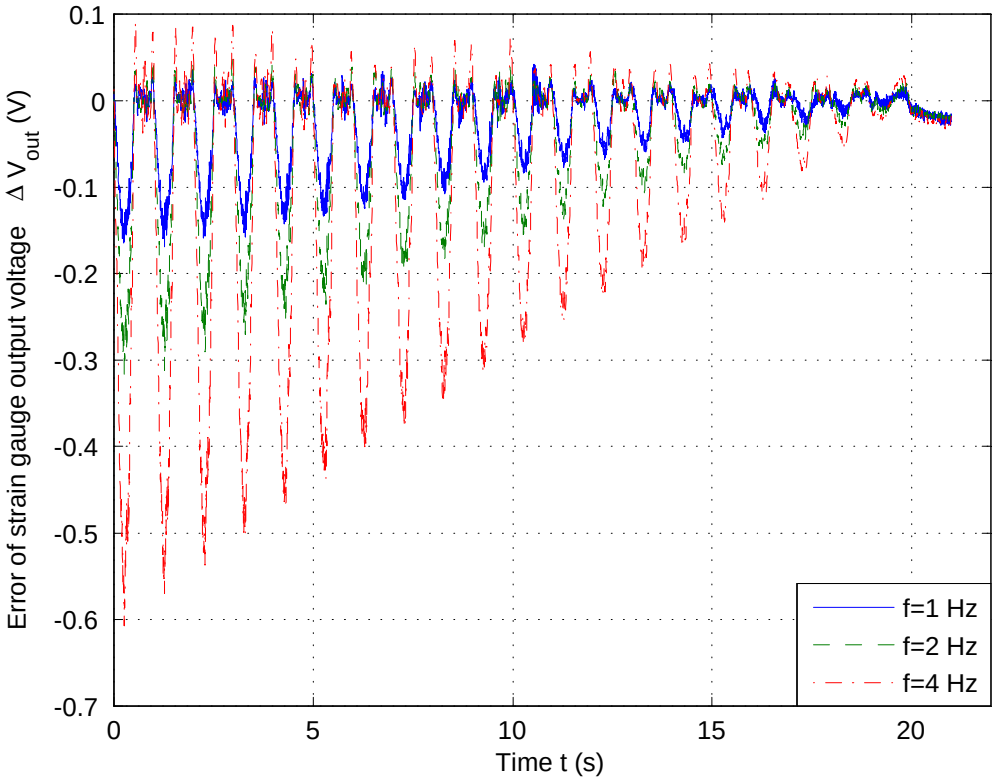

Figure 3.56: Error between experiment output and simulation output of FOD curves ($f = 1$, 2, 4 Hz).

Chapter 4

Open-Loop Drift Tests Based on Input Noise Injection

As noted in Chapter 1, piezoceramics are well suited for high precision shape control. An active material as such is able to modify and maintain its shape with spatially distributed piezoceramic elements; and they offer high resolution down to the subnanometer range, high stiffness, low wear and tear, and fast response times [3]. In such applications, the shape control problem can be converted into a series of independent distributed regulation control problems [4].

However, the inherent hysteresis of piezoceramic actuators makes the setpoint regulation problem much more difficult than that for linear systems as pointed out in [7]. It is interesting to notice that for a given desired setpoint y_d, and a hysteresis read-out operator Γ_r, there exists a set of equivalent states Ψ_{eq}^{d} such that for any state $\psi_{eq}^{d} \in \Psi_{eq}^{d}$, $\Gamma_r\left(\psi_{eq}^{d}\right) = y_d$. This observation provides one more degree of freedom to accomplish the open-loop regulation task. Moreover, an important measure of open-loop regulation performance is the maximum output transient caused by noises because this measurement describe the deviation from the desired shape. Thus, the open-loop regulation task for a hysteresis system is defined as follows.

Problem 1 (Open-Loop Regulation Task) *Let t_r be a time instant, $\eta(t)$ be a uniformly distributed noise, and $\Psi_{eq}^{y_d}$ be the set of equivalent states for a given Preisach system with readout operator: $\Gamma_r(\Psi) \rightarrow Y$ and a desired output $y_d \in Y$. Suppose the input $u(t) = \bar{u}_d + \eta(t)$ when $t > t_r$, where $\|\eta(t)\|_\infty = \xi$ and $\bar{u}_d = u_d(t_r) = \psi_{eq}^{d}(t_r, 0) \in \Psi_{eq}^{y_d}$. When $t < t_r$, choose the initial state and design an input $u_d(t)$ to drive to that state, so that the derivative of the output with respect to the input during open-loop regulation in the presence of input noise is minimized.*

Intuitively for a hysteretic system, the set of equivalent states provide us one more degree of freedom, the initial state, to accomplish a regulation task. In this chapter, the notion of regulating a hysteretic system around a neutral state for the purposes of improved input noise rejection is investigated in both simulations and experiments. This is accomplished via open-loop drift tests performed on the computer based shape control system driven by piezoceramic actuators described in Chapter 3. The differential drift [7] before and after the injection of noise on the input are investigated based on the different initial states ψ_a, ψ_d and ψ_n. These states exist

on the ascending curve of the major hysteresis loop, the descending curve of the major hysteresis loop and the locus of neutral states $N(l)$ respectively as defined by Eq. (2.16) and corresponding to a given desired output position where $\Gamma_r(\psi_a) = \Gamma_r(\psi_d) = \Gamma_r(\psi_n) = y_d = 1$. However, the hysteresis found in piezoceramic actuators is frequency dependent. Thus, input voltage signals V_{in} with frequencies $f = 1$, 2, and 4 Hz are applied in order to reach the initial states ψ_a, ψ_d and ψ_n for the open-loop drift tests.

The piezoceramic actuators of the SS15 are in a bimorph configuration, which is different from the stack actuator investigated in [7]. Thus, a uniformly-distributed random noise input u_d is generated and filtered offline. The cut-off frequency of the filter is determined by the resonance frequency of the bimorph piezoceramic actuator investigated in the first section of this chapter. The implementation procedure of the simulations and experiments is listed in the second section. Both simulation and experimental results are shown and discussed in the third and fourth sections. The simulations are generated according to the Preisach model using the FOD data collected from the shape control unit SS15, while the experimental data is collected directly from the SS15 by following a slightly modified procedure to account for the dynamics of the Flexmorph itself.

4.1 Noise sequence generation

The effect of input noise on a piezoceramic actuator of the SS15 is examined in this thesis using a zero-mean uniformly-distributed random noise input u_d generated offline.

The configuration of the piezoceramic bimorph actuators in the SS15 is constructed as a cantilever. In order to avoid resonance of the cantilever and generating results that are difficult to interpret, the natural frequency f_n of the piezo actuated beam is identified from an initial experiment implemented on the shape control system. The rationale is that the cut-off frequency of the noise input u_d can be determined according to f_n. At the anhysteretic state, a step signal of small amplitude, i.e. 7V is applied to the bimorphs of the SS15 and the response is recorded. From the free vibration result shown in Figure 4.1, the natural frequency is 37.62 Hz as shown in the single-sided amplitude spectrum of the strain gauge output $V_{out}(t)$ shown in Figure 4.2.

Based on the natural frequency identified, i.e. $f_n = 37.62$ Hz, a noise sequence with amplitude 0.5 V and with cut-off frequency 15 Hz is generated for the open-loop drift test. It is observed that the sample time used in the Uniform Noise Generator[1] needs to be reduced to 0.015 s in order to retain the noise amplitude after the low pass filter with 15 Hz cut-off frequency. When a larger sampling time is set in the Uniform Noise Generator, the original noise signal is generated over a smaller frequency range. Thus, a smaller portion of the noise is filtered by the low-pass filter. As a result the filtered noise amplitude is not significantly reduced and this is depicted in the first two seconds of the noise sequence shown in Figure 4.3. The power spectral density of the filtered noise sequence shown in Figure 4.4 shows that the main power component of the noise sequence is below 15 Hz.

[1] Simulink block of Matlab Version 7.5.0.342 (R2007b)

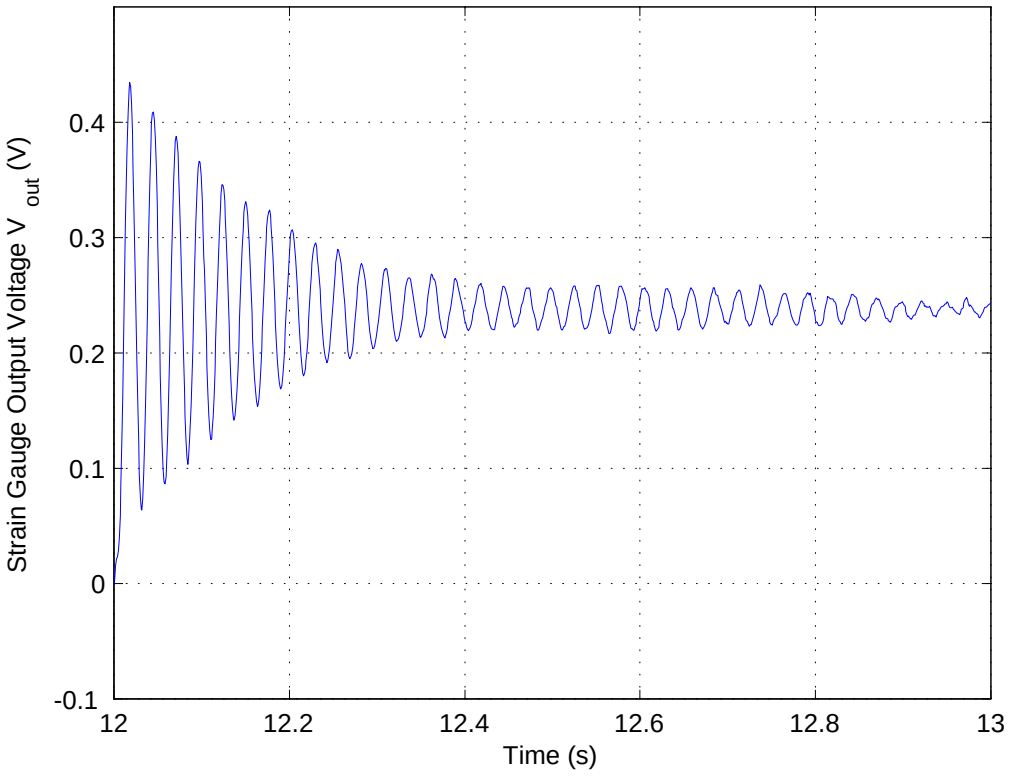

Figure 4.1: Step response $V_{out}(t)$.

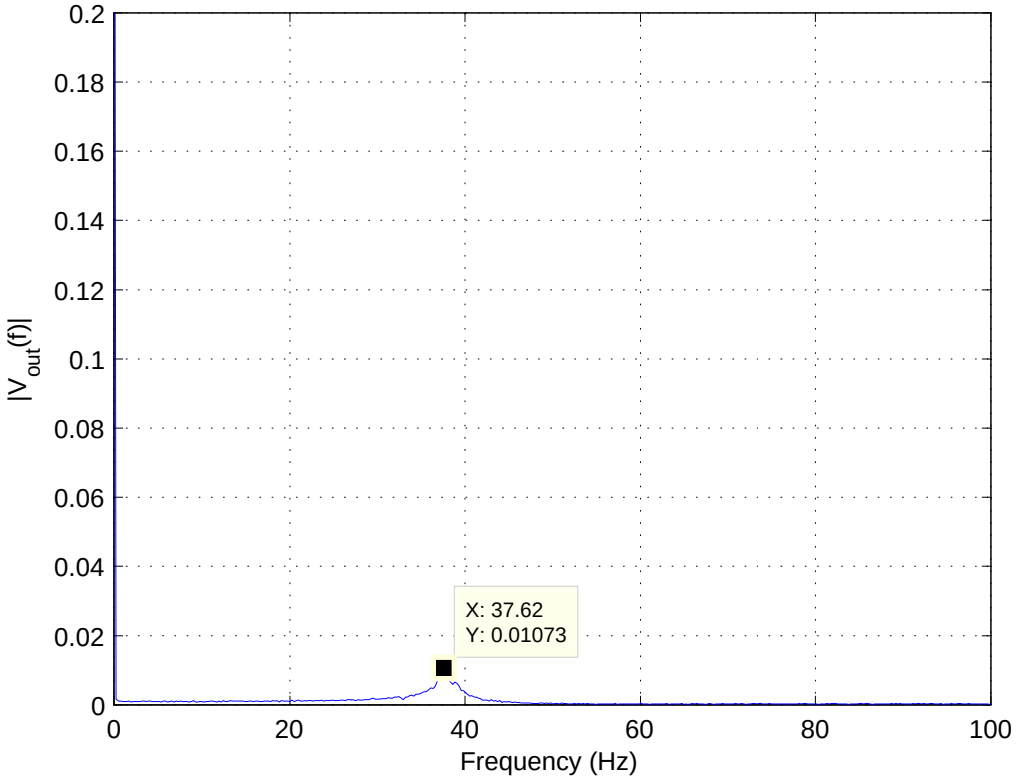

Figure 4.2: Single-sided amplitude spectrum of output $V_{out}(t)$.

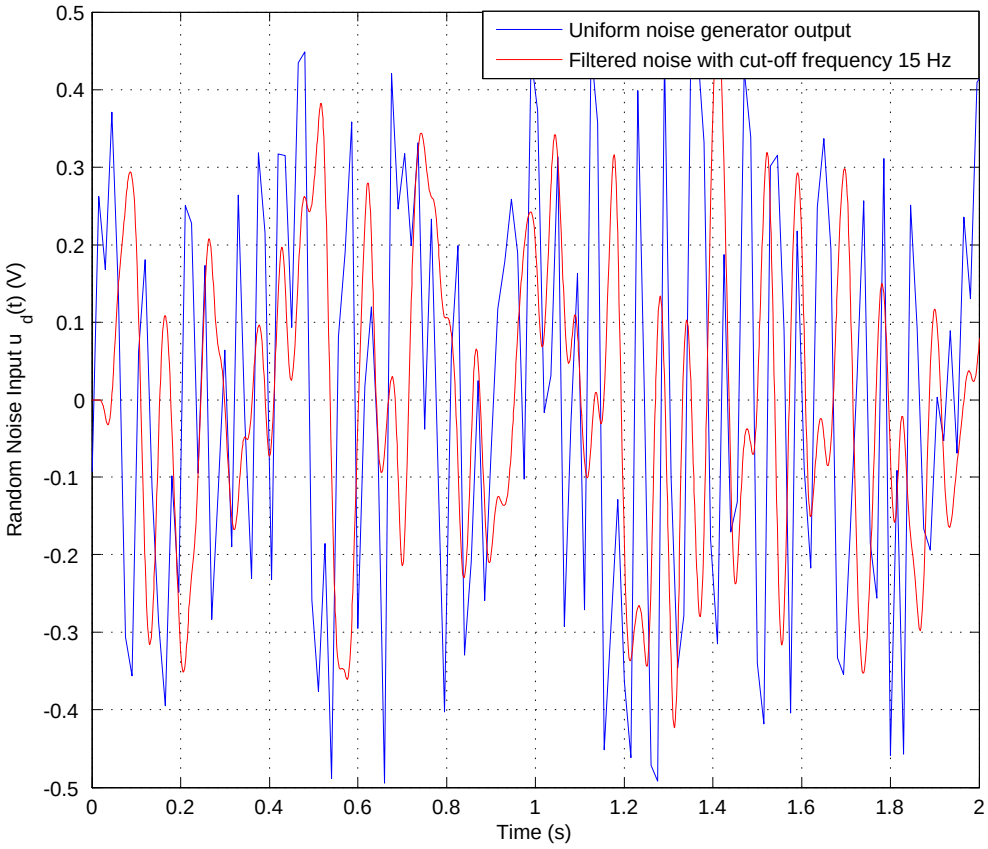

Figure 4.3: Noise sequence before and after filter.

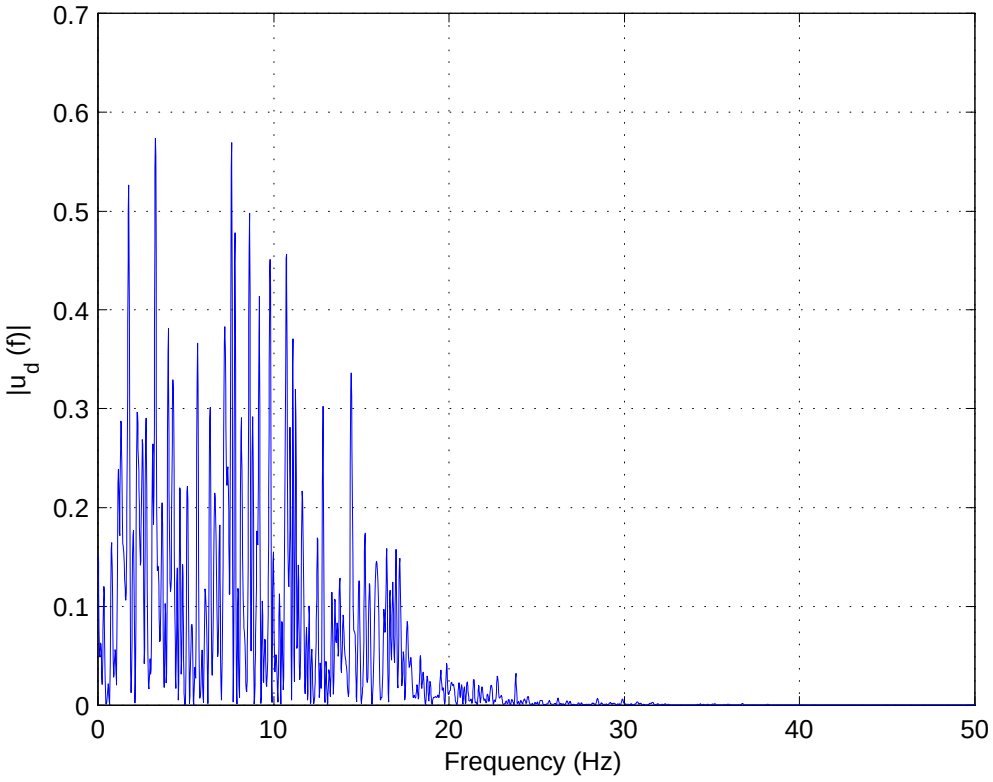

Figure 4.4: Power spectral density from filtered noise sequence generated by uniform noise generator.

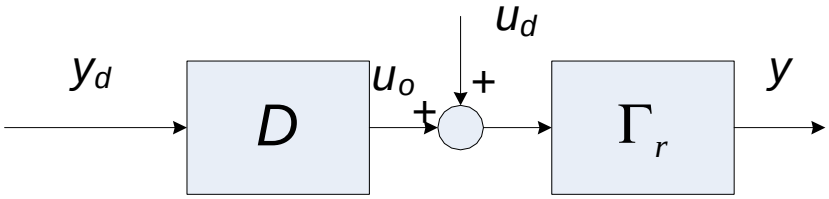

Figure 4.5: Open-loop system schematic for input noise injection tests.

4.2 Implementation Procedure of Open-Loop Simulations and Experiments

In the following sections, the open-loop response in the presence of input noise is investigated in both simulation and experiment using the shape control system. It is expected that the output drift would vary depending on different initial states as a result of the hysteresis found in the piezo actuators. It is also expected that for a given desired output y_d, the output drift due to input noise will be lower when the system starts from a neutral state ψ_n^l. Moreover, the lower output drift in the open-loop response should lead to a lower control effort in the closed-loop response based on a PI regulator as hypothesized in [7].

The open-loop system for comparative tests is illustrated in Figure 4.5. For a given desired output y_d, an input u_o is generated by D such that it can drive the system to the corresponding desired initial state, which can be a neutral state ψ_n, a state ψ_a on the major ascending branch of the hysteresis or a state ψ_d on the major descending branch of the hysteresis.

If the desired state is ψ_n and $l \in [-\hat{u}, 0) \cup (0, \hat{u}]$, then $u_o = u_l$ as shown in Eq. (4.1). It is modified from [7] by specifying the amplitude of the input used to wiping-out the boundary $\psi(t_0)$.

$$u_l(t) = \begin{cases} \frac{t_1 - t}{t_1 - t_o}\left(sgn(l) \times \hat{u} - l\right) \sin\left(2\pi f\left(t - t_0\right) + \frac{\pi}{2}\right) + l & t_o < t < t_1,\ l \neq 0 \\ l & t \geq t_1,\ l \neq 0 \end{cases} \tag{4.1}$$

where $t_1 > t_o$, f is the input frequency to drive the system output to the desired initial state ψ_n, and $\hat{u}$ is the maximum input saturation. If the desired state is ψ_n and $l = 0$, then

$$u_l(t) = \begin{cases} \frac{t_1 - t}{t_1 - t_o}\hat{u} \sin\left(2\pi f\left(t - t_0\right) + \frac{\pi}{2}\right) & t_o < t < t_1 \\ 0 & t \geq t_1 \end{cases} \tag{4.2}$$

where $t_1 > t_o$. D in Figure 4.5 is a combination of N^{inv}, as defined in Section 2.8 by Eqs. (2.19) and (2.20), and Eq. (4.1) or Eq. (4.2). According to the desired output y_d, N^{inv} determines the parameter l, then $u_o = u_l$ as defined by Eq. (4.1) or Eq. (4.2) in order to generate the desired state ψ_n.

If the desired state is ψ_a, u_o is generated by a one and a half period sinusoidal wave, which is in the form of

$$u_o = \begin{cases} \hat{u} \sin\left(2\pi f\left(t - t_0\right) + \theta_a\right) & t_o < t < t_0 + 1/f \\ \frac{(\bar{u} + \hat{u})}{2} \sin\left(2\pi f\left(t - t_0\right) + \theta_a\right) + \frac{(\bar{u} - \hat{u})}{2} & t_0 + 1/f \leq t \leq t_0 + 1.5/f \\ \bar{u} & t > t_0 + 1.5/f \end{cases} \tag{4.3}$$

where f is set to be 1, 2 and 4 Hz in separate trials, $\theta_a = -\frac{\pi}{2}$, $\hat{u} = 7$. $\bar{u}$ is determined during the first half period of the sine wave, which drives the system into the range close to the desired output y_d, i.e. $[y_d - 0.03, y_d + 0.03]$. Similarly, if the desired state is ψ_d, u_o is generated by a one and a half period sinusoidal wave, which is in the form of

$$u_o = \begin{cases} \hat{u}\sin\left(2\pi f\left(t - t_0\right) + \theta_d\right) & t_o < t < t_0 + 1/f \\ \frac{(\bar{u}+\hat{u})}{2}\sin\left(2\pi f\left(t - t_0\right) + \theta_d\right) + \frac{(\bar{u}-\hat{u})}{2} & t_0 + 1/f \leq t \leq t_0 + 1.5/f \\ \bar{u} & t > t_0 + 1.5/f \end{cases} \tag{4.4}$$

where f is also set to be 1, 2 and 4 Hz in separate trials and $\theta_d = \frac{\pi}{2}$.

The open-loop drift tests with input noise are performed based on input signal $u_o(t)$ having frequencies $f = 1$, 2 and 4 Hz. The following procedure is followed to examine the differential drift starting from the neutral state ψ_n in simulation:

1. Generate and save a uniformly-distributed random disturbance input $u_d(t)$ with cut-off frequency 15 Hz to the workspace of Matlab.
2. Invert N numerically and determine l for the given desired output $y_d = 1$ by interpolation.
3. Construct an input $u_o = u_l$ to drive the system to an initial state $\psi_n \approx \psi_n^l$.
4. Apply a constant offset at u_o, i.e. $u_o = l$ from $t = t_1$ to $t = t_1 + 2$ s.
5. Starting from $t = t_1 + 2$ s, inject 8 s of input noise at $u_d(t)$ scaled by different gains $K_n = 0.8 * i$ (where $i = 1, ...7$) for different trials.
6. At $t = t_1 + 10$ s, complete the test and store the output measurement.

For the other two different initial states ψ_a and ψ_d, the simulations are carried out in a similar procedure by changing step 2 and 3 to apply $u_o(t)$ as defined by Eq.(4.3) and (4.4) in order to drive the system to the other two initial states. Moreover in steps 4, 5 and 6, $t_1 = t_0 + 1.5/f$ for initial states ψ_a and ψ_d specifically.

In the experiments the implementation procedure is similar to that for the simulations with minor modification due to the un-modelled inertia of the bimorph beam. The parameter l in u_l for generating the initial state ψ_n and $\bar{u}$ for generating the initial states ψ_a and ψ_d are determined in experiments in order to give an output close to $y_d = 1$.

In order to generate the neutral state ψ_n in experiments, the locus $N(l)$ is determined from experimental data collected from the shape control system and inverted numerically to determine l for the given desired output $y_d = 1$ by interpolation. In order to generate ψ_a and ψ_d, $\bar{u}$ in Eq.(4.3) and (4.4) is determined during the first half period of the sine wave, which drives the system output into the range of $[y_d + \Delta y_l, y_d + \Delta y_h]$ in the first half period of the sine wave and keeps the system output in the range of $[y_d - 0.1, y_d + 0.1]$ between t_1 and t_1+2 in all experimental trials. The parameters Δy_l and Δy_h are determined experimentally for the input signals $u_o(t)$ with frequencies $f = 1$, 2 and 4 Hz separately, which are listed in Table 4.1.

Table 4.1: Threshold for generating the desired state ψ_a and ψ_d given $y_d = 1$

	ψ_a		ψ_d	
f (Hz)	Δy_l	Δy_h	Δy_l	Δy_h
1	-0.22	-0.14	0.14	0.22
2	-0.28	-0.22	0.22	0.28
4	-0.44	-0.38	0.38	0.44

4.3 Simulation Results

Open-loop drift tests are implemented in simulations in the presence of input noise. The influence of the initial states is investigated based on the Preisach model identified in Section 3.4 by using the FOD data sets collected from the bimorph piezoceramic actuator SS15. The simulation model developed in [7] is used to generate simulation results. The differential output drift as defined in [7] is applied to the outputs of the bimorph piezoceramic actuator, such that the effect of scaled input noise on different initial states can be compared quantitatively.

As explained at the beginning of this chapter, three different initial states ψ_n, ψ_a and ψ_d are investigated, each of which gives an output $y_d \approx 1$. The locations of those three initial states ψ_n, ψ_a and ψ_d are shown on the input-output graphs in Figure 4.6 through Figure 4.8 where a sinusoidal input is used to drive the hysteretic system to the desired state using the frequencies $f = 1$, 2, and 4 Hz. The major loop of the hysteresis becomes wider when the input signals are applied at higher frequency. Such a change in the hysteresis characteristics of a voltage-to-displacement relationship is likely caused by a combination of viscous-type effects and other dynamic effects which obviously become more pronounced when the input voltage frequency increases [55]. Moreover, in each figure the locus $N(l)$ and the major loop generated by an input voltage of different frequencies are also shown. In each case, the locus $N(l)$ together with y_- and y_+ is noted by a dash-dot line which is monotonic. The input range is discretized and neutral boundaries for each input in the discrete set are generated to drive the system to those boundaries. Then the output is determined based on the simulation model. Other missing points on locus $N(l)$ corresponding to the input not belonging to the input discrete set are determined by linear interpolation assuming continuity and fine enough quantization.

The test inputs as defined in the previous section are applied in simulation to the identified Preisach model of the bimorph actuator using the MATLAB code developed by the author of [7]. The simulated output starting from the three different initial states generated by input signals with different frequencies are presented in Figure 4.9 through Figure 4.11. The input noise has a gain of 1.6, i.e. the amplitude of the noise is 0.8 V. Even though the output signals are difficult to distinguish from each other, it can still be observed that the output is constant before the input noise injection starting from $t = 2$ s for each initial state of ψ_n, ψ_a and ψ_d. Moreover after the injection of input noise, the average output drifts different amounts based on the initial state. Such a difference becomes much more significant when the initial state is generated by an input signal with higher frequency. From Figure 4.9 through Figure 4.11, the differential output drift can be observed clearly. The mean value of the output between time $t = a$ and $t = b$ is noted by $\overline{y_{a,b}}$, then the differential output drift is defined as $\overline{y_{8,10}} - \overline{y_{0,2}}$. The differential output drift is

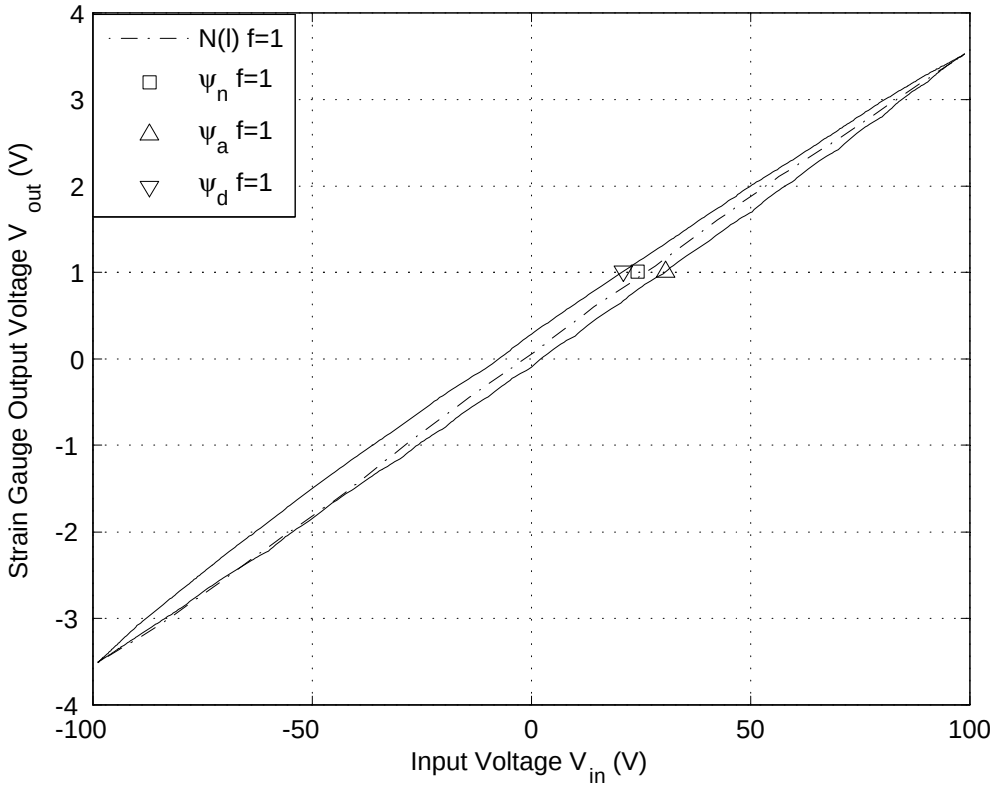

Figure 4.6: Major loop locus $N(l)$ and initial states for regulation test ($f = 1$ Hz simulated).

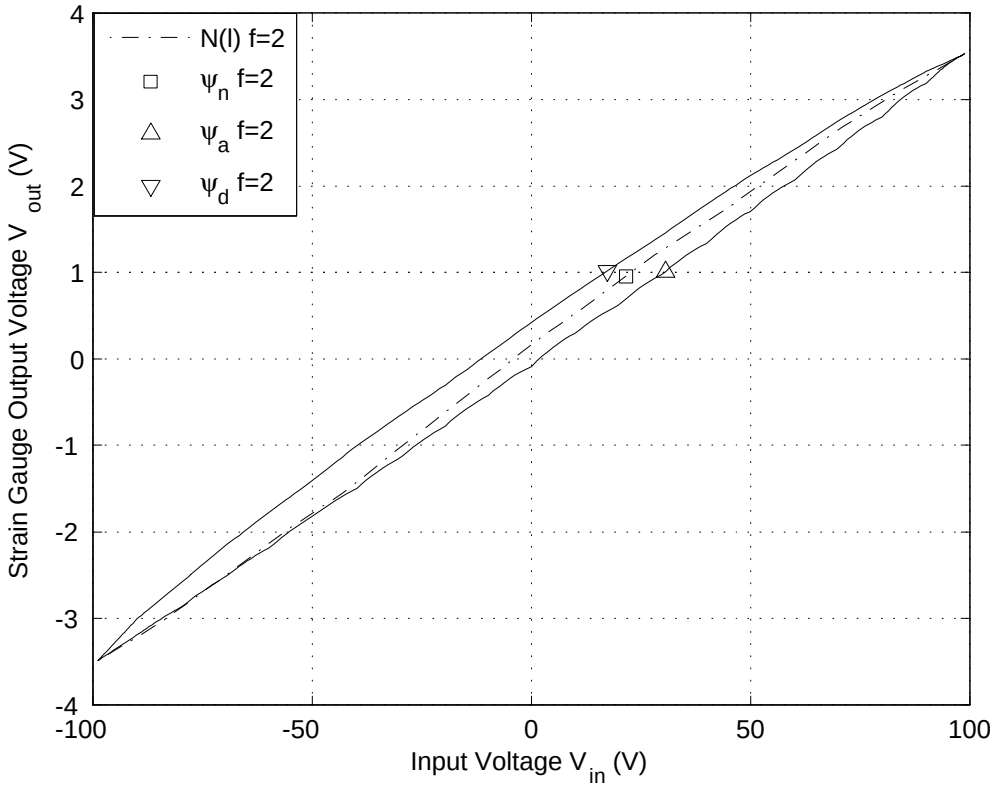

Figure 4.7: Major loop locus $N(l)$ and initial states for regulation test ($f = 2$ Hz simulated).

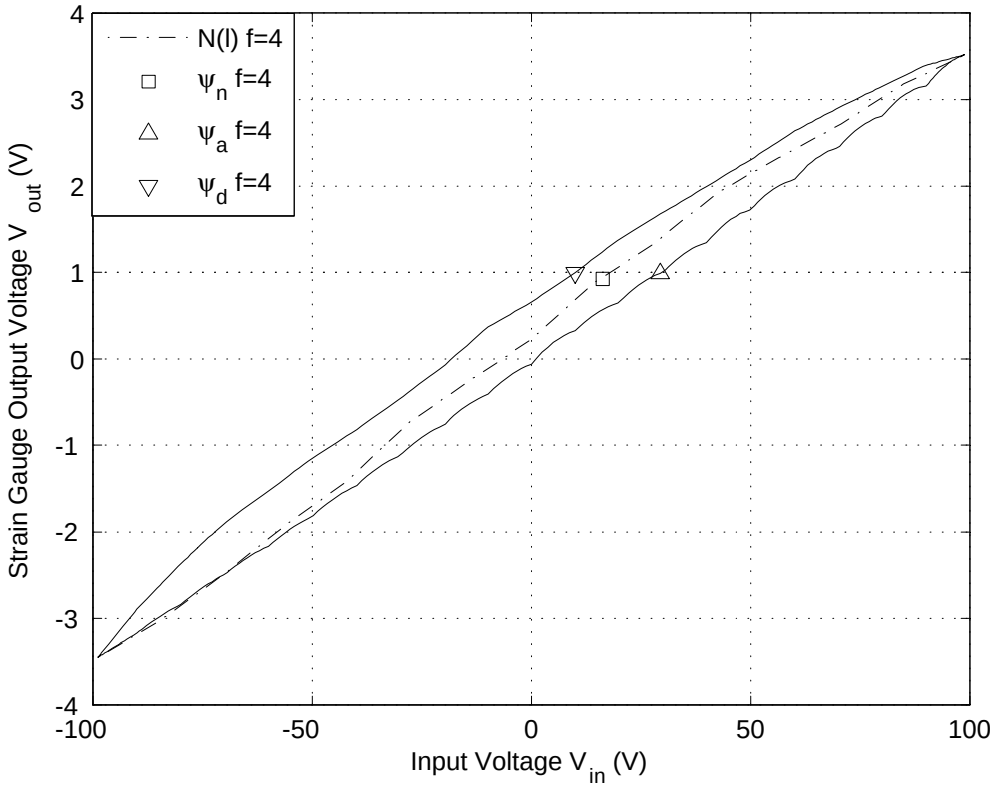

Figure 4.8: Major loop locus $N(l)$ and initial states for regulation test ($f = 4$ Hz simulated).

compared in open-loop regulation tests in the presence of input noise based on the different initial states where each initial state approximates the desired output $y_d = 1$.

Figure 4.12 shows the complete simulation results of the open-loop drift tests with input noise. Differential output drift is calculated and shown in the figure for the initial states ψ_n, ψ_a and ψ_d that have been generated by input signals with frequencies $f = 1$, 2, and 4 Hz. The injected input noise is scaled by gains $\{0.8, 1.6, 2.4, 3.2, 4.0, 5.6\}$. Figure 4.12 clearly shows the output drift based on the initial state ψ_n is less than those based on the other two initial states ψ_a and ψ_d. The simulated output also drifts in the opposite direction for initial states ψ_a and ψ_d. For example, $\overline{y_{8,10}} > \overline{y_{0,2}}$ for the initial state ψ_a while $\overline{y_{8,10}} < \overline{y_{0,2}}$ for the initial state ψ_d. When the noise gains are increased the differential output drift is also increased in magnitude for initial states ψ_a and ψ_d in most cases while such a tendency is not so clear for initial state ψ_n. Moreover, for initial non-neutral states ψ_a and ψ_d generated by higher frequencies, the differential output drift is more than those based on initial non-neutral states generated by lower frequency.

4.4 Experimental Results

The open-loop drift tests with input noise are also implemented in the shape control system. The complete experimental results are shown in Figure 4.13. There are two major similarities between the experimental and simulation results even though the experimental results shown do not appear exactly the same as simulation results. First, the differential output drift increases when the noise amplitude increases for non-neutral initial states. Second, the neutral state holds the best noise rejection property. The corresponding output voltage is also shown from Figure 4.14, which shows that the output is close to y_d within the range of ± 0.1 V. The results shown in Figure 4.13 are chosen from seven trials. During the chosen trial the output is closest to y_d before input noise injection comparing to the other six trials.

4.5 Discussion

From results in both simulations and experiments, it is clear that the differential output drift based on initial state ψ_n is lower than that based on the other two non-neutral states ψ_a and ψ_d. Now, this phenomenon will be explained based on the Preisach model. The Preisach boundaries of initial states ψ_n, ψ_a and ψ_d are shown in Figure 4.15. The state ψ_n is the reachable approximation of the unreachable neutral state ψ_n^l.

The intuitive reason for the state ψ_n holding optimal input noise rejection can be depicted in Figure 4.16 based on the Preisach model. The Preisach boundaries of initial states ψ_n ψ_a and ψ_d are presented in Figure 4.16 (a) (b) and (c) along with the area swept due to small positive and negative disturbances of the same amplitude $\bar{\xi}$. It is clearly shown in Figure 4.16 (a) that similar areas in the Preisach Plane P_r are swept by positive and negative disturbances with the same amplitude starting from initial state ψ_n. According to Proposition 1 stated in Section 2.4 on page 13, the output variation will be dependent on the integration of the weighting function μ over the area swept by the boundary caused by a monotonic change in input. In general the output variation will be similar when a similar area is swept by the Preisach boundary. Therefore, the output drift from the desired regulation point is much lower for a uniform distributed noise with zero mean based on the initial state ψ_n.

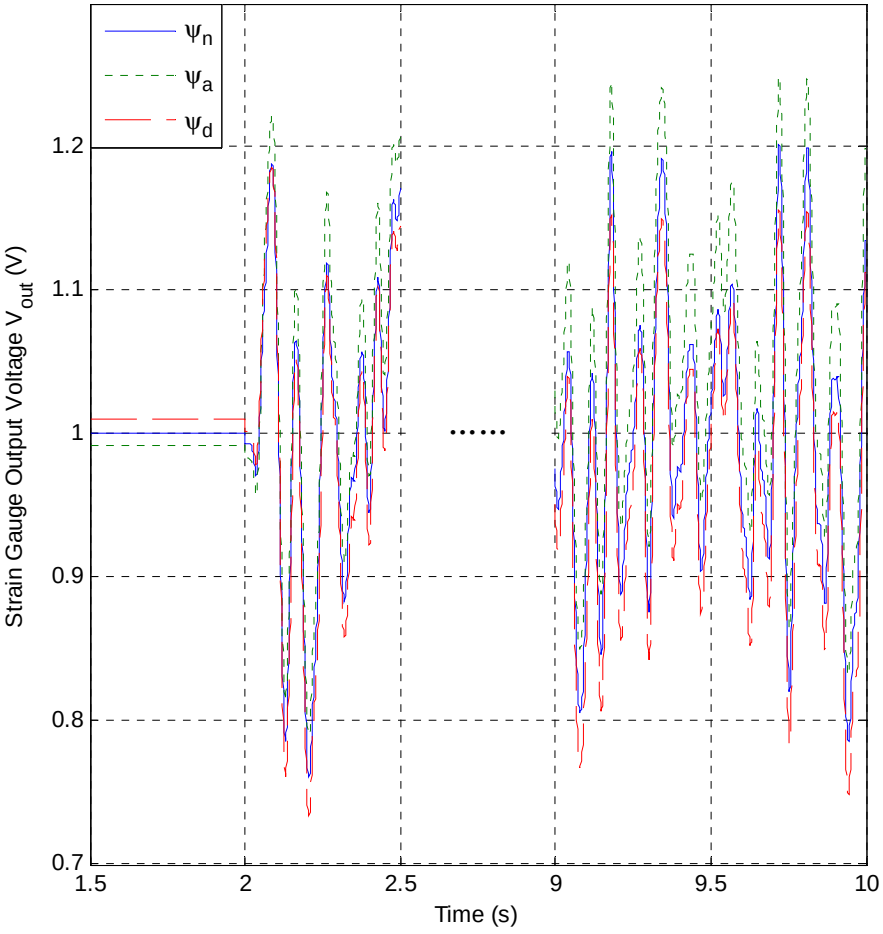

Figure 4.9: Simulated output response from initial states ψ_n, ψ_a and ψ_d generated by input signal at $f = 1$ Hz for a noise gain of 1.6.

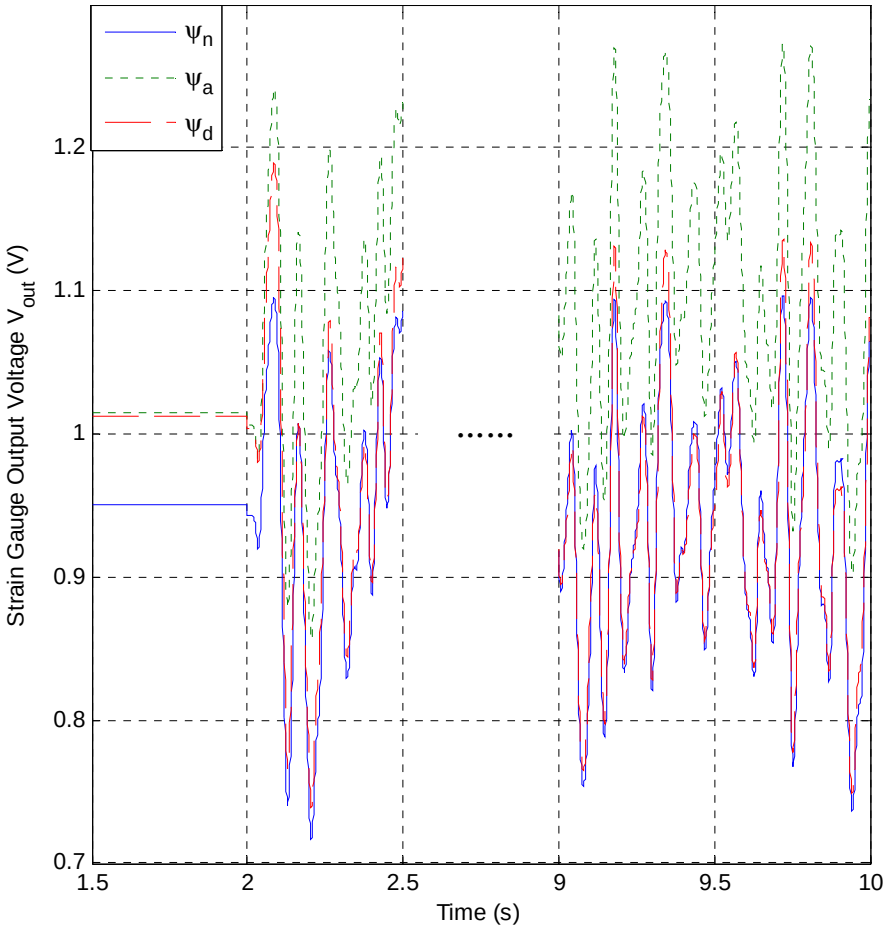

Figure 4.10: Simulated output response from initial states ψ_n, ψ_a and ψ_d generated by input signal at $f = 2$ Hz for a noise gain of 1.6.

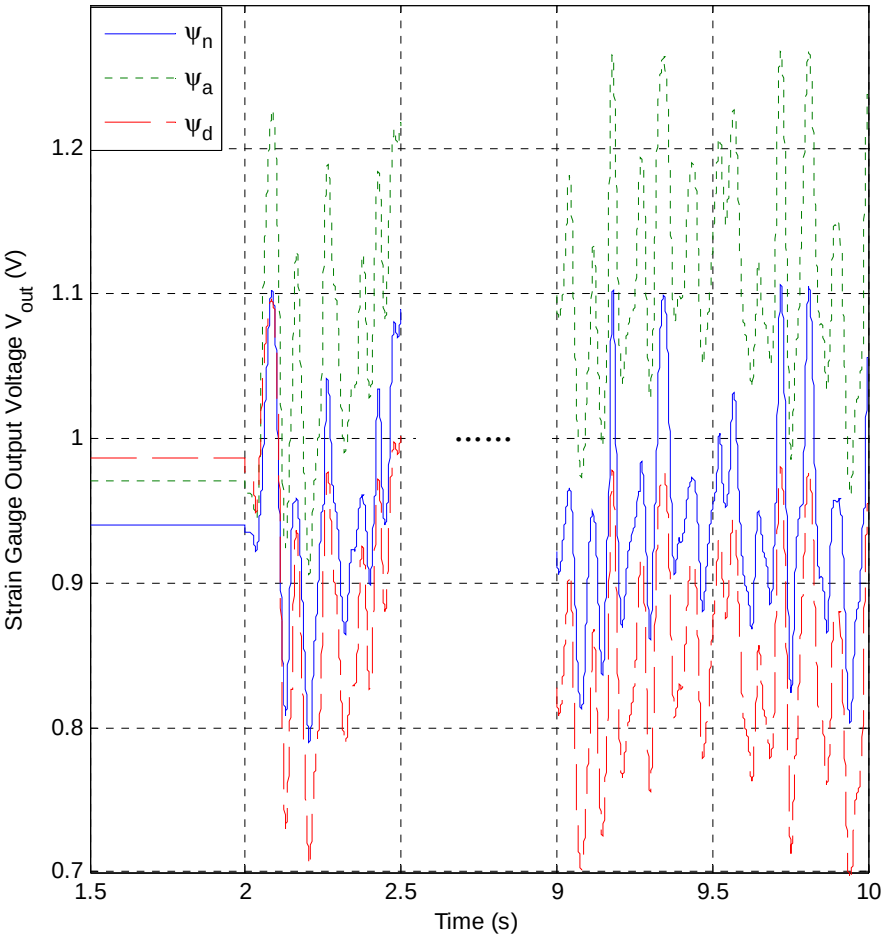

Figure 4.11: Simulated output response from initial states ψ_n, ψ_a and ψ_d generated by input signal at $f = 4$ Hz for a noise gain of 1.6.

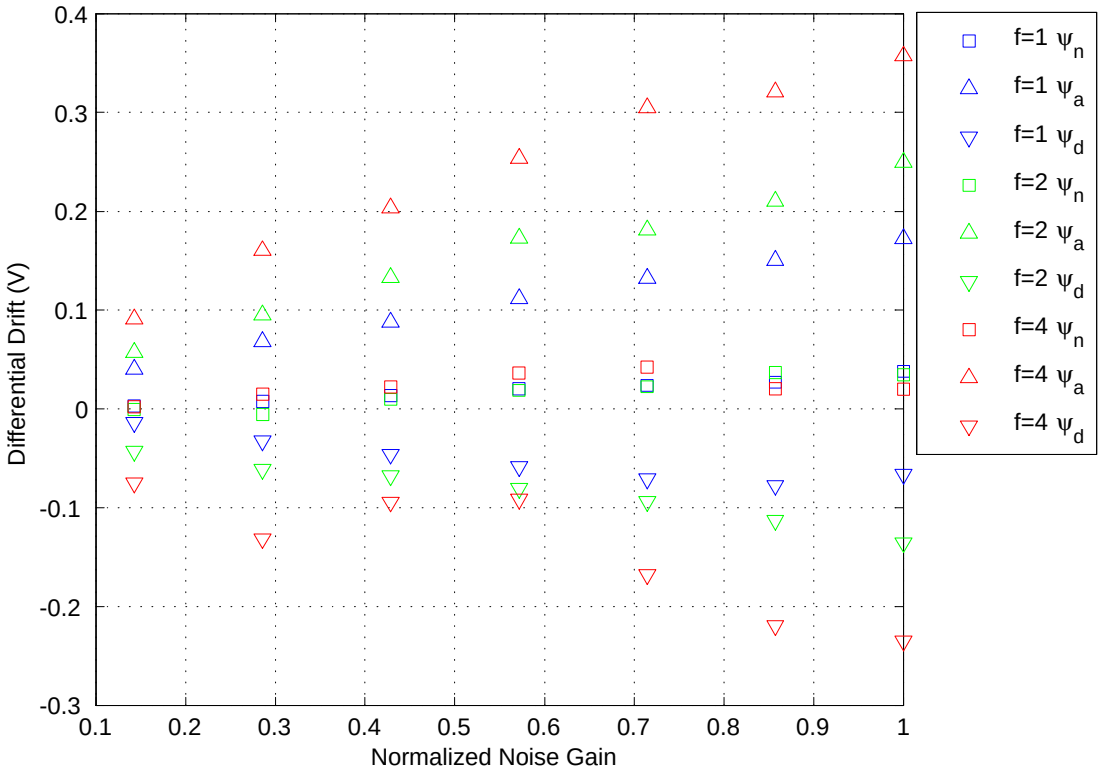

Figure 4.12: Open-loop differential drift for different noise gains and initial states generated by input signal with frequency f=1, 2 and 4 Hz (simulation).

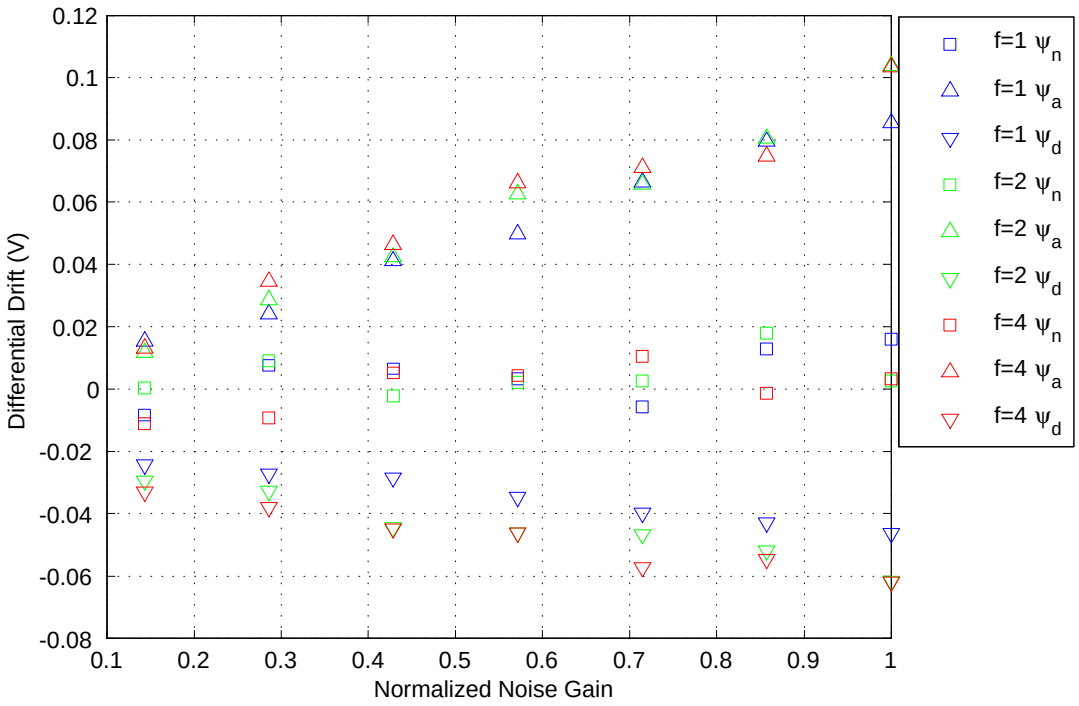

Figure 4.13: Open-Loop differential drift for different noise gains and initial states generated by input signal with frequency$f = 1$, 2 and 4 Hz (experiments).

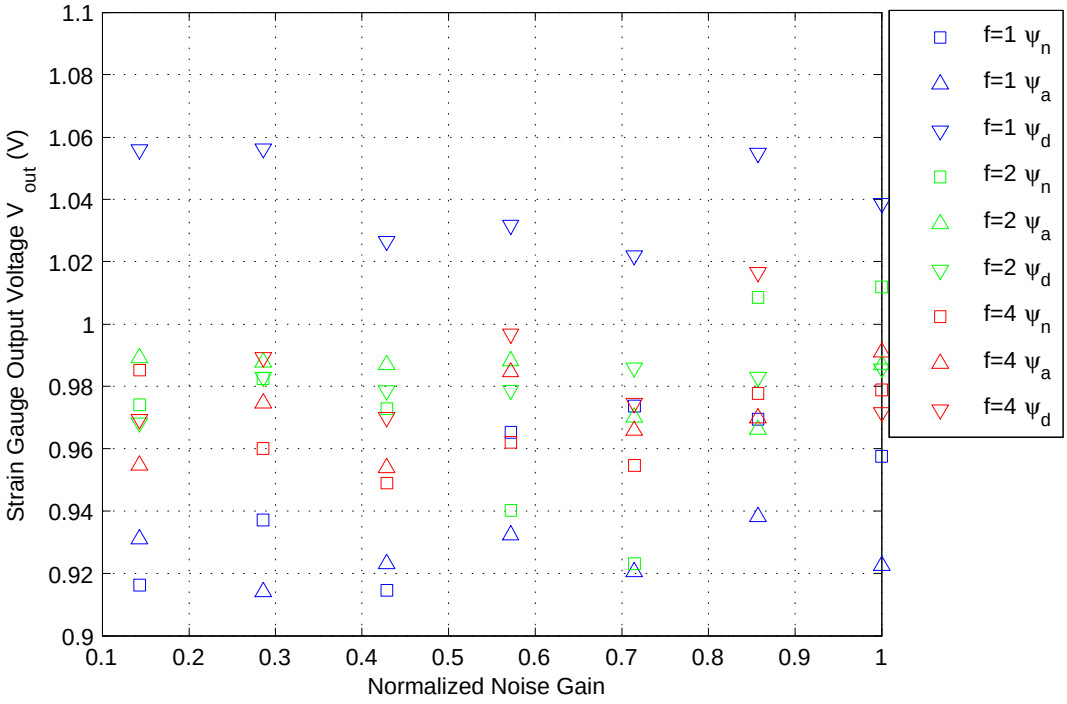

Figure 4.14: Output before input noise injection with different gains and initial states generated by input signal at $f = 1$, 2 and 4 Hz (experiments).

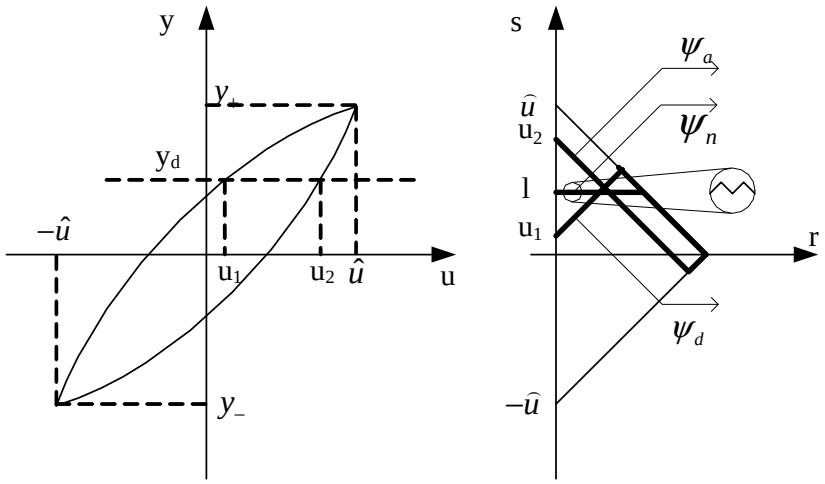

Figure 4.15: Initial states ψ_n ψ_a and ψ_d for open-loop drift tests about $y_d = 1$.

From Figure 4.16 (b), it can be observed that the area swept by the Preisach boundary caused by a positive disturbance is much larger than a negative disturbance. Generally speaking, the output variation is larger when a larger area is swept. Moreover, if $\mu > 0$ the output variation will have the same tendency as the input variation. Thus the differential output drifts are positive when a uniform distributed noise with zero mean is injected into the input signal. Similarly, the area swept by the Preisach boundary caused by a negative disturbance is much larger than a positive disturbance based on the initial state of ψ_d. Thus, the output drifts down after uniform distributed noise with zero mean is injected and starting from the initial state of ψ_d.

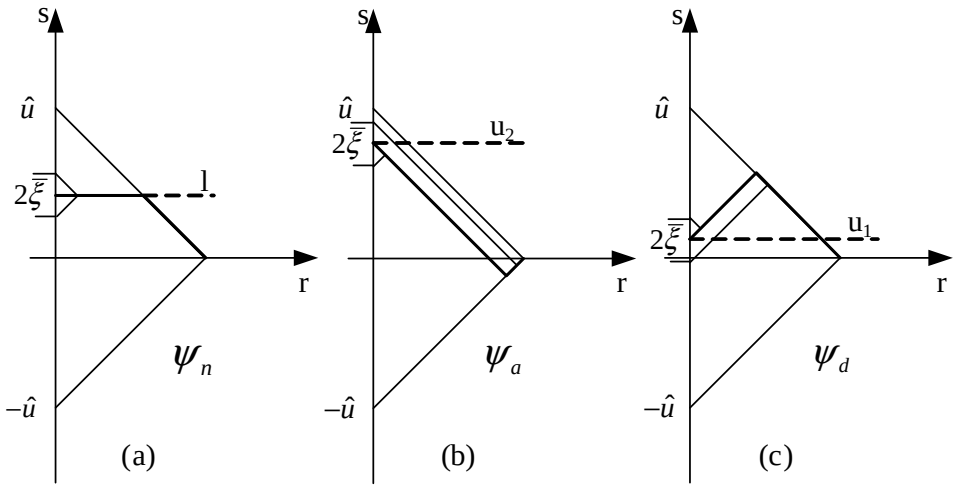

Figure 4.16: Preisach boundaries of initial states ψ_n, ψ_a, and ψ_d subjected to zero mean disturbance.

Chapter 5

Closed-Loop Regulation using PI Control

In order to achieve better performance during regulation tasks in the presence of noise and unmodelled system dynamics, a closed-loop controller is required. It is also prudent to investigate the influence of the initial state during closed-loop regulation. A closed-loop controller for regulation is expected to decrease or remove the drift observed in the open-loop tests in the presence of input noise regardless of the initial state prior to the injection of input noise. It is hypothesized in [7] that lower regulation control effort in closed-loop can be achieved if the system starts from the neutral state and this was demonstrated in simulation with a PI regulator and a Preisach model of a stacked actuator. The closed-loop regulation task for a hysteresis system is defined as follows.

Problem 2 (Closed-Loop Regulation Task) *Let $t_{rf} < t_{cf} < t_{nf}$ be three time instants, $\eta(t)$ be a uniformly distributed noise where $t \in (t_{cf}, t_{nf})$, and $\Psi_{eq}^{y_d}$ be the set of equivalent states for a given Preisach system with readout operator: $\Gamma_r(\Psi) \rightarrow Y$ and a desired output $y_d \in Y$. Suppose the input $u(t) = \bar{u}_d + u_c(t)$ when $t \in (t_{rf}, t_{cf})$, where $\bar{u}_d = u_d(t_r) = \psi_{eq}^{d}(t_r, 0) \in \Psi_{eq}^{y_d}$ and $u_c(t)$ is a PI regulator output. Suppose the input $u(t) = \bar{u}_d + u_c(t) + \eta(t)$ when $t \in (t_{cf}, t_{nf})$, where $\|\eta(t)\|_\infty = \xi$. When $t < t_r$, choose the initial state and design an input $u_d(t)$ to drive to that state, so that the control effort during closed-loop regulation in the presence of input noise is minimized.*

In this chapter, the control effort of a PI regulator is investigated in both simulations and experiments. In the first section the implementation procedure for the simulations and experiments is introduced. The simulation results based on the Preisach model of the bimorph piezoceramic actuator are presented in the second section while the experimental results collected from the shape control system are provided in the last section.

5.1 Implementation Procedure of Closed-loop Regulation in Simulation and Experiment

Figure 5.1 presents the closed-loop control system schematic employed to compare the closed-loop control effort when the initial states ψ_a ψ_d and ψ_n are achieved by u_o and the input noise u_d

with different gains is injected. Similar to the open-loop system schematic, D generates one of the initial states ψ_a, ψ_d and ψ_n given the desired output y_d without enabling the controller C by applying the input signal u_o with the frequencies $f = 1$, 2, and 4 Hz. The read-out operator Γ_r provides the system output y corresponding to a particular state generated by the total input $u_o + u_d + u_c$.

With the experimental system initially at ψ_a, a PI controller C is manually tuned to achieve a good response subject to a small step input disturbance. The analog controller output is provided as follows [56]:

$$u_c(t) = K_p e(t) + K_i \int_0^t e(\tau)\, d\tau \tag{5.1}$$

where $e(t) = y_d - y(t)$ is the controller input signal. Considering the controller required to be implemented in a discrete form, it is necessary to convert Eq. (5.1) into the equation in discrete format. The integral term is approximated to be the summation of all previous errors. Thus, the discretized PI controller is shown as below [56]:

$$u_c(k) = K_p e(k) + K_i T_s \sum e(k) \tag{5.2}$$

where $e(k) = y_d - y(k)$ and T_s is the sampling time interval. In both the simulation and experiment the sampling time T_s is set to 0.001 s when the input signal is set to 1 and 2 Hz in order to initialize the system to a particular initial state such as ψ_a, ψ_d and ψ_n given a desired output $y_d = 1$ V; the sampling time is set to 0.0005 s when the initialization input signal is set to 4 Hz in both the simulation and experiment. The simulation results are obtained via the following procedure:

1. Apply $u_o(t)$ $(t \leq t_1)$ to achieve each of the initial states ψ_a, ψ_d and ψ_n for a desired output voltage $y_d = 1$ V, i.e. $\Gamma_r(\psi_a) = \Gamma_r(\psi_d) = \Gamma_r(\psi_n) = y_d$; this is the same as the open-loop test.

2. Starting from $t = t_1$, apply a constant offset $u_o(t_1)$ to keep the system in the desired state given the desired output voltage.

3. Starting from $t = t_1 + 1$ s, enable the PI regulator by closing switch S as shown in Figure 5.1 and superimpose the controller output $u_c(t)$ on the constant offset $u_o(t_1)$

4. Starting from $t = t_1 + 2$ s, inject the 8 s scaled input noise u_d, i.e. after $t = t_1 + 10$, $u_d = 0$.

5. At $t = t_1 + 12$ s, complete the test and store the experimental data.

The implementation procedure for the experiments is similar to that for the simulations. However, the input to the PI controller is obtained by the average error, i.e. $\Delta y = y_d - y$, collected in the previous 0.025 s in order to remove the effect of measurement noise in the experimental setup.

This procedure is followed for each of the initial states and for 7 noise gains K_n, i.e. $K_n = 0.8 * i$ (where $i = 1, ...7$). In order to compare the control effort of the PI regulator starting from the different initial states in the presence of the input noise, the 2-norm of the control effort n_c is the metric employed and is calculated using the formula:

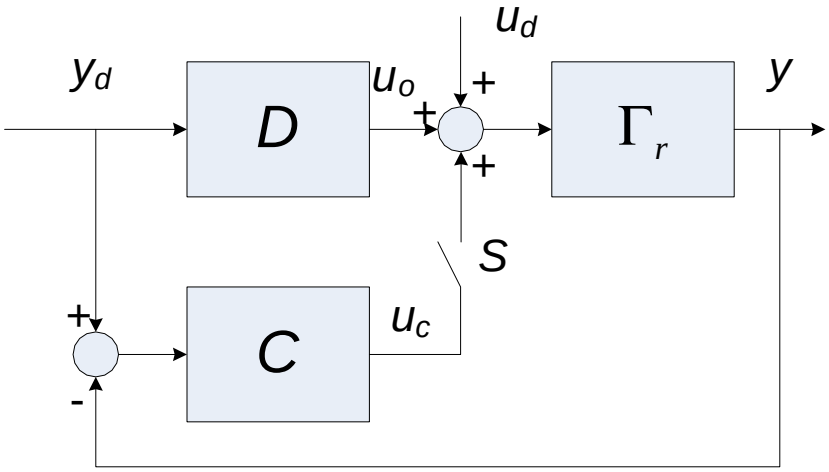

Figure 5.1: Control system schematic employed to compare performance when different initial states and input noise are applied.

$$n_c = \|u_{cn}(t) - \bar{u}_c\|_2 \tag{5.3}$$

where $u_{cn}(t) = u_c(t)$ $t \in (t_1 + 2, t_1 + 10)$ and $\bar{u}_c$ is the mean value of $u_c(t)$ $t \in (t_1 + 1.5, t_1 + 2)$. Only the control effort to overcome the differential drift due to the injection of the input noise is taken into account in n_c. The simulation and experimental results are presented in the following two sections.

5.2 Simulation Results

The closed-loop regulation tests are implemented in simulation based on the same Preisach model and simulation model used in the open-loop tests except with the addition of proportional-integral (PI) feedback. The simulated closed-loop output for a noise gain of 1.6 is shown in Figure 5.2 through Figure 5.4 for each initial state generated by an oscillatory input with frequencies 1, 2 and 4 Hz respectively. It can be observed from these three figures that the PI regulator is able to drive the system to the desired output $y_d = 1$ regardless of the initial states and the input signals frequencies without the presence of the input noise. The difference between the desired output and simulated output can be observed from $t = 0$ to 1 s when the controller is disabled. Such an error is caused by the quantization of the simulated Preisach model. Starting from $t = 1$ s, the controller is enabled and drives the system to the desired output, i.e. $y_d = 1$ V. However, the controller is not able to maintain the system at the desired output when the input noise is injected from $t = 2$ to 10 s. When the input noise ends at $t = 10$ s, the controller drives the system to the desired output $y_d = 1$ V again. Therefore, we can conclude that the closed-loop regulator is able to eliminate the output drift observed in the open-loop tests.

The 2-norm of control effort n_c is calculated based on Eq. (5.3), where the timing information is given, and shown in Figure 5.5 through Figure 5.7 for input signals with different frequencies

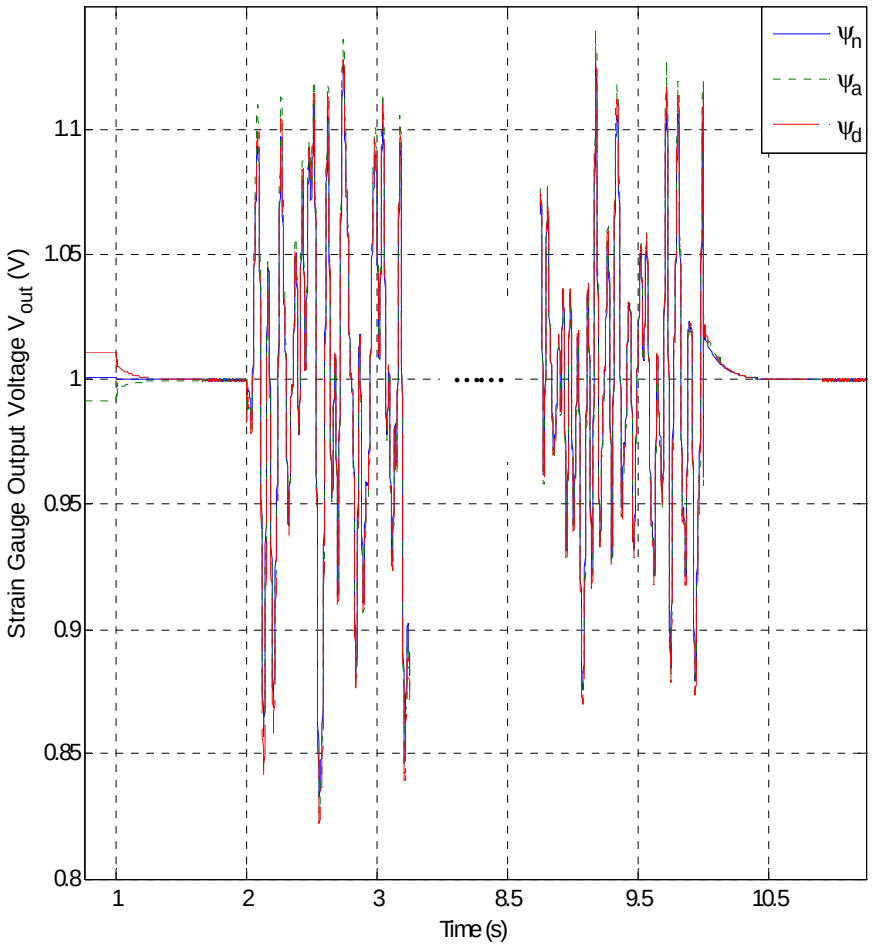

Figure 5.2: Closed-loop simulated output at a noise gain of 1.6 and an input signal with frequency $f = 1$ Hz.

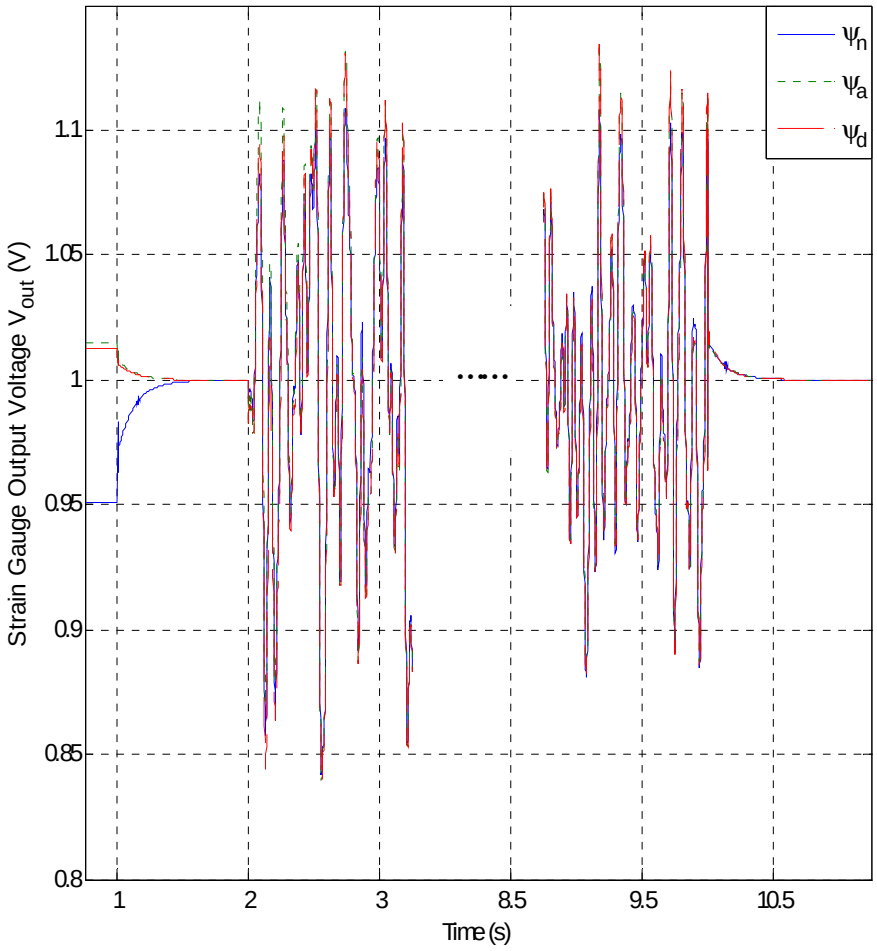

Figure 5.3: Closed-loop simulated output at a noise gain of 1.6 and an input signal with frequency $f = 2$ Hz.

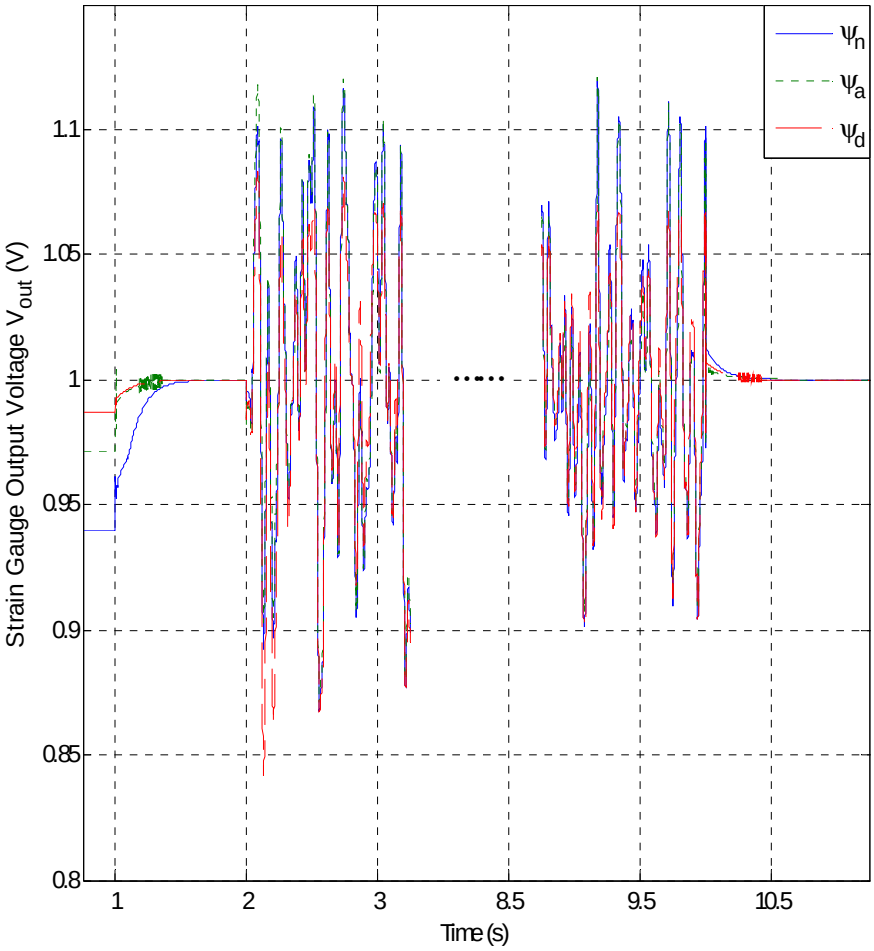

Figure 5.4: Closed-loop simulated output at a noise gain of 1.6 and an input signal with frequency $f = 4$ Hz.

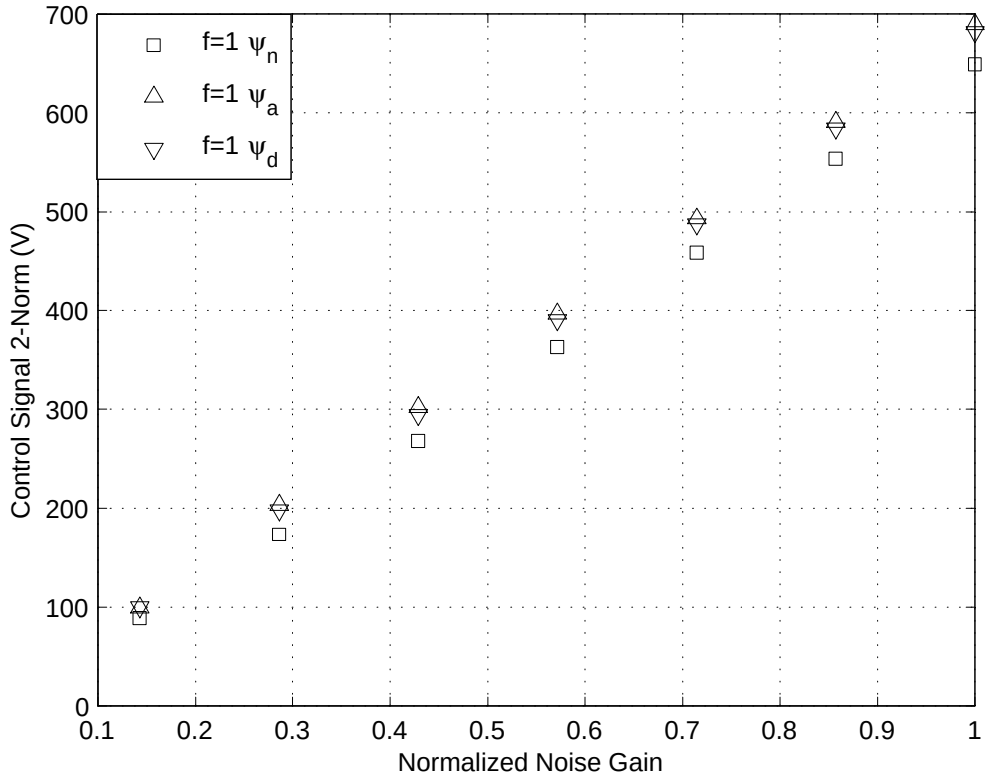

Figure 5.5: Simulated closed-loop control effort for different noise gains and initial states with the initialization input signal with frequency $f = 1$ Hz.

applied to achieve the initial states. When the initialization input signal has frequency $f = 1$ and 2 Hz, the control effort n_c obtained in the regulation test starting from the initial state ψ_n is smaller than the other two initial states ψ_a and ψ_d, which is more obvious when the noise gain increases. Moreover, for the initialization input signal at frequency $f = 1$ Hz, approximately the same control effort is required in the regulation task for the initial states ψ_a and ψ_d on opposite branches of the major loop since the hysteresis loop is approximately symmetric at $y_d = 1$ V. However, the control effort shows increased difference between the initial states ψ_a and ψ_d when the initialization input signal has a frequency of $f = 2$ Hz. This is probably because when the frequency of the input signal for initialization increases, the branches of the major loop becomes less symmetric. When the input signal frequency increases to 4 Hz, the better regulating performance of starting from the neutral state ψ_n disappears when the noise gain is increased to more than 4.0; this may be caused by limitations of the Preisach model of a piezo when the input signal is at a high frequency.

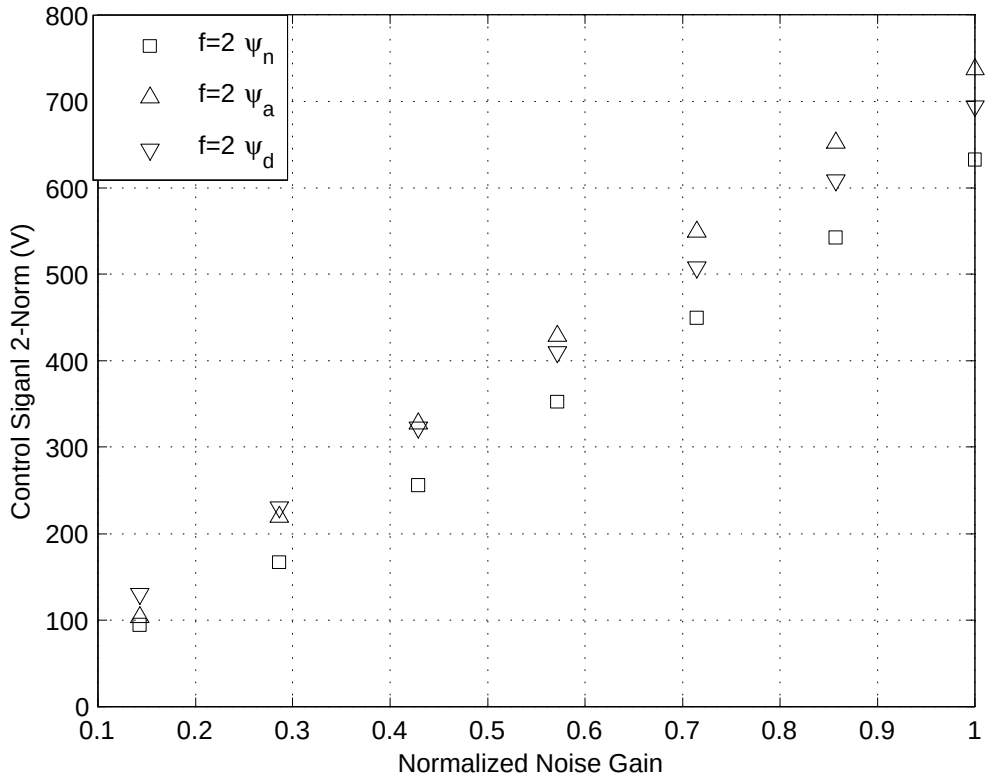

Figure 5.6: Simulated closed-loop control effort for different noise gains and initial states with the initialization input signal with frequency $f = 2$ Hz.

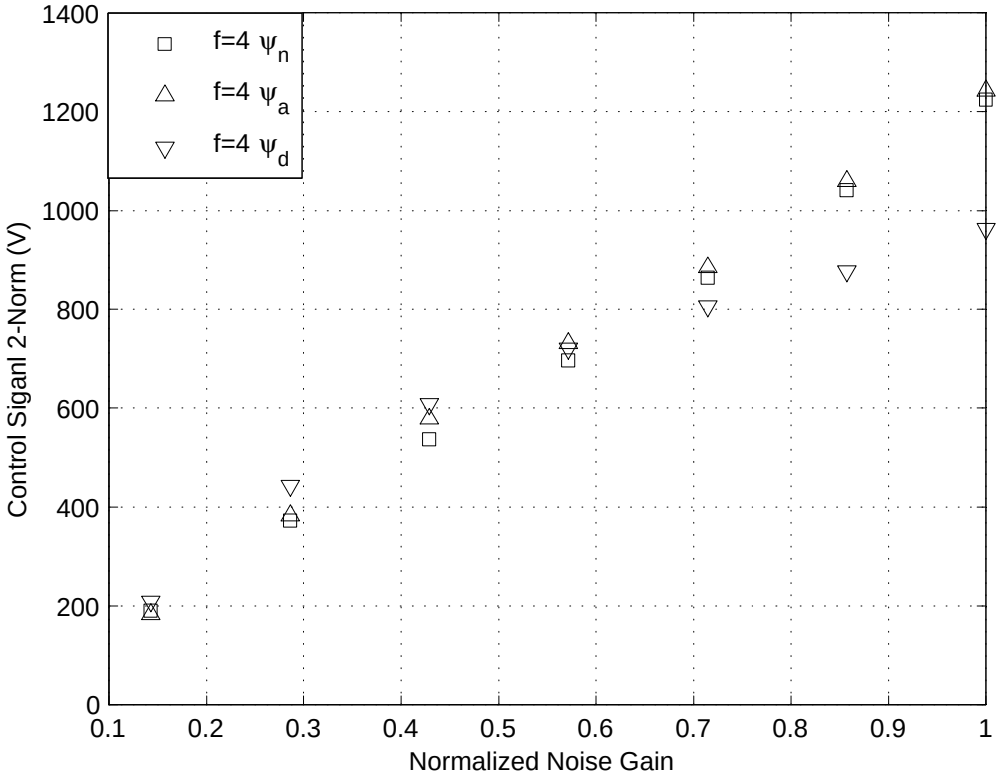

Figure 5.7: Simulated closed-loop control effort for different noise gains and initial states with the initialization input signal with frequency $f = 4$ Hz.

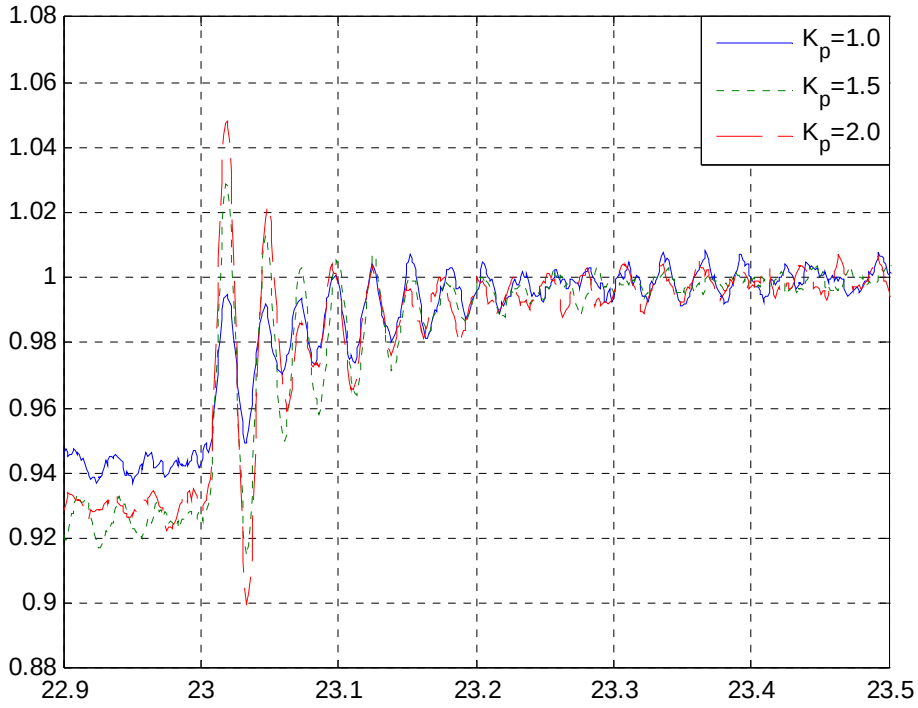

Figure 5.8: Experimental output of closed-loop regulation control for different K_p at initialization state ψ_a generated by an input signal at 1 Hz.

5.3 Experimental Results

The experimental results of the closed-loop regulation tests are presented in this section. First, the gain tuning results based on the initial state ψ_a are shown, then the control efforts n_c calculated from the data collected from experiments are shown.

The gain tuning results are based on the mean value of five trials for each gain setup. When the integral gain K_i is nominally set to be 30, the proportional gain K_p is set to be 1.0, 1.5 and 2.0 separately and the results are shown in Figure 5.8. With higher K_p, the oscillation is more obvious while with smaller K_p the output tends to achieve steady state slower. Thus, K_p is selected to be 1.5 ,and trials are run where $K_i = 20$, 30, and 40, and the results are shown in Figure 5.9. With higher K_i, the output approaches the desired output quicker, but there exists oscillation after achieving steady state. Thus, K_i is set to 30.

In order to evaluate the effect of the different initial states, the 2-norm of the control effort n_c is examined for each of the initial states as $n_c(\psi_n)$ $n_c(\psi_a)$ and $n_c(\psi_d)$. The differences of the 2-norm of control effort between initial states ψ_a and ψ_n, i.e. $n_c(\psi_a) - n_c(\psi_n)$, are shown as upward-pointing triangles in Figure 5.10 through 5.12 for the various noise gains and the input

Figure 5.9: Experimental output of closed-loop regulation control for different K_i at initialization state ψ_a generated by an input signal at 1 Hz.

signals frequencies $f = 1$, 2 and 4 Hz. In addition, the differences of n_c between initial states ψ_d and ψ_n, i.e. $n_c(\psi_a) - n_c(\psi_n)$, are shown as downward-pointing triangles in the same figures for each case. The results shown here are based on the mean value of seven trials and the experimental data are collected from the shape control system. It can be seen in Figure 5.10 through 5.12 that most of the differences are positive except for one data point in Figure 5.12, which means that the control efforts during regulation starting from the initial state ψ_n are smaller than the other two initial states ψ_a and ψ_d even though the control effort differences are not increasing when the input noise gains increase. The differences of the 2-norm of control effort n_c between the non-neutral states (ψ_a and ψ_d) and the neutral ψ_n over the control effort n_c starting from the neutral state ψ_n, i.e. $\frac{[n_c(\psi_a)-n_c(\psi_n)]}{n_c(\psi_n)} \times 100\%$ and $\frac{[n_c(\psi_d)-n_c(\psi_n)]}{n_c(\psi_n)} \times 100\%$ are listed in Table 5.1 in percentages for different noise gains and input signals with different frequencies. It is shown that, even though it is better to start from the initial state ψ_n, the difference of the control effort between the non-neutral states and the neutral state is not significant.

Table 5.1: Percentage of control effort

f (Hz)	1	2	4	1	2	4
Normalized Noise Gain	$\frac{[n_c(\psi_a)-n_c(\psi_n)]}{n_c(\psi_n)}$			$\frac{[n_c(\psi_d)-n_c(\psi_n)]}{n_c(\psi_n)}$		
0.1429	0.2277	1.9916	0.2666	6.6523	6.3656	18.0776
0.2857	1.1494	0.7452	2.2912	2.3129	2.8210	3.3733
0.4286	2.6548	1.7425	-0.0032	1.9575	1.5881	2.0138
0.5714	1.2536	1.6094	0.9816	1.9920	0.8368	1.1421
0.7143	1.4988	1.2737	1.1755	1.3567	1.2008	1.0495
0.8571	1.5130	1.2553	1.4559	1.4250	1.0649	0.7772
1	2.0443	1.3737	1.2434	1.4365	0.7818	1.5092

Since noise also affects the control effort during the experiments, the experimental results are not exactly as we expect: the control effort is not monotonically increasing when the input noise gains increase; the control effort starting from the initial states ψ_a and ψ_d are not the same as each other even when the input signal is at 1 Hz to generate the initial states. However, the benefit of starting from the initial state ψ_n in regulation tasks is demonstrated experimentally with results collected from the shape control system.

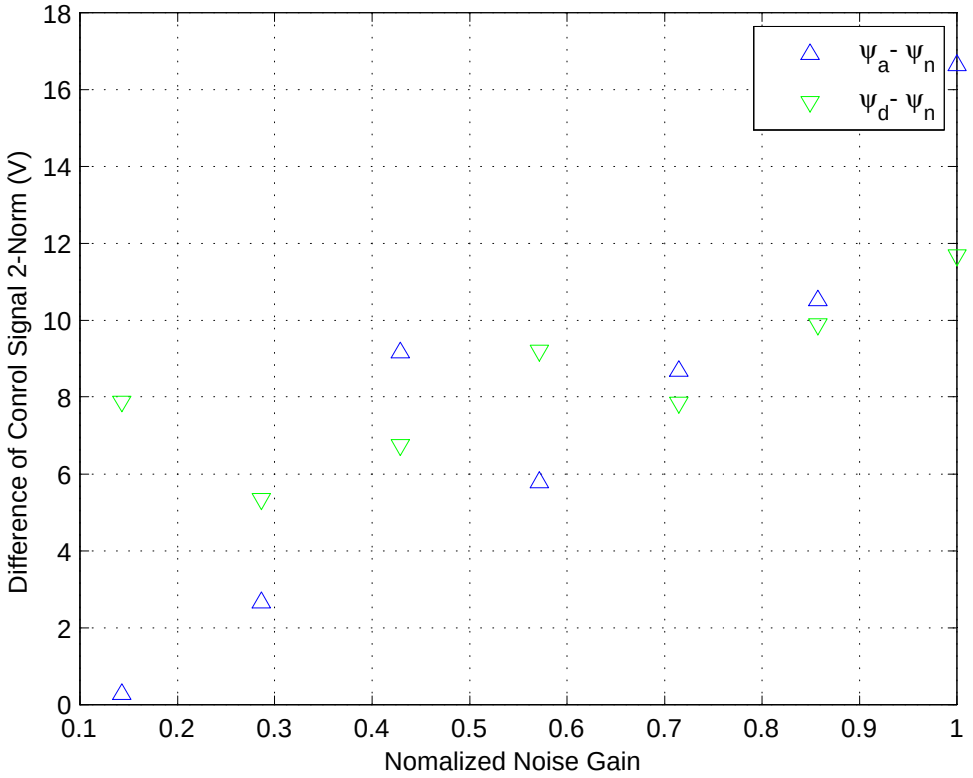

Figure 5.10: Experimental difference of control signal 2-norm for different noise gains and initial states based on initialization input signal with frequency $f = 1$ Hz.

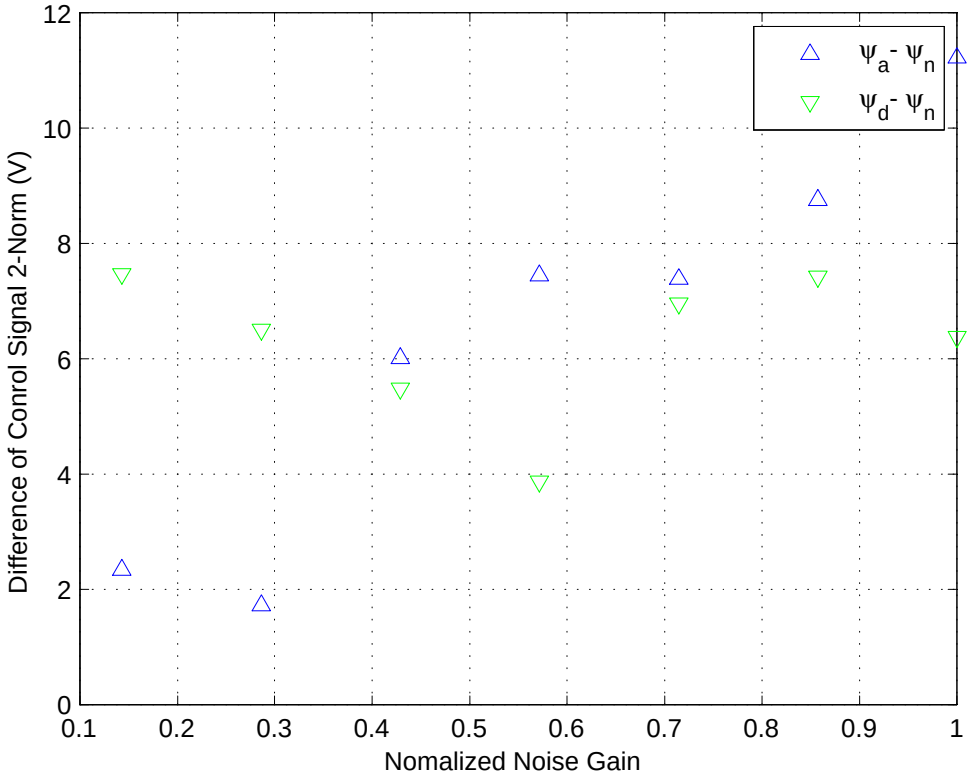

Figure 5.11: Experimental difference of control signal 2-norm for different noise gains and initial states based on initialization input signal with frequency $f = 2$ Hz.

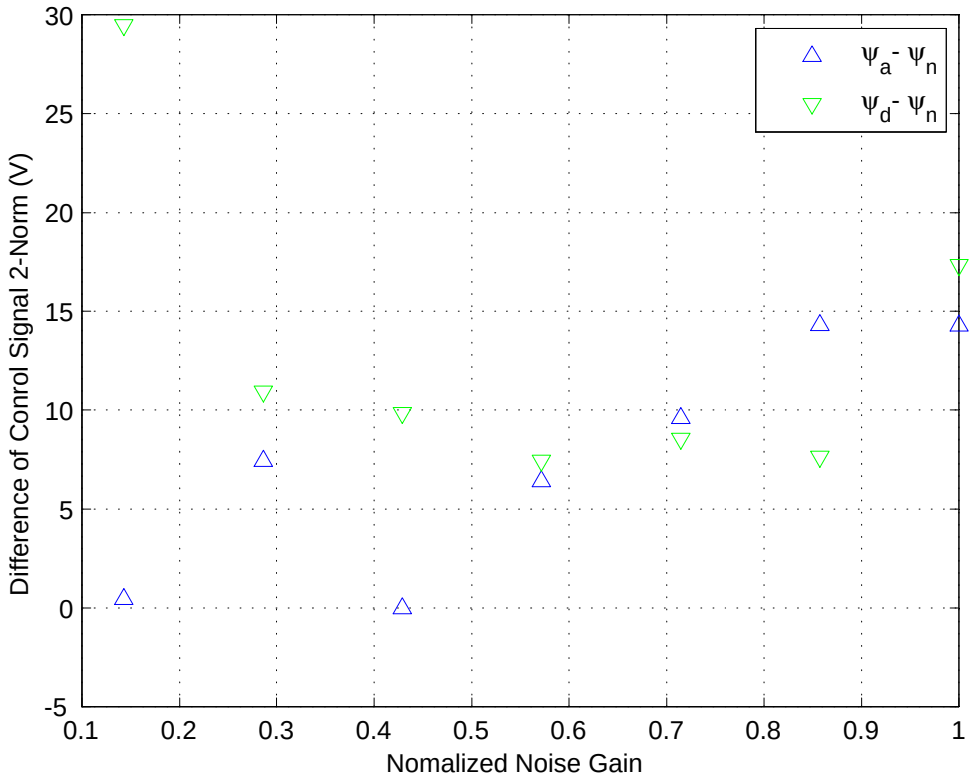

Figure 5.12: Experimental difference of control signal 2-norm for different noise gains and initial states based on initialization input signal with frequency $f = 4$ Hz.

Chapter 6

Conclusions and Future Work

In this thesis, a study has been conducted to investigate the effect of the initial state of a hysteretic system with Preisach representation in a regulation task when there is input noise.

6.1 Conclusions

The hysteresis inherent in piezoceramics leads to the limitation in their precision applications. However, given a desired output, the existence of multi-states also provides one more degree of freedom for the regulation design of those systems with memory, which is different from the regulation design for memory-less systems.

The Preisach model is identified in this work to describe the hysteretic relationship between the strain gauge output voltage and the high input voltage of the shape control system studied in this thesis. The Preisach model is chosen due to its general structure and ability to model hysteresis.

- The results from the representation tests demonstrate the classical Preisach model is sufficient to describe hysteresis with reasonable error when the input signal is at frequency $f = 1$, 2, and 4 Hz.

From the wiping-out tests, the error of the maximum magnitude over the whole output range is about 2.33% 4.51% and 9.23% when the input signal is at $f = 1$, 2, and 4 Hz. From the CML tests, the error of the maximum magnitude over the whole output range is about 2.05% 4.16% and 7.38% for the input signals at $f = 1$, 2, and 4 Hz. From the comparison between the experimental and simulated FOD data, it is found that the error of the maximum magnitude over the whole output range is about 2.42% 4.52% and 8.69% at $f = 1$, 2, and 4 Hz. However, the modelling error becomes larger when the high input voltage has a higher frequency based on the experimental results. Since the classical Preisach model is intended for describing the static hysteresis while the hysteresis inherent in piezoceramic actuator is more dynamic when the frequencies of the input signals increase, such an increased modelling error is expected. Further

more, since the mechanical dynamics of the bimorphs have not been incorporated into the model, this represents another source of the increased modelling error.

The open-loop drift tests are performed in both simulations and experiments based on the shape control system. The better regulating performance of the neutral state is explained intuitively based on the Preisach model.

- The simulation and experimental results clearly show that the open-loop differential output due to input noise is less when the system starts from the neutral state ψ_n as compared to the other two initial states ψ_a and ψ_d on the ascending and descending branches of the major loop.
- The simulation and experimental results also demonstrate that the open-loop differential drift increases when the input noise gain increases and the system starts from the initial states ψ_a and ψ_d, while such a tendency for the initial state ψ_n is not so obvious.
- When the initial state is generated by an input voltage with a higher frequency, the difference of the differential output between starting from the neutral states and the non-neutral states becomes larger according to the simulation results. However, such a trend is not clear according to the experimental results when the frequency of the input signal increases.

The closed-loop regulation tests are also applied in both simulations and experiments. The same input noise signal injected in the open-loop tests is used here. A traditional PI controller is tuned based on the initial state ψ_a. The 2-norm of the control effort due to the input noise injection is compared when the system starts from the different initial states ψ_n ψ_a and ψ_d.

- The simulation results demonstrate that the system requires the least control effort when it is initialized at the neutral state as compared to the other two initial states ψ_a and ψ_d, except when the initial states are generated by an input signal with a higher frequency up to 4 Hz.
- The experimental results indicate that the shape control system requires the least control effort when it starts from the neutral state ψ_n under all noise and frequency conditions tested as compared to the other two initial states.

Since both simulation and experiments have shown advantages by starting from the neutral states, it may be possible to show this analytically. Traditionally this could be approached by taking derivatives of the model used, in this case, the Preisach model. Although a conventional derivative does not exist for this model, it is possible to take sub-derivatives for this purpose, and this is provided in Appendix A.

6.2 Future Work

In order to continue the work of investigating the better regulating performance of the neutral state, the following tasks are recommended:

- Identify the dynamic Preisach model at frequencies over a broader spectrum. Implement open-loop noise rejection test and closed-loop regulation test at frequencies over the broader spectrum in both simulations and experiments.
- Theoretically, the better noise tolerance of the neutral state may be proved by minimizing the output variation subject to a noisy input signal based on the Preisach model. A derivative based on the Preisach model (see Appendix A) may be incorporated into optimization routines, such that for a given output setpoint, the output variation due to noise in the input signal is minimized by designing an optimal initial state.
- Design and implement more sophisticated control methodologies such as robust control [57], fuzzy logic adaptive control [58] and neuro-adaptive control [59] to investigate the effects of different initial states. Investigate the response to disturbance or input noise in closed-loop using the Preisach model to determine initial state given an output. It is expected that the control effort is minimum at neutral state and neutral state is robust to disturbance and noise regardless of the type of controller.
- Explore the effect of initial states based on a dynamic Preisach model. Hopefully the extension and the application of a dynamic model to the shape control unit SS15 would remove some of the uncertainties around the frequency-dependence which is observed in this thesis.
- Investigate the influence of initial states within the hysteresis in terms of a dynamic tracking problem. Explore the possibility of tracking the state along the neutral locus, as the desired output varies in the range of the hysteresis. The extension is non-trivial since the current model requires wide swings of input (and therefore output) in order to drive the system to the neutral locus once it leaves. However, there may be value in studying these regulation-specific results for the understanding of the tracking problem in future.

Appendix A

Preisach Model Derivative

In this appendix, the derivative of the Preisach model is determined. Before computing the derivative, we introduce a reduced memory sequence as a useful tool. When the input keeps its direction, the derivative can be easily defined in a conventional sense. However, the derivative of a hysteresis loop does not even exist, in a traditional sense, at input reversals. Thus, the generalized derivative of the Preisach model is developed when the input reverses its direction.

A.1 Reduced Memory Sequence

A branch appears in the hysteresis loop when the input switches direction at the input extrema. Generally the output of a static hysteresis is dependent on the current input value and all the past input extrema. The effect of these previous input extrema are stored in a hysteretic loop output, and the set of past extrema is used to build a memory sequence [10]. The wiping-out property of the Preisach model implies, in particular, that the output is determined only by a specific subset of the memory sequence. Mayergoyz referred to the subset as dominant input extrema [9] and Visintin referred it as the reduced memory sequence, abbreviating to be RMS [10]. The latter terminology is used in the thesis.

As described in the previous section, the wiping-out property states that any input maximum which is larger than previous maxima will wiping-out the memory of those maxima and any input minimum which is smaller than previous minima will also wiping-out those minima. For a given time τ, only particular past extrema remain and influence the output. Those extrema build a corresponding set of input maxima and minima. In the set, the maxima decrease in magnitude sequentially while the minima increase until the two series converge at $u(t)$.

Both [10] and [9] have examples of the construction of the reduced memory sequence associated with an input. The following construction is from [10].

For any input $u \in U(-\infty, T]$ and any $\tau \leq T$, set

$$\begin{aligned} s_0 &= 0 \\ \eta &= \max_{t \in (-\infty, \tau]} |u(t)| \end{aligned}$$

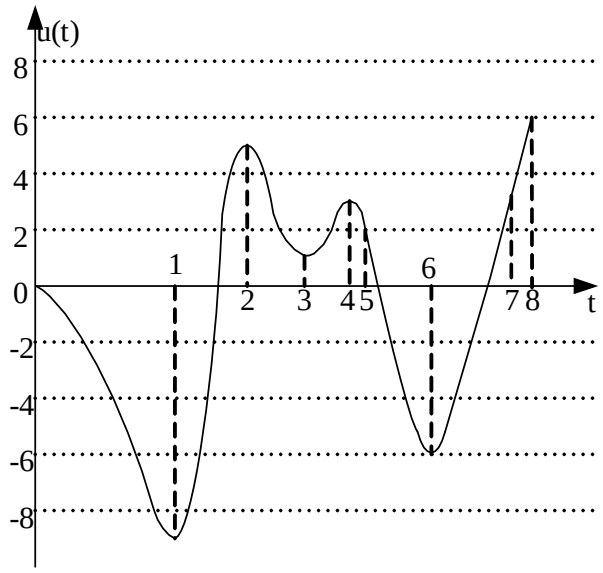

i	$s(u,t_i)$
1	{-9}
2	{-9, 5}
3	{-9, 5, 1}
4	{-9, 5, 1, 3}
5	{-9, 5, 1, 3, 2}
6	{-9, 5, -6}
7	{-9, 5, -6, 3}
8	{-9, 6}

Figure A.1: Input $u(t)$ and correponding RMS.

and let

$$t_1 = \max\{t \in (-\infty, \tau] \,|\, |u(t)| = \eta\}$$

Then the elements s_i $(i = 1, 2, ...)$ of the reduced memory sequence $s = \{s_i\}$ where $i \geq 1$ can be defined as follows:

$$\begin{aligned}
i = 1 \qquad &: \qquad s_1 = u(t_1) \\
s_{i-1} < s_{i-2} &: \qquad s_i = \max_{t \in (t_{i-1}, \tau]} u(t) \\
&\qquad\quad t_i = \max\{t \in (t_{i-1}, \tau] \,|\, u(t) = s_i\} \\
s_{i-1} > s_{i-2} &: \qquad s_i = \min_{t \in (t_{i-1}, \tau]} u(t) \\
&\qquad\quad t_i = \max\{t \in (t_{i-1}, \tau] \,|\, u(t) = s_i\}
\end{aligned}$$

When $t_i = \tau$, the sequence is terminated.

The elements in RMS vary with respect to time. For instance, the input $u(t)$ and its RMS corresponding to different time is shown in Figure A.1. The Preisach boundaries at different instances in time is also shown in Figure A.2, from which it is clearly shown that wiping-out occurred during time interval (t_5, t_6) and (t_7, t_8).

Let s_{n-1} stand for the input which causes the last reversal of the Preisach boundary $\psi(\tau, r)$ and note that s_{n-1} will be used in the following section of the appendix to develop the derivative of a Preisach model.

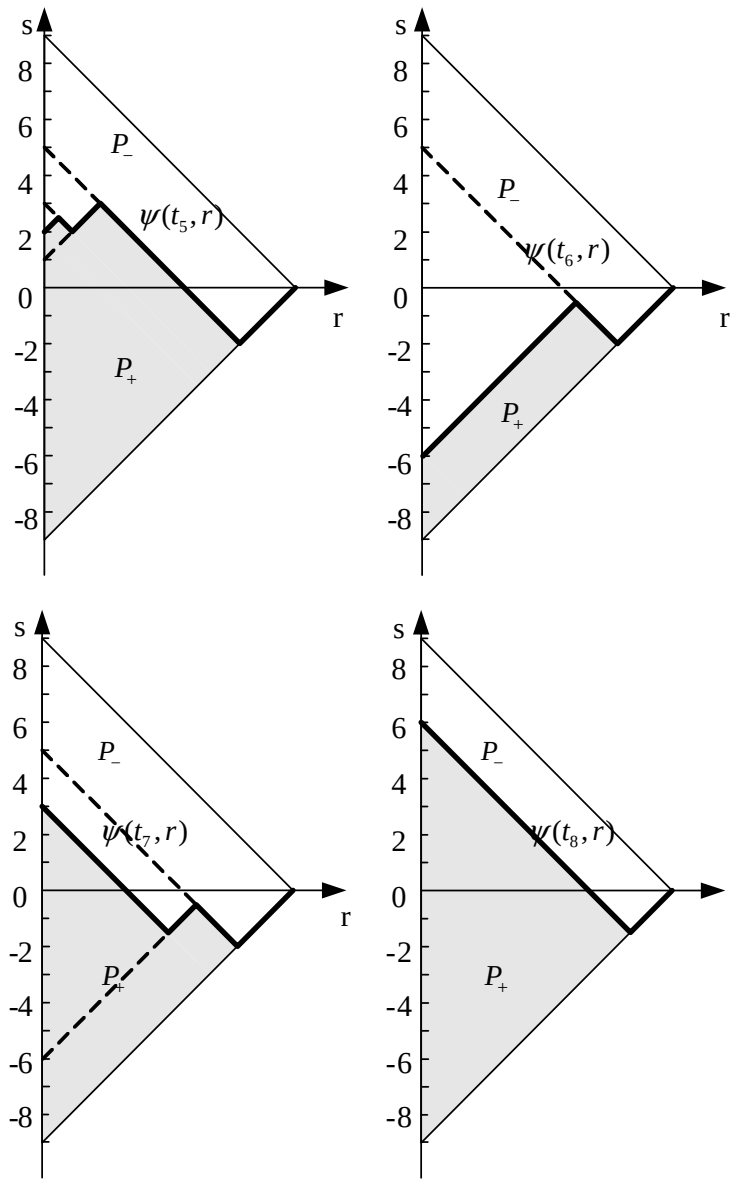

Figure A.2: Presaich plane and boundary of t_5 t_6 t_7 and t_8.

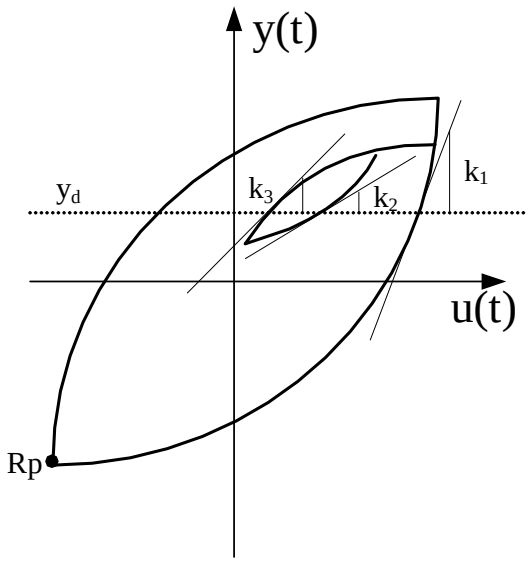

Figure A.3: Slopes of hysteresis loop on I/O plane.

A.2 Derivative of the Preisach Model

To improve eligibility of this section, we use the notation $\frac{dy}{du}$ to refer to the derivatives of the output with respect to the input $\frac{dy(t)}{du(t)}$ for the Preisach model, which are developed here since they are generally considered to be useful in optimization as they can illustrate the relationship between the input and the output variation. Together with the input derivative with respect to time $\frac{du(t)}{dt}$, the output derivative with respect to time $\frac{dy(t)}{dt}$ can also be calculated and it is essential for stability analysis. $\frac{dy}{du}$ is expected to be used in proving the better regulating performance of the neutral state with respect to input noise for piezoceramics.

Even though the Preisach model is not dependent on time, $\frac{dy}{du}$ for a hysteresis loop is different depending on whether $u(t)$ is increasing or decreasing and on the past history of the input for a given desired output y_d. Geometrically, $\frac{dy}{du}$ is the slope of the tangent line to the curve of the hysteresis in the I/O plane. As shown in Figure A.3, the slope k_1 of the ascending branch of the major loop is different from the slope k_2 of the ascending branch of the minor loop, and the slope k_3 on the descending branch of the minor loop is also different from the slope k_2. Moreover, the derivative is not defined when the input $u\,(t)$ reverses as shown by point R_p in Figure A.3, i.e. elements in the RMS change, so the subderivatives will be stated and computed.

The magnitude of the output variation is related to the area Ω swept by the Preisach boundary in response to a given input variation. s_{n-1} is the second-last element in the RMS as defined in the previous section. When dy/du is calculated in the following part of the section, a small change in u, namely Δu, is considered such that for the given boundary $\psi\,(\tau, r)$ no corners are wiped out. In Section A.2.1 and A.2.2, the cases of monotonic increase and decrease change in u are examined as shown in Figure A.4 (a) and (b) separately. In Section A.2.3, the cases of input

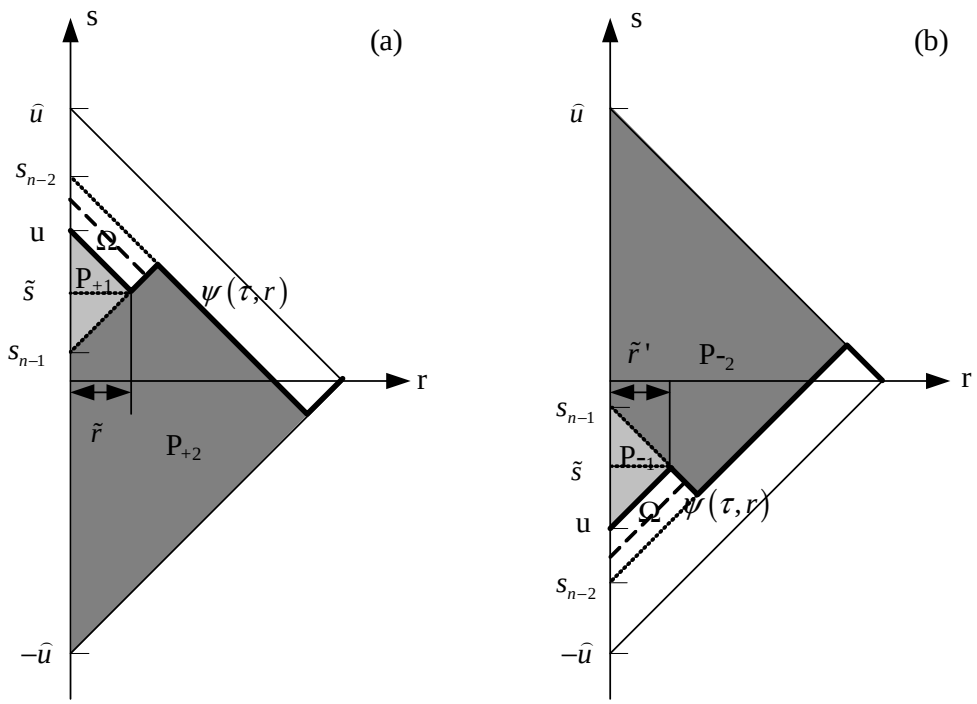

Figure A.4: Preisach plane for $\frac{dy}{du}$ calculation of monotonic input cases: (a) Case (a) monotonic increase input, (b) Case (b) monotonic decrease input.

reversals are investigated.

A.2.1 Derivative For Monotonically Increasing Input

First consider that input $u(t)$ does not change its direction and monotonically increases with respect to time, which is Case (a) shown in Figure A.4 (a), where $\tilde{r} = \frac{u - s_{n-1}}{2}$ and $\tilde{s} = \frac{u + s_{n-1}}{2}$. In this monotonic increase case, the derivative can be defined in a conventional way. Note that $\tilde{r}$ is positive. For a given boundary $\psi(\tau, r)$, assume that the input is increasing (Case (a)). According to Eq. (2.6) for a monotonic increase in input, the output y can be written as:

$$\begin{aligned} y &= 2 \iint\limits_{P_+(t)} \mu(r,s)\, dsdr - \iint\limits_{P_r} \mu(r,s)\, dsdr \\ &= 2 \left(\iint\limits_{P_{+1}(t)} \mu(r,s)\, dsdr + \iint\limits_{P_{+2}(t)} \mu(r,s)\, dsdr \right) - \iint\limits_{P_r} \mu(r,s)\, dsdr \end{aligned}$$

for Case (a), where $P_{+1}(t)$ and $P_{+2}(t)$ are as shown in Figure A.4 (a) by light and dark grey shaded regions. As indicated in the figure, only $P_{+1}(t)$ is changing with respect to $u(t)$ at this

time instantaneous as long as no wiping-out happens. Furthermore $u(t) > s_{n-1}$, such that $\tilde{r} > 0$. Thus

$$\frac{dy}{du} = 2\frac{d}{du}\left(\iint_{P_{+1}(t)} \mu(r,s)\, dsdr\right) \tag{A.1}$$

As in the section on Preisach modelling (Section 2.6), the form of the weighting function from [45] is considered here, i.e. $\mu(r,s) = v(r,s) + \kappa(s-r)\,\delta(2r)$.

Without loss of any generality, Eq.(A.1) can be rewritten as

$$\begin{aligned}\frac{dy}{du} &= 2\frac{d}{du}\left(\int_0^{\tilde{r}}\int_{s_{n-1}+r}^{u-r} v(r,s)\, dsdr\right) \\ &\quad +2\frac{d}{du}\left(\int_{s_{n-1}}^{\tilde{s}}\int_0^{s-s_{n-1}} \kappa(s-r)\,\delta(2r)\, drds + \int_{\tilde{s}}^{u}\int_0^{u-s} \kappa(s-r)\,\delta(2r)\, drds\right) \\ &= 2\frac{d}{du}\left(f_1(u) + f_2(u)\right)\end{aligned} \tag{A.2}$$

where

$$f_1(u) = \int_0^{\tilde{r}} g_1(r,u)\, dr \tag{A.3}$$

$$g_1(r,u) = \int_{s_{n-1}+r}^{u-r} v(r,s)\, ds \tag{A.4}$$

$$\begin{aligned}f_2(u) &= \int_{s_{n-1}}^{\tilde{s}}\int_0^{s-s_{n-1}} \kappa(s-r)\,\delta(2r)\, drds \\ &\quad + \int_{\tilde{s}}^{u}\int_0^{u-s} \kappa(s-r)\,\delta(2r)\, drds\end{aligned} \tag{A.5}$$

Then according to the Leibniz Integral Rule [60]

$$\frac{\partial}{\partial z}\int_{a(z)}^{b(z)} f(x,z)\, dx = \int_{a(z)}^{b(z)} \frac{\partial f}{\partial z} dx + f(b(z),z)\frac{\partial b}{\partial z} - f(a(z),z)\frac{\partial a}{\partial z}$$

the following equations are obtained:

$$\begin{aligned}\frac{\partial f_1(u)}{\partial u} &= \frac{\partial}{\partial u}\int_0^{\tilde{r}} g_1(r,u)\, dr \\ &= \int_0^{\tilde{r}} \frac{\partial g_1(r,u)}{\partial u} dr + g_1(\tilde{r},u)\frac{\partial(\tilde{r})}{\partial u} - g_1(0,u)\frac{\partial 0}{\partial u} \\ &= \int_0^{\tilde{r}} \frac{\partial g_1(r,u)}{\partial u} dr + \frac{1}{2} g_1(\tilde{r},u)\end{aligned} \tag{A.6}$$

where

$$\begin{aligned}\frac{\partial g_1(r,u)}{\partial u} &= \frac{\partial}{\partial u}\int_{s_{n-1}+r}^{u-r} v(r,s)\,ds \\ &= \int_{s_{n-1}+r}^{u-r}\frac{\partial v(r,s)}{\partial u}ds + v(r,u-r)\frac{\partial(u-r)}{\partial u} - v(r,s_{n-1}+r)\frac{\partial(s_{n-1}+r)}{\partial u} \\ &= v(r,u-r) \end{aligned} \tag{A.7}$$

Substituting Eq. (A.7) into Eq. (A.6) leads to

$$\begin{aligned}\frac{\partial f_1(u)}{\partial u} &= \int_0^{\tilde{r}} v(r,u-r)\,dr + \frac{1}{2}\int_{s_{n-1}+\tilde{r}}^{u-\tilde{r}} v\left(\frac{u-s_{n-1}}{2},s\right)ds \\ &= \int_0^{\tilde{r}} v(r,u-r)\,dr \end{aligned} \tag{A.8}$$

due to continuous and bounded $v(r,s)$ and

$$\begin{aligned} u-\tilde{r} &= u-\frac{u-s_{n-1}}{2} = \frac{u+s_{n-1}}{2} \\ s_{n-1}+\tilde{r} &= s_{n-1}+\frac{u-s_{n-1}}{2} = \frac{u+s_{n-1}}{2} \end{aligned}$$

i.e. the interval of the second integration term goes to zero.

According to the properties of the Dirac delta function, i.e. $\delta(ax) = \frac{1}{|a|}\,\delta(x)$ and the Sifting Property [61], (A.5) can be rewritten as

$$\begin{aligned} f_2(u) &= \frac{1}{2}\left(\int_{s_{n-1}}^{\tilde{s}}\kappa(s-0)\,ds + \int_{\tilde{s}}^{u}\kappa(s-0)\,ds\right) \\ &= \frac{1}{2}\int_{s_{n-1}}^{u}\kappa(s)\,ds \end{aligned} \tag{A.9}$$

Since $\kappa(s)$ is continuous along the s axis, the Leibniz Integral Rule can be applied to get $\frac{df_2(u)}{du}$, which results in

$$\begin{aligned}\frac{\partial f_2(u)}{\partial u} &= \frac{1}{2}\left(\int_{s_{n-1}}^{u}\frac{\partial\kappa(s)}{\partial u}ds + \frac{\partial u}{\partial u}\kappa(u) - \frac{\partial s_{n-1}}{\partial u}\kappa(s_{n-1})\right) \\ &= \frac{1}{2}\kappa(u) \end{aligned} \tag{A.10}$$

Substituting Eq.(A.8) and (A.10) into Eq.(A.2) to get

$$\frac{dy}{du} = 2\left(\int_0^{\tilde{r}} v(r,u-r)\,dr + \frac{1}{2}\kappa(u)\right) \tag{A.11}$$

Since $\tilde{r} > 0$ in Case (a)

$$\int_0^{\tilde{r}}\kappa(u-r-r)\,\delta(2r)\,dr = \frac{1}{2}\kappa(u) \tag{A.12}$$

Substituting Eq. (A.12) into Eq. (A.11) achieves

$$\begin{aligned}\frac{dy}{du} &= 2\left(\int_0^{\tilde{r}} v\left(r, u-r\right) + \kappa\left(u-r-r\right)\delta\left(2r\right)dr\right) \\ &= 2\int_0^{\tilde{r}} \mu\left(r, u-r\right)dr\end{aligned}$$

Let $\frac{dy}{du\uparrow^+}$ denotes $\frac{dy}{du}$ of Case (a), for monotonically increasing u thus

$$\frac{dy}{du\uparrow^+} = 2\int_0^{\tilde{r}} \mu\left(r, u-r\right)dr \tag{A.13}$$

$$= 2\int_0^{\tilde{r}} v\left(r, u-r\right)dr + \kappa\left(u\right) \tag{A.14}$$

If $\mu\left(r, u-r\right) \in M_p$, then the integration term in A.14 is always larger than or equal to zero. Thus $\frac{dy}{du\uparrow^+} \geq \kappa\left(u\right) \geq 0$. When $\tilde{r} = 0$, $\frac{dy}{du\uparrow^+} = \kappa\left(u\right) \geq 0$.

A.2.2 Derivative For Monotonically Decreasing Input

Similarly for monotonically decreasing input $du/dt < 0$, and $u\left(t\right)$ keeps decreasing (Case (b)) as shown in Figure A.4 (b) , i.e. $u\left(t\right) < s_{n-1}$. Thus $\tilde{r}' = \frac{s_{n-1}-u}{2} > 0$. According to Eq. (2.7):

$$\begin{aligned}y &= -2\iint\limits_{P_-(t)} \mu\left(r,s\right)dsdr + \iint\limits_{P_r} \mu\left(r,s\right)dsdr \\ &= -2\left(\iint\limits_{P_{-1}(t)} \mu\left(r,s\right)dsdr + \iint\limits_{P_{-2}(t)} \mu\left(r,s\right)dsdr\right) + \iint\limits_{P_r} \mu\left(r,s\right)dsdr\end{aligned}$$

for Case (b), where $P_{-1}\left(t\right)$ and $P_{-2}\left(t\right)$ are as shown in Figure A.4 (b) by light and dark grey shaded regions. As indicated in the figure, only $P_{-1}\left(t\right)$ is changing with respect to $u\left(t\right)$ at this time instaneous as long as no wiping-out happens. Thus

$$\frac{dy}{du} = -2\frac{d}{du}\left(\iint\limits_{P_{-1}(t)} \mu\left(r,s\right)dsdr\right) \tag{A.15}$$

Similarly to Case (a) without loss of any generality, Eq.(A.15) can be rewritten as

$$\begin{aligned}\frac{dy}{du} &= -2\frac{d}{du}\left(\int_0^{\tilde{r}'}\int_{u+r}^{s_{n-1}-r} v\left(r,s\right)dsdr\right) \\ &= -2\frac{d}{du}\left(\int_{\tilde{s}}^{s_{n-1}}\int_0^{s_{n-1}-s} \kappa\left(s-r\right)\delta\left(2r\right)drds + \int_u^{\tilde{s}}\int_0^{s-u} \kappa\left(s-r\right)\delta\left(2r\right)drds\right) \\ &= -2\frac{d}{du}\left(f_3\left(u\right) + f_4\left(u\right)\right)\end{aligned} \tag{A.16}$$

where

$$f_3(u) = \int_0^{\tilde{r}'} g_2(r,u)\,dr \tag{A.17}$$

$$g_2(r,u) = \int_{u+r}^{s_{n-1}-r} v(r,s)\,ds \tag{A.18}$$

$$\begin{aligned} f_4(u) &= \int_{\tilde{s}}^{s_{n-1}} \int_0^{s_{n-1}-s} \kappa(s-r)\,\delta(2r)\,dr ds \\ &\quad + \int_u^{\tilde{s}} \int_0^{s-u} \kappa(s-r)\,\delta(2r)\,dr ds \end{aligned} \tag{A.19}$$

Then according to the Leibniz Integral Rule [60],

$$\begin{aligned} \frac{\partial f_3(u)}{\partial u} &= \frac{\partial}{\partial u}\int_0^{\tilde{r}'} g_2(r,u)\,dr \\ &= \int_0^{\tilde{r}'} \frac{\partial g_2(r,u)}{\partial u} dr + g_2(\tilde{r}',u)\frac{\partial(\tilde{r}')}{\partial u} - g_2(0,u)\frac{\partial 0}{\partial u} \\ &= \int_0^{\tilde{r}'} \frac{\partial g_2(r,u)}{\partial u} dr - \frac{1}{2} g_2(\tilde{r}',u) \end{aligned} \tag{A.20}$$

where

$$\begin{aligned} \frac{\partial g_2(r,u)}{\partial u} &= \frac{\partial}{\partial u}\int_{u+r}^{s_{n-1}-r} v(r,s)\,ds \\ &= \int_{u+r}^{s_{n-1}-r} \frac{\partial v(r,s)}{\partial u} ds + v(r, s_{n-1}-r)\frac{\partial(s_{n-1}-r)}{\partial u} - v(r,u+r)\frac{\partial(u+r)}{\partial u} \\ &= -v(r,u+r) \end{aligned} \tag{A.21}$$

Substituting Eq. (A.21) into Eq. (A.20) leads to

$$\begin{aligned} \frac{\partial f_3(u)}{\partial u} &= \int_0^{\tilde{r}'} -v(r,u+r)\,dr - \frac{1}{2}\int_{u+\tilde{r}'}^{s_{n-1}-\tilde{r}'} v\left(\frac{s_{n-1}-u}{2}, s\right) ds \\ &= \int_0^{\tilde{r}'} -v(r,u+r)\,dr \end{aligned} \tag{A.22}$$

due to continuous and bounded $v(r,s)$ and

$$\begin{aligned} s_{n-1} - \tilde{r}' &= s_{n-1} - \frac{s_{n-1}-u}{2} = \frac{u+s_{n-1}}{2} \\ u + \tilde{r}' &= u + \frac{s_{n-1}-u}{2} = \frac{u+s_{n-1}}{2} \end{aligned}$$

i.e. the interval of the second integration term goes to zero.

According to the properties of the Dirac delta function, i.e. $\delta(ax) = \frac{1}{|a|}\,\delta(x)$ and the Sifting Property [61], Eq. (A.19) can be rewritten as

$$
\begin{aligned}
f_4(u) &= \frac{1}{2}\left(\int_{\tilde{s}}^{s_{n-1}} \kappa(s-0)\,ds + \int_{u}^{\tilde{s}} \kappa(s-0)\,ds\right) \\
&= \frac{1}{2}\int_{u}^{s_{n-1}} \kappa(s)\,ds
\end{aligned} \tag{A.23}
$$

Since $\kappa(s)$ is continuous along the s axis, the Leibniz Integral Rule can be applied to get $\frac{df_4(u)}{du}$, which results in

$$
\begin{aligned}
\frac{\partial f_4(u)}{\partial u} &= \frac{1}{2}\left(\int_{u}^{s_{n-1}} \frac{\partial \kappa(s)}{\partial u} ds + \frac{\partial s_{n-1}}{\partial u}\kappa(s_{n-1}) - \frac{\partial u}{\partial u}\kappa(u)\right) \\
&= -\frac{1}{2}\kappa(u)
\end{aligned} \tag{A.24}
$$

Substituting Eq.(A.22) and (A.24) into Eq.(A.16) to get

$$
\frac{dy}{du} = -2\left(\int_{0}^{\tilde{r}'} -v(r, u+r)\,dr - \frac{1}{2}\kappa(u)\right) \tag{A.25}
$$

Since $\tilde{r}' > 0$

$$
\int_{0}^{\tilde{r}'} \kappa(u+r-r)\,\delta(2r)\,dr = \frac{1}{2}\kappa(u) \tag{A.26}
$$

Substituting Eq. (A.26) into Eq. (A.25) achieves

$$
\begin{aligned}
\frac{dy}{du} &= 2\left(\int_{0}^{\tilde{r}'} v(r, u+r) + \kappa(u+r-r)\,\delta(2r)\,dr\right) \\
&= 2\int_{0}^{\tilde{r}'} \mu(r, u+r)\,dr
\end{aligned}
$$

Let $\frac{dy}{du\downarrow^-}$ denotes $\frac{dy}{du}$ of Case (b), for monotonically decreasing u thus

$$
\frac{dy}{du\downarrow^-} = 2\int_{0}^{\tilde{r}'} \mu(r, u+r)\,dr \tag{A.27}
$$

$$
= 2\int_{0}^{\tilde{r}'} v(r, u+r)\,dr + \kappa(u) \tag{A.28}
$$

If $\mu(r, u+r) \in M_p$, then the integration term in Eq. (A.28) is always larger than or equal to zero. Thus $\frac{dy}{du\downarrow^-} \geq \kappa(u) \geq 0$. When $\tilde{r}' = 0$, $\frac{dy}{du\downarrow^-} = \kappa(u) \geq 0$.

A.2.3 Subderivatives For Input Reversal Cases

At the input reversing point u_s, the classical derivative of the output with respect to the input in a hysteresis loop does not exist. Thus, the classical derivative should be extended to a generalized format at input reversals. The generalized derivative in [62] is adopted here.

Consider the absolute value as a simple example first:

$$h(u) = |u| \tag{A.29}$$

$h(u)$ does not have derivative at $u = 0$. However, both left and right derivatives of $h(u)$ at the origin are defined by

$$\begin{aligned} h'_{-}(u) &= \lim_{u' \uparrow u} \frac{h(u') - h(u)}{u' - u} \\ h'_{+}(u) &= \lim_{u' \downarrow u} \frac{h(u') - h(u)}{u' - u} \end{aligned}$$

where $u' \uparrow u$ means that u' approaches u from below, i.e. $u' < u$, and $u' \downarrow u$ represents u' tends to u from above, i.e. $u' > u$. For the function $h(u)$ in (A.29):

$$\begin{aligned} h'_{-}(0) &= -1 \\ h'_{+}(0) &= +1 \end{aligned}$$

As defined in [62], a generalized derivative $h'_{\lambda}(u)$ of h at u is a convex combination of its left and right derivatives $h'_{-}(u)$ and $h'_{+}(u)$, as shown below:

$$h'_{\lambda}(u) = (1 - \lambda) h'_{-}(u) + \lambda h'_{+}(u) \tag{A.30}$$

where $0 \leq \lambda \leq 1$. For the function $h(u)$ at the point of $u = 0$, the generalized derivative $h'_{\lambda}(0)$ are in the range of $\left[h'_{-}(0), h'_{+}(0)\right] = [-1, 1]$ and can be expressed as

$$h'_{\lambda}(u) = 2\lambda - 1$$

The definition of the generalized derivative above applies to single-valued functions, but the hysteresis graph around an input reversal is multi-valued with a cusp at the switching point $u = u_s$ as shown by the point R_p in Figure A.3. The definition can be easily extended, however, by looking at the derivatives on either side of the switching point u_s and taking limits as $u \to u_s$ on either function.

As developed in Section A.2.1 and A.2.2, output derivative with respect to input $\frac{dy}{du}$ can be written as

$$\begin{aligned} \frac{dy}{du} &= y'(u) \\ &= \begin{cases} y'_1(u) & \text{if } \frac{du}{dt} < 0 \\ y'_2(u) & \text{if } \frac{du}{dt} > 0 \end{cases} \end{aligned}$$

where $y'_1(u) = \frac{dy}{du\downarrow^-}$ as shown in Eq.(A.27) and $y'_2(u) = \frac{dy}{du\uparrow^+}$ as shown in Eq. (A.13). At input reversals u_s, the classical derivative $y'(u)$ is not defined. However it lies within the range of $y'_1(u)$ and $y'_2(u)$.

As a result, define the subderivative at u_s as:

$$y'(u_s) = \left[\lim_{u \to u_s} y'_1(u), \lim_{u \to u_s} y'_2(u)\right] \tag{A.31}$$

which can also be expressed in a convex combination of the range's lower and upper limits as

$$y'_\lambda(u_s) = (1-\lambda)\lim_{u\to u_s} y'_1(u) + \lambda \lim_{u\to u_s} y'_2(u)$$

Suppose that the input switched from decreasing to increasing at $u = u_s$, at time $t = t_r$. Figure A.5 (a) shows the Preisach plane just after the reversal and Figure A.5 (a') shows the Preisach plane just prior to the reversal. Over $\tau > \tau_r$, $u(\tau) \to s_{n-1}(u,\tau) = u_s = u(\tau_r)$ and the Preisach boundary is shown as $\psi(\tau, r)$. Moreover, the boundary of $\psi(\tau', r)$ is shown in Figure A.5 (a') and it can be observed that $s_{n-1}(u,\tau') = s_{n-2}(u,\tau)$. The dashed line in the figure shows the boundary of the time at switching point τ_r in Figure A.5 (a) and (a'). It is important to notice that for the reversal cases, a new corner appears on the Preisach boundary and the second last element in RMS needs to be updated, such as $s_{n-2}(u,\tau) = s_{n-1}(u,\tau')$ when calculating $\lim_{u\to u_s} y'_2(u)$ and $s_{n-1}(u,\tau) = u_s$ when calculating $\lim_{u\to u_s} y'_1(u)$. The range of subderivatives are calculated as below for input reversing from decreasing to increasing first.

For Case (a) and (a') in Figure A.5:

$$\begin{aligned}
\lim_{u\to u_s} y'_1(u) &= \lim_{u\to u_s} 2\int_0^{\frac{s_{n-2}-u}{2}} \mu(r, u+r)\, dr \\
&= \lim_{u\to u_s} 2\int_0^{\frac{s_{n-2}-u}{2}} v(r, u+r)\, dr + \kappa(u) \\
&= 2\int_0^{\frac{s_{n-2}-u_s}{2}} v(r, u_s+r)\, dr + \kappa(u_s) \qquad \text{(A.32)}
\end{aligned}$$

$$\lim_{u\to u_s} y'_2(u) = \lim_{u\to u_s} 2\int_0^{\frac{u-s_{n-1}}{2}} \mu(r, u-r)\, dr \qquad \text{(A.33)}$$

Noting $u_s = s_{n-1}(u,\tau)$, Eq. (A.33) becomes

$$\lim_{u\to u_s} y'_2(u) = \kappa(u_s)$$

Thus

$$\begin{aligned}
y'_\lambda(u_s) &= (1-\lambda)\lim_{u\to u_s} y'_1(u) + \lambda \lim_{u\to u_s} y'_2(u) \\
&= (1-\lambda)\left(2\int_0^{\frac{s_{n-2}-u_s}{2}} v(r, u_s+r)\, dr + \kappa(u_s)\right) + \lambda\kappa(u_s) \\
&= 2(1-\lambda)\int_0^{\frac{s_{n-2}-u_s}{2}} v(r, u_s+r)\, dr + \kappa(u_s) \qquad \text{(A.34)}
\end{aligned}$$

On the other hand, if the input starts to decrease from increasing also generates a reversal u_s in input when $t = \tau_r$. Similarly the Preisach boundaries just after the reversal and prior to the reversal are shown in Figure A.5 (b) and(b') respectively. The range of subderivatives for this

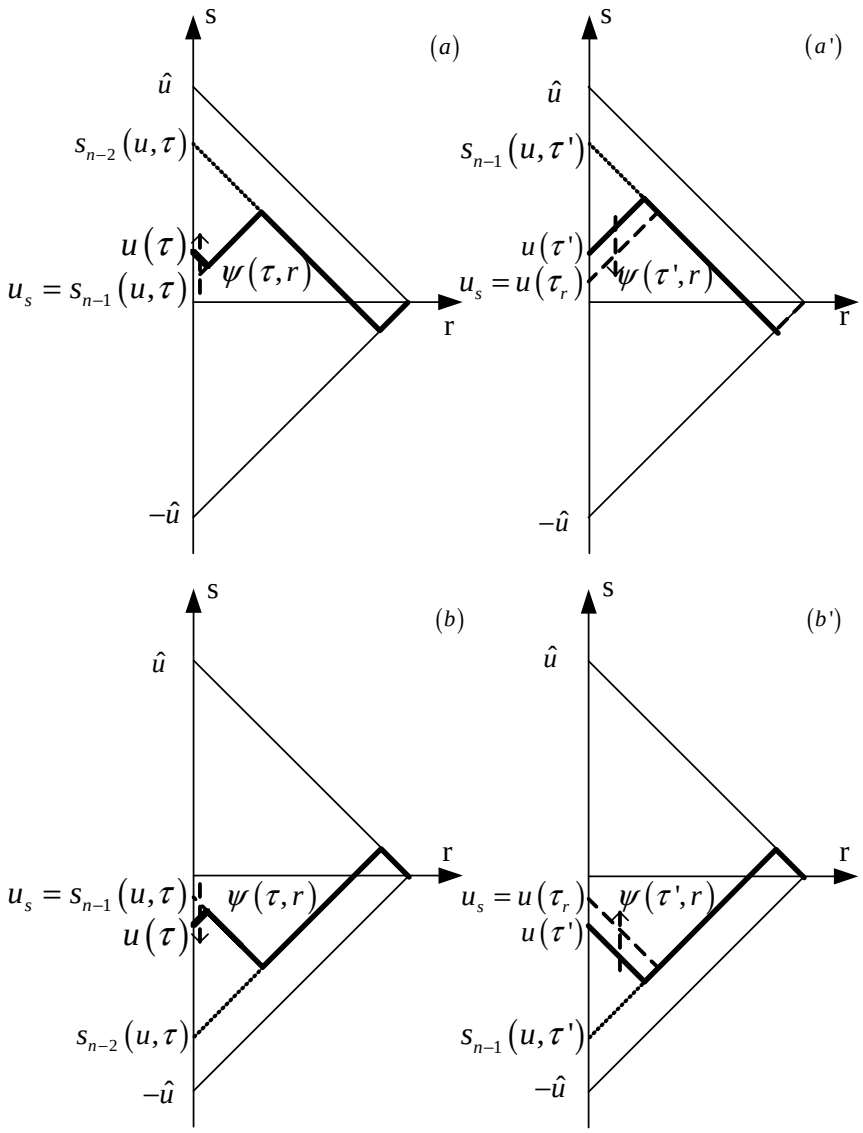

Figure A.5: Preisach plane for $\frac{dy}{du}$ calculation of reversal input cases: (a) After reversal from decreasing to increasing, (a') Prior to reversal from decreasing to increasing, (b) After reversal from increasing to decreasing, (b') Prior to reversal from decreasing to increasing.

kind of reversal are calculated as below.

$$\begin{aligned}\lim_{u\to u_s} y_2'(u) &= \lim_{u\to u_s} 2\int_0^{\frac{u-s_{n-2}}{2}} \mu(r, u-r)\,dr \\ &= \lim_{u\to u_s} 2\int_0^{\frac{u-s_{n-2}}{2}} v(r, u-r)\,dr + \kappa(u) \\ &= 2\int_0^{\frac{u_s-s_{n-2}}{2}} v(r, u_s-r)\,dr + \kappa(u_s) \end{aligned} \tag{A.35}$$

$$\lim_{u\to u_s} y_1'(u) = \lim_{u\to u_s} 2\int_0^{\frac{s_{n-1}-u}{2}} \mu(r, u+r)\,dr \tag{A.36}$$

Noting $u_s = s_{n-1}(u,\tau)$, Eq. (A.36) becomes

$$\lim_{u\to u_s} y_1'(u) = \kappa(u_s)$$

Thus

$$\begin{aligned} y_\lambda'(u_s) &= (1-\lambda)\lim_{u\to u_s} y_1'(u) + \lambda \lim_{u\to u_s} y_2'(u) \\ &= (1-\lambda)\kappa(u_s) + \lambda\left(2\int_0^{\frac{u_s-s_{n-2}}{2}} v(r, u_s-r)\,dr + \kappa(u_s)\right) \\ &= 2\lambda\int_0^{\frac{u_s-s_{n-2}}{2}} v(r, u_s-r)\,dr + \kappa(u_s) \end{aligned} \tag{A.37}$$

Moreover, since λ is only an arbitrary number in $[0,1]$, λ and $1-\lambda$ are in the same range. Thus, the subderivative at input reversals of a hysteresis loop can finally be written as:

$$y_\lambda'(u_s) = 2\lambda\int_0^{\frac{sgn(u_s-s_{n-2})(u_s-s_{n-2})'}{2}} v(r, u_s-(sgn(u_s-s_{n-2}))\,r)\,dr + \kappa(u_s) \tag{A.38}$$

where $\lambda\in[0,1]$. If $\mu(r, u_s-(sgn(u_s-s_{n-2}))\,r)\in M_p$, then $y_\lambda'(u_s) > \kappa(u_s)$. When the interval of the first integration term goes to zero, i.e. $u_s \to s_{n-2}$, $y_\lambda'(u_s)$ is minimized to be $\kappa(u_s)$.

It is easy to verify that the extending of the generalized derivative definition from [62] to multi-valued functions, as presented here, reduces for the definition of [62] for the case of $h(u) = |u|$.

In summary, the derivative of a hysteresis loop is defined as

$$\frac{dy}{du} = \begin{cases} y_1'(u) \text{ if } \frac{du}{dt} < 0 \\ y_2'(u) \text{ if } \frac{du}{dt} > 0 \\ y_\lambda'(u_s) \text{ at } u(t) \text{ reversals} \end{cases} \tag{A.39}$$

Appendix B

Experimental Calibration

The manner in which the ADCs of the Quanser Data Acquisition Card are calibrated is described in Section B.1, whereas the relationship between the analogue voltage from the DACs of the Quanser Data Acquisition Card and the high output voltage of the power amplifier (SA11) is investigated in Section B.2.

B.1 Quanser ADC

The output signal of the strain gauge amplifier is measured through the ADC. In order to calibrate the ADC on the Quanser-PCI Multi-Q DAQ, a -5 to +5 VDC voltage is supplied by a DC power supply through the ADC sockets. The input voltage from the DC power supply is measured with a multimeter (FLUKE 189 TRUE RMS MULTIMETER). Each ADC channel is sampled and controlled via the Matlab real-time workshop using the Weighted Moving Average block [1] to take the average of the 10 most recent samples (sampling time is 1 ms). Four channels, Ch0 to Ch3, are tested for proper functioning as listed in Table B.1.

[1] Simulink block of Matlab Version 7.5.0.342 (R2007b)

Table B.1: Analogue input voltage and digital output voltage ADC (Ch0 to Ch3)

Power Supply (V)	Ch 0 (V)	Ch 1 (V)	Ch 2 (V)	Ch 3 (V)
-5.00	-5.00	-5.00	-5.00	-5.00
-4.00	-4.02	-4.03	-4.03	-4.03
-3.00	-3.02	-3.02	-3.02	-3.02
-2.00	-2.02	-2.02	-2.02	-2.02
-1.00	-1.01	-1.01	-1.01	-1.01
0.00	0.00	0.00	0.00	0.00
1.00	1.00	1.00	1.00	1.00
2.00	2.00	2.00	2.00	2.00
3.00	3.00	3.00	3.01	3.01
4.00	4.01	4.02	4.02	4.00
5.00	5.00	5.00	5.00	5.00

B.2 Quanser DAC+SA11 Amplifier

Table B.2 depicts the data collected to reveal the relationship between the voltage signal sent out from the Quanser DAC socket and the output voltage of the SA11 amplifier. In the table, output channel A (Ch A) of SA11 (Va_{out}) is controlled by the analogue voltage on CH 0 (Va_{in}) of the Quanser DAC card, while output channel B (Ch B), i.e. Vb_{out}, is controlled by CH 1 (Vb_{in}). In Table B.2, $Va_{in} = Vb_{in}$ noted by Va, b_{in}. The output voltage of the SA11 amplifier is measured by the digital multimeter which can show five digits. Thus, two decimal digits are listed in Table B.2 since the range of the output voltage of the SA11 amplifier lies between ± 150 V.

Table B.2: Digital voltage set by Matlab and output voltage of the power amplifier

Va, b_{in} (V)	Va_{out} (V)	Vb_{out} (V)	Va, b_{in} (V)	Va_{out} (V)	Vb_{out} (V)
0	-0.45	-0.34	-10	141.30	141.06
1	-14.56	-14.42	-9	127.22	127.00
2	-28.66	-28.48	-8	113.12	112.94
3	-42.77	-42.57	-7	99.01	98.86
4	-56.88	-56.64	-6	84.91	84.79
5	-70.97	-70.70	-5	70.81	70.72
6	-85.08	-84.78	-4	56.71	56.65
7	-99.18	-98.84	-3	42.61	42.59
8	-113.29	-112.93	-2	28.50	28.50
9	-127.39	-126.99	-1	14.40	14.44
10	-141.48	-141.05	0	-0.45	-0.34

It is assumed that the relationship between the digital input voltage of the DAC channels and the analogue output voltage of the power amplifier SA11 is linear. Then the "Polyfit" function

of Matlab is used to establish the relationship by 1st order polynomial. The experimental data Va_{out} Vb_{out} and the linear fit line $\widetilde{Va}_{out}$ $\widetilde{Vb}_{out}$ are shown in the following Figures B.1 (a) and B.2 (a). Moreover, the errors between the experimental data, Va_{out} Vb_{out}, and the linear fit data, $\widetilde{Va}_{out}$ $\widetilde{Vb}_{out}$, are shown in Figures B.1 (b) and B.2 (b) respectively.

The RMS values of the errors between the linear fit data and the experimental data are 0.20 V and 0.19 V respectively. For Ch A and Ch B of the power amplifier, the following functions are used to describe the relationship between the input and output voltages of the SA11 amplifier approximately.

$$Va_{out} \approx \widetilde{Va}_{out} = -14.16 \times Va_{in} - 0.12 \tag{B.1a}$$

$$Vb_{out} \approx \widetilde{Vb}_{out} = -14.12 \times Vb_{in} - 0.02 \tag{B.1b}$$

The applied voltage on the other two Flexmorphs holds the same magnitude as Va_{out} and Vb_{out} respectively, but with the opposite polarity. In this thesis, only one Flexmorph will be examined. Its high input voltage is calculated based on Eq.(B.1b) although variables are renamed and shown below in Eq.(B.2) for an easier understanding.

$$V_{in} = -14.12 \times Vb_{in} - 0.02 \tag{B.2}$$

Its output is measured through Ch 1 of the Quanser ADC socket and named V_{out}.

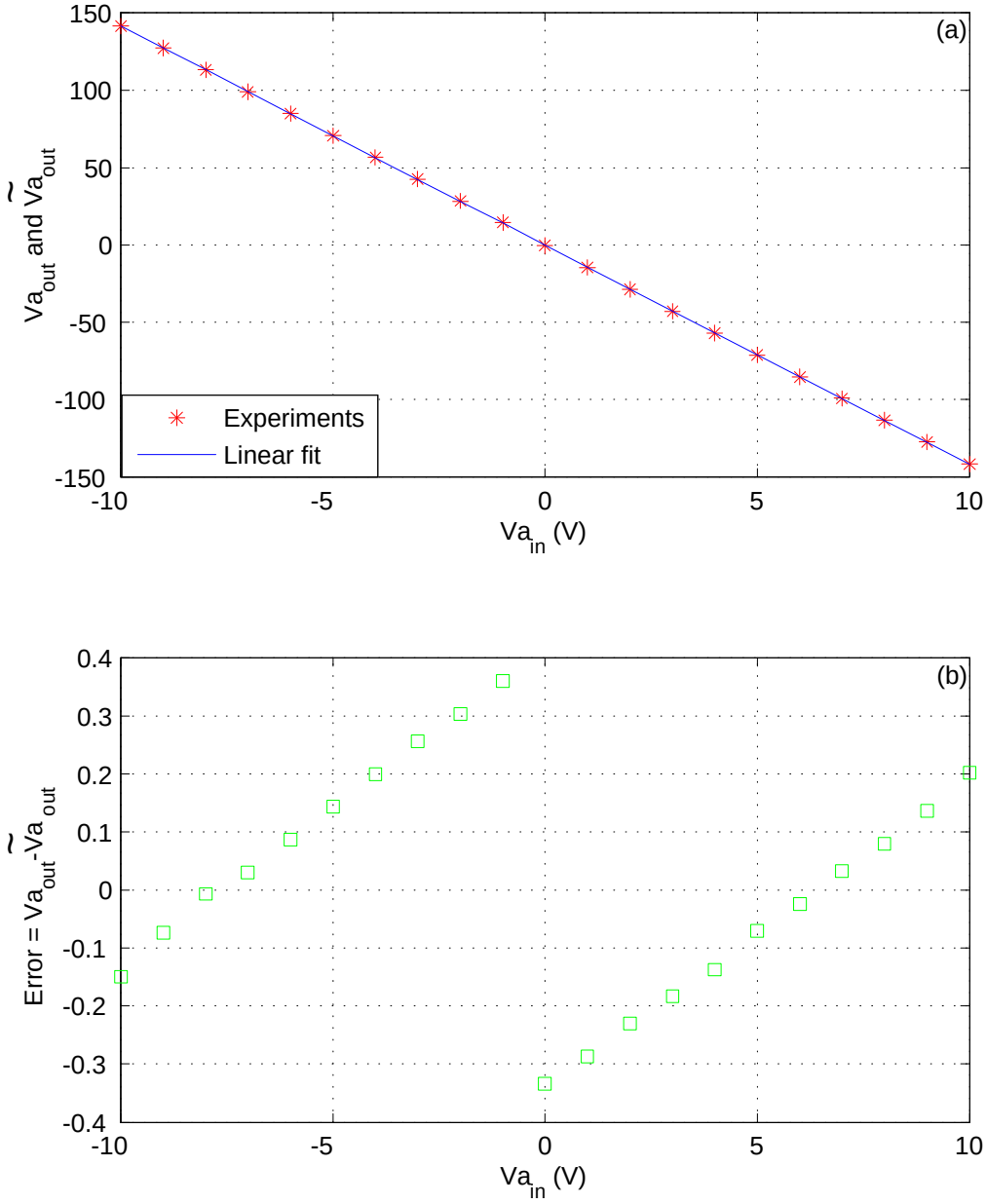

Figure B.1: Relationship between input and output of amplifier channel A. (a) Va_{out} and $\widetilde{Va}_{out}$; (b) error between Va_{out} and $\widetilde{Va}_{out}$.

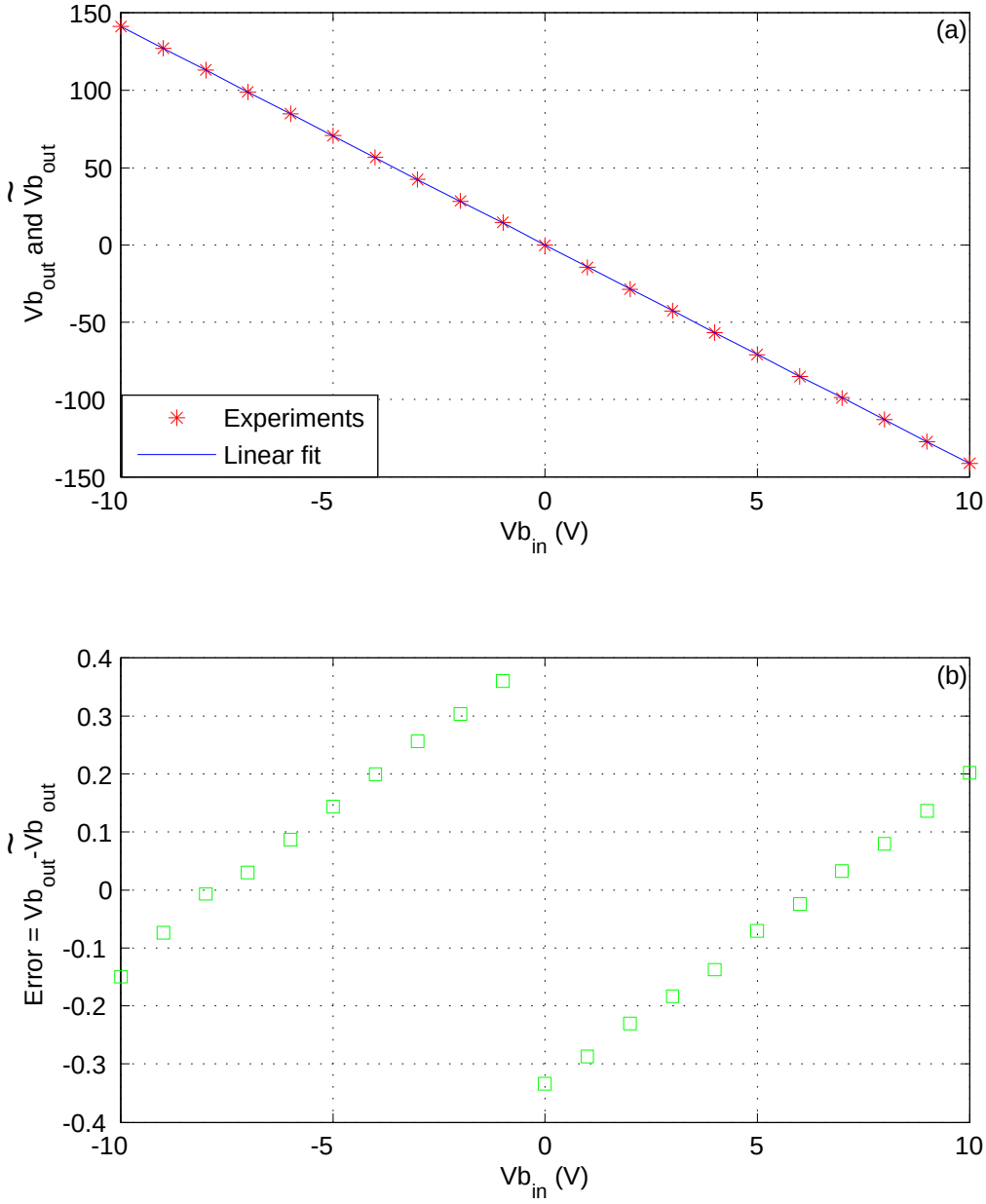

Figure B.2: Relationship between input and output of amplifier channel B. (a) Vb_{out} and $\widetilde{Vb}_{out}$; (b) error between Vb_{out} and $\widetilde{Vb}_{out}$.

References

[1] B. Culshaw. *Smart Structures and Materials*. Artech House, 1996.

[2] R.T. Haftka and H.M. Adelman. An analytical investigation of shape control of large space structures by applied temperatures. *AIAA*, 23(3):450–457, 1985.

[3] Physik Instrumente L.P. Designing with piezoelectric transducers: nanopositioning fundamentals. Piezo Actuator Tutorial, 2005.

[4] D.B. Koconis, L.P. Kollar, and G.S. Springer. Shape Control of Composite Plates and Shells with Embedded Actuators. II. Desired Shape Specified. *Journal of Composite Materials*, 28(3):262, 1994.

[5] B.N. Agrawal and K.E. Treanor. Shape control of a beam using piezoelectric actuators. *Smart Materials and Structures*, 8(6):729–739, 1999.

[6] F.M. Callier and C.A. Desoer. *Linear System Theory*. Springer, 1991.

[7] R.B. Gorbet. Influence of Initial State on Position Regulation of Hysteretic Actuators. *Journal of Intelligent Material Systems and Structures*, page 1045389X07087131v1, 2008 (Online version, accessed June 30 2008).

[8] G. Tao and P.V. Kokotovic. Adaptive control of plants with unknown hystereses. *Automatic Control, IEEE Transactions on*, 40(2):200–212, 1995.

[9] I.D. Mayergoyz. *Mathematical Models of Hysteresis*. Springer-Verlag, New York, 1991.

[10] A. Visintin. *Differential Models of Hysteresis*, volume 111 of *Applied Mathematical Sciences*. Springer-Verlag, New York, 1994.

[11] D.C. Jiles. Frequency dependence of hysteresis curves in conducting magnetic materials. *Journal of Applied Physics*, 76:5849, 1994.

[12] D.C. Jiles and D.L. Atherton. Theory of ferromagnetic hysteresis (invited). *Journal of Applied Physics*, 55:2115, 1984.

[13] D.W. Bondurant and F.P. Gnadinger. Ferroelectrics for nonvolatile RAMs. *Spectrum, IEEE*, 26(7):30–33, 1989.

[14] J. Millman and A. Grabel. *Microelectronics*. McGraw-Hill, New York, second edition, 1987.

[15] H.B. Callen. *Thermodynamics and an Introduction to Thermostatics*. Wiley, New York, 1985.

[16] S. Can, M.S. Richards, and R.A. Pease. A 3 V thermostat circuit. *Bipolar/BiCMOS Circuits and Technology Meeting, 1996., Proceedings of the 1996*, pages 105–108.

[17] K. Bhattacharya, R.D. James, and P.J. Swart. Relaxation in shape-memory alloysąłPart I. Mechanical model. *Acta Materialia*, 45(11):4547–4560, 1997.

[18] Y. Mualem. Theory of universal hysteretical properties of unsaturated porous media. *Proc. Fort Collins Fluid Intern. Hydrol. Symp. 1977*.

[19] J. Cacko. Simulation experiments in investigation of fatigue degradation effects of dynamic processes. *Eur. Simulation Multiconf. 1995*, pages 92–96, 1995.

[20] C. Truesdell and W. Noll. *The Non-Linear Field Theories of Mechanics*. Springer, 2004.

[21] R.C. Smith. *Smart material systems: model development*. Society for Industrial Mathematics, 2005.

[22] C. Niezrecki, D. Brei, S. Balakrishnan, and A. Moskalik. Piezoelectric Actuation: State of the Art. *The Shock and Vibration Digest*, 33(4):269, 2001.

[23] Sensor Technology Limited. *SS15 Shape Control Unit*. Sensor Technology Limited, Collingwood, 2005.

[24] C.B. Sawyer. The use of Rochelle salt crystals for electrical reproducers and microphones. *Proc. Inst. Radio Eng*, 19(11):2020–2029, 1931.

[25] M.R. Steel, F. Harrison, and P.G. Harper. Piezoelectric bimorph–an experimental and theoretical study of its quasi-static response. *J. Phys. D*, 11(6):979–89, 1978.

[26] H.S. Tzou. Development of a light-weight robot end-effector using polymericpiezoelectric bimorph. *Robotics and Automation, 1989. Proceedings., 1989 IEEE International Conference on*, pages 1704–1709, 1989.

[27] S. Chonan, Z.W. Jiang, and M. Koseki. Soft-handling gripper driven by piezoceramic bimorph strips. *Smart Materials & Structures*, 5(4):407–414, 1996.

[28] J.A. August and S.P. Joshi. Preliminary design of smart structure fins for high-speed missiles. *Proceedings of SPIE*, 2721:58, 1996.

[29] T. Kaneko, T. Ohmi, N. Ohya, and N. Kawahara. A compact and quick-response dynamic focusing lens. *Sensors & Actuators: A. Physical*, 70(1-2):92–97, 1998.

[30] Ferroelectrics Standards Committee of the IEEE Ultrasonics and Frequency Control Society. An american national standard: Ieee standard on piezoelectricity. *The institute of Electrical and Electronics Engineers, ANSI/ IEEE Std*, 176, 1987.

[31] M. Goldfarb and N. Celanovic. Modeling piezoelectric stack actuators for control ofmicromanipulation. *Control Systems Magazine, IEEE*, 17(3):69–79, 1997.

[32] R.C. Smith, A.G. Hatch, B. Mukherjee, and S. Liu. A Homogenized Energy Model for Hysteresis in Ferroelectric Materials: General Density Formulation. *Journal of Intelligent Material Systems and Structures*, 16(9):713, 2005.

[33] I.J. Busch-Vishniac. *Electromechanical Sensors and Actuators*. Springer, 1999.

[34] R.C. Smith and Z. Ounaies. A Domain Wall Model for Hysteresis in Piezoelectric Materials. *Journal of Intelligent Material Systems and Structures*, 11(1):62, 2000.

[35] M. Omura, H. Adachi, and Y. Ishibashi. Simulations of ferroelectric characteristics using a one-dimensional lattice model. *Jpn J Appl Phys*, 30:2384–2387, 1991.

[36] R.C. Smith, S. Seelecke, Z. Ounaies, and J. Smith. A Free Energy Model for Hysteresis in Ferroelectric Materials. *Journal of Intelligent Material Systems and Structures*, 14(11):719, 2003.

[37] F. Preisach. Ueber die magnetische Nachwirkung. *Zeitschrift fuer Physik*, 94(5-6):277–302, 1935.

[38] P. Ge and M. Jouaneh. Modeling hysteresis in piezoceramic actuators. *Precision Engineering*, 17(3):211–221, 1995.

[39] P. Ge and M. Jouaneh. Tracking control of a piezoceramic actuator. *Control Systems Technology, IEEE Transactions on*, 4(3):209–216, 1996.

[40] G. Robert, D. Damjanovic, N. Setter, and A.V. Turik. Preisach modeling of piezoelectric nonlinearity in ferroelectric ceramics. *Journal of Applied Physics*, 89:5067, 2001.

[41] W.S. Galinaitis and R.C. Rogers. Compensation for hysteresis using bivariate Preisach models. *Proceedings of SPIE*, 3039:538, 1997.

[42] H.T. Banks, A.J. Kurdila, and G. Webb. Identification of hysteretic control influence operators representing smart actuators, Part I: Formulation. *Mathematical Problems in Engineering*, 3(4):287–328, 1997.

[43] I.D. Mayergoyz and G. Friedman. Generalized Preisach model of hysteresis. *Magnetics, IEEE Transactions on*, 24(1):212–217, 1988.

[44] H. Hu, H. Zhang, and R.B. Mrad. Preisach based dynamic hysteresis model. *Intelligent Mechatronics and Automation, 2004. Proceedings. 2004 International Conference on*, pages 825–830, 2004.

[45] D. Hughes and J.T. Wen. Preisach modeling of piezoceramic and shape memory alloy hysteresis. *Smart Materials and Structures*, 6(3):287–300, 1997.

[46] J. Ortín. Preisach modeling of hysteresis for a pseudoelastic Cu-Zn-Al single crystal. *Journal of Applied Physics*, 71(4):1454, 1992.

[47] R.B. Gorbet. *Control of hysteretic systems with Preisach representations.* PhD thesis, University of Waterloo, 1998.

[48] R.B. Gorbet, K.A. Morris, and D. Wang. Control of hysteretic systems: a state-space approach. *Learning, Control and Hybrid Systems*, 241:432–451, 1998.

[49] Omega Engineering. *Omega Strain Gages Specifications Chart.* Omega Engineering, Laval.

[50] J. Edward Pope. *Rules of Thumb for Mechanical Engineers.* Gulf Professional Publishing, 1996.

[51] T. Sachdeva. Computer interfacing SS15. Technical report, University of Waterloo, 2006.

[52] R.B. Gorbet and R. Russell. A novel differential shape memory alloy actuator for position control. *Robotica*, 13(4):423–30, 1995.

[53] R.B. Gorbet, D. Wang, and K.A. Morris. Preisach model identification of a two-wire SMA actuator. *Robotics and Automation, 1998. Proceedings. 1998 IEEE International Conference on*, 3, 1998.

[54] J.A. Nedler and R. Mead. A simplex method for function minimization. *Computer Journal*, 7:308–313, 1965.

[55] R.B. Mrad and H. Hu. A Model for Voltage-to-Displacement Dynamics in Piezoceramic Actuators Subject to Dynamic-Voltage Excitations. *IEEE/ASME TRANSACTIONS ON MECHATRONICS*, 7(4):479, 2002.

[56] C.L. Phillips and H.T. Nagle. Digital control system analysis and design. 2007.

[57] B.M. Chen, T.H. Lee, C.C. Hang, Y. Guo, and S. Weerasooriya. An H_∞ almost disturbance decoupling robustcontroller design for a piezoelectric bimorph actuator with hysteresis. In *Advanced Motion Control, 1996. AMC'96-MIE. Proceedings., 1996 4th International Workshop on*, volume 2, 1996.

[58] Y. Stepanenko and C.Y. Su. Intelligent control of piezoelectric actuators. In *Decision and Control, 1998. Proceedings of the 37th IEEE Conference on*, volume 4, 1998.

[59] C.L. Hwang and C. Jan. A reinforcement discrete neuro-adaptive control for unknown piezoelectric actuator systems with dominant hysteresis. *IEEE Transactions on Neural networks*, 14(1):66–78, 2003.

[60] Frederick S Woods. *Advanced Calculus: A Course Arranged with Special Reference to the Needs of Students of Applied Mathematics*, chapter 60. Ginn, 1926.

[61] R.P. Kanwal. *Generalized Functions: Theory and Technique*. Birkhäuser, 1998.

[62] P. Wriggers and P.D. Panagiotopoulos. *New Developments in Contact Problems*. Springer, 1999.